



Norwegian University of Life Sciences  
Faculty of Science and Technology

Philosophiae Doctor (PhD)  
Thesis 2019:33

# Introducing microclimate into simulation models for buildings

Inkludering av mikroklima i  
simuleringsmodeller for bygninger

Stergiani Charisi



# Introducing microclimate into simulation models for buildings

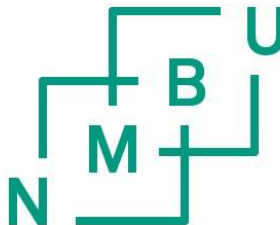
Inkludering av mikroklima i simuleringsmodeller for bygninger

Philosophiae Doctor (PhD) Thesis

Stergiani Charisi

Norwegian University of Life Sciences  
Faculty of Science and Technology

Ås 2019



Thesis: 2019:33

ISSN: 1894-6402

ISBN: 978-82-575-1592-8



To Aleksander

To my mother, Mairi

To my father, Vasilis

A doctoral thesis at a university in Norway is produced either as a monograph or as a collection of papers. In the latter case, the introduction part constitutes the formal thesis, which summarizes the accompanying papers already published or manuscripts at various stages (in press, submitted or in preparation).

Supervisors

**Thomas Kringlebotn Thiis, Dr. (main supervisor)**

Professor. Faculty of Science and Technology  
Norwegian University of Life Sciences (NMBU)  
P.O. box: 5003, REALTEK, 1432, Ås, Norway

**Ingunn Burud, Dr. (co-supervisor)**

Associate Professor. Faculty of Science and Technology  
Norwegian University of Life Sciences (NMBU)  
P.O. box: 5003, REALTEK, NO-1432, Ås, Norway

Evaluation Committee:

**Carsten Rode, Dr.**

Professor. Department of Civil Engineering.  
Technical University of Denmark (DTU)  
Brovej, Building 118, room 156, 2800 Kgs. Lyngby

**Arild Gustavsen, Dr.**

Professor. Department of Architectural Design, History and Technology  
Norwegian University of Science and Technology (NTNU)  
Alfred Getz vei 3, NO-7491, Trondheim, Norway

**Roberto Tomasi, Dr.**

Professor. Faculty of Science and Technology  
Norwegian University of Life Sciences (NMBU)  
P.O. box: 5003, REALTEK, 1432, Ås, Norway

... Men å drømme om noe usannsynlig har et eget navn. Vi kaller det *håp*.

... Αλλα το όνειρο του απίθανου έχει τη δική του ονομασία. Το αποκαλούμε  
*ελπίδα*.

Jostein Gaarder

## Acknowledgements

After three years on my PhD project, and without having finished writing my PhD thesis, I decided to write my acknowledgements. The people mentioned below have been with me during this three-year period and, regardless the outcome, the least I owe them is my regards, my gratitude, a big thank you.

First, I want to thank my supervisor, Thomas Thiis, for entrusting me with this PhD project and guiding me through the way. I will always be grateful for having been given this opportunity and for the good moments of this three-year period. I would also like to thank Professor Tormod Aurlien for his invaluable scientific advice, but also for all the nice and constructive conversations around science, religion and culture. I want also to thank my master thesis supervisor, Katerina Tsikaloudaki, for putting the seed of research to me and showing me the nice and warm face of academia.

I want to thank some of the REALTEK staff for the great collaboration and help throughout the years. Specifically, I would like to thank Mona K., Mona S. and Tone for helping me out so many times with administrative and financial matters. I would like to thank Berit for always being available and for all the guidance, she generously provided throughout my PhD. Also, I would like to thank Signe Kroken for always providing me with weather data on time, and Tom Ringstad for his invaluable help with my measuring equipment and for setting up a whole data acquisition system, which big part of my project was based on.

I want to thank my office mates, Dag, Iver and Ildiko, for all the nice moments, the lunch breaks, the conversations and the support. I want also to thank Solrun, who although was in a different building, was always there for me to spread her positivity during our lunch or coffee break.

Boris, I am extremely grateful for the fact that we were both on the same faculty for these past three years. Thank you for always giving me your lights, for making me smarter, and for generally being such a great friend. I will definitely miss our kaffedakia. I want also to thank Josipa, who has always been sending me her positive energy.

Δάσκαλε, thank you for every piece of advice, wisdom and guidance you have shared with me all these years. Most importantly, thank you for being such a great friend, always supportive, caring and fun, and for all the nice moments we share since the very first day I arrived in Norway.



Eva, I am really grateful to have such a great friend as you so close to me, always supportive, positive and eager to join me in any crazy endeavour.

Daskalaki, you showed up during my last and most stressful period of my PhD research, and your innocent and bright smile has been the best stress-relief during my thesis writing.

I want to also thank my dear filarakia, Nena, Vladanoula and D. Tzimirotas. It has been a privilege and a joy to have such a cool group of people surrounding me since my very first day in this country. Thank you opening up your warm circle for me and thank you for all the nice moments and dinnerakia we share.

Aggeliki and Ioanna, thank you both for always been there for me even though you are miles away. It has always been a pure joy and a great psychological relief to be able to call you, catch up with you and make the distance disappear.

I want to thank my grandparents and my aunts for their continuous concern and contact, and for always sending me their love and support.

I want to also thank my dear sisters, Vasiliki, Maria and Alexandra. Thank you for all the positivity, support and everyday contact that made me travel daily from LA or NY to Pyli, from Pyli to Thessaloniki, and never miss a thing! Maria, an extra 'thank you' to you for always giving me your lights as the greatest researcher I know, and thus making me sound smarter and cooler.

I want to thank my parents, Mairi and Vasili. Μαμά και Μπαμπά, thank you for being the most caring, loving, supportive and understanding parents anyone could wish for. You helped me chase my dreams. Nothing would have ever been possible without you. Even though we are miles apart, you are always in my heart.

Last but not least, I want to thank Aleksander. Viking μου, words are not good enough to describe how lucky, happy and grateful I am to have such a great, kind, positive, smart, fun and beautiful person as you by my side. Thank you for opening up to me a whole new world of culture, adventures and experiences, and for always jumping so eagerly into mine. You make my life perfect and complete in every possible way, and your endless support, help and encouragement during my PhD years have been priceless. Thank you for making these last three years the best years of my life, despite the stressful periods and some rough workdays. Thank you for all the advice, the solutions, the pep talks. Thank you for always giving me the inspiration to continue and the strength to never give up. Thank you for always being here for me! I would have never made it without you!

## Synopsis

The contemporary sustainability imperativeness requires high performance buildings. Smart solutions during the design or retrofiting phase can significantly contribute towards decreasing the energy consumption and gas emissions, as well as increasing the durability and life cycle of building materials. An invaluable tool that can facilitate both the design and retrofiting process is the building performance simulation. The optimization of building simulation models can lead towards better decision-making, and subsequently towards sustainability.

Climatic loads are one of the key variables in the building performance simulation. However, the climatic loads acting on buildings are determined by the micro scale climate. Buildings with the exact same geometry and construction can be subjected to different climatic loads depending on the local district morphology they belong to, even within the borders of the same city. Increasing the accuracy of climatic loads by taking into consideration the microclimate, will automatically increase the prediction accuracy of the building performance simulation.

This PhD research project aims on improving aspects of the building performance simulation by accounting for the microclimate. The climate-driven loads of wind, wind-driven rain and solar radiation acting on buildings are defined with respect to the microclimate, and some methods to introduce them in simulation models for buildings are investigated.

A simple hygrothermal model that can predict how the surface temperature and moisture content vary spatially along building façades is developed. The model is developed upon the basic principles of heat and moisture transport within the context of building physics. The developed model takes into consideration the microclimatic loads of wind-driven rain and solar radiation, which are determined by the surroundings and the building's geometry. In addition, the building's spatial architectural details are considered, thus revealing areas of high-exposure or shelter from rain and solar radiation. As a result, the climate-driven loads acting on the building façade investigated are more accurately defined. In contrast to most of the contemporary simulation models that treat façades uniformly, the developed model is able to predict the spatial variations of surface temperature and moisture content along the

building façades. On-site surface temperature and moisture measurements in two different façades verify the spatial accuracy of the model presented.

Furthermore, the micro-scale wind effects on buildings are researched. The wind-induced pressurization of the building envelope is one of the driving mechanisms of air infiltration, and air infiltration is crucial to the building energy consumption. As a result, predicting with high accuracy the wind-induced pressures acting on buildings can significantly improve the calculation of air infiltration and consequently of building energy demands.

Full-scale measurements on two reference buildings reveal high spatial pressure variations along the building façades. The measurements reveal that the wind-induced pressure variations are essentially determined by the building's surroundings and geometry. A common method to express the wind-induced pressure acting on a body is by means of wind pressure coefficients ( $C_p$ ). Therefore, the use of building-specific wind pressure coefficients as appropriate boundary conditions that can introduce the microclimate into building energy simulation is researched.

Building-specific wind pressure coefficients are calculated through full-scale measurements and computational fluid dynamics (CFD) simulations. The results show that building-specific wind pressure coefficients are able to capture the microclimatic effect. The use of building-specific  $C_p$  values on building energy simulations for the calculation of air infiltration is validated against tracer gas measurements for a reference building. In contrast to the conventional methods used for the air infiltration calculation, building-specific wind pressure coefficients manage to account for the microclimate. The results indicate that the prediction accuracy of calculated air infiltration rates using building-specific  $C_p$  values is significantly higher than the rest of the methods.

Furthermore, the use of fluctuating building-specific  $C_p$  values is evaluated. The Monte Carlo method is employed, and the probability distribution function (pdf) of building-specific  $C_p$  values is combined with the wind speed pdf. Cross validation with on-site measurements suggests that the statistical method can improve even further the accuracy of the air infiltration calculation.

## Sammendrag

Bærekraftig utvikling krever høyttelsesbygninger. Smarte løsninger i prosjektering av nye bygg og rehabilitering av eldre bygg kan bidra til å redusere energiforbruk og klimagassutslipp, samt å øke holdbarhet og levetid for bygningsmaterialer. Bygningssimulering (Building Performance Simulation, BPS) er et viktig verktøy for å tilrettelegge for både god prosjektering av nye bygg og rehabilitering av eldre bygg. Optimalisering av simuleringmodeller for bygninger kan effektivisere beslutningsprosessen og bidra til bærekraftig utvikling.

Klimabelastninger er viktige variabler i BPS. Opptredende klimabelastning på en bygning påvirkes av omkringliggende mikroklima. Bygninger med lik oppbygning og identisk geometrisk utforming kan være utsatt for ulike klimabelastninger innenfor samme bygrense, på grunn av ulik omkringliggende topologi. Ved å ta hensyn til mikroklima kan man oppnå mer nøyaktige data på klimabelastninger, som resulterer i mer nøyaktige bygningssimuleringer.

Dette PhD forskningsprosjektet sikter på å forbedre aspekter ved bygningssimuleringer ved å ta hensyn til mikroklima. Klimabelastningene fra vind, slagregn og solstråling som opptrer på bygninger defineres med hensyn til mikroklima, og det er undersøkt hvordan man kan inkludere dem i bygningssimuleringsmodeller.

Det er utviklet en enkel hygrotermisk modell som kan forutse hvordan overflatetemperatur og fuktinnhold varierer over bygningsfasaden. Modellen er utviklet fra grunnleggende prinsipper om fukt- og varmetransport. Modellen tar hensyn til mikroklimabelastninger fra slagregn og solstråling som er bestemt av omgivelsene og bygningens geometri. I tillegg er tatt hensyn til arkitektoniske detaljer som viser arealer som er eksponert eller skjermet for regn og solstråling. Resultatet er mer nøyaktig bestemmelse av klimapåkjenninger på bygningens fasade. Modellen kan beregne varierende utbredelse av overflatetemperatur og fuktinnhold over fasaden, i motsetning til de fleste simuleringmodeller som simulerer hele fasaden som én enhet. Utførte feltforsøk av fra to forskjellige fasader viser at modellen beregner nøyaktig utbredelse av overflatetemperatur og fuktinnhold.

Videre er det forsket på effekten av lokale vindforhold på bygninger. Vind er en av hoveddrivkreftene for luftinfiltrasjon, og luftinfiltrasjon er avgjørende for

bygningens totale energiforbruk. Ved å beregne nøyaktig vindtrykk på fasaden kan man få mer nøyaktige beregningsresultater for luftinfiltrasjon og energibehov.

Målinger fra feltforsøk fra to referansebygninger viser stor variasjon av vindtrykk over fasaden. Målingene viser at variasjonen av vindtrykket bestemmes av bygningens geometri og omgivelser. En vanlig metode for å uttrykke vindtrykket på et legeme er ved vindtrykkkoeffisienten  $C_p$ . Bygningsspesifikk  $C_p$  kan brukes som grensebetingelse for å ta hensyn til mikroklima i energiberegninger.

Bygningsspesifikke vindtrykkkoeffisienter beregnes ved bruk av målinger fra feltforsøk og numerisk fluiddynamikk (computational fluid dynamics, CFD) beregninger. Resultatene viser at bygningsspesifikke vindtrykkkoeffisienter kan ta hensyn til effektene av mikroklima. Bruk av bygningsspesifikke vindtrykkkoeffisienter i energiberegninger for bygninger er validert mot sporgassmålinger for et referansebygg. I motsetning til konvensjonelle metoder for luftinfiltrasjonsberegninger, kan bygningsspesifikke vindtrykkkoeffisienter ta høyde for effektene fra mikroklima. Resultatene viser at ved å bruke bygningsspesifikke vindtrykkkoeffisienter øker nøyaktigheten til beregninger for luftinfiltrasjon sammenliknet med konvensjonelle metoder.

Videre er bruk av svingende bygningsspesifikke vindtrykkkoeffisienter vurdert. Monte Carlo metoden er benyttet, og sannsynlighetsfordeling av bygningsspesifikke vindtrykkkoeffisienter er kombinert med sannsynlighetsfordelt vindhastighet. Kryssvalidering med målinger fra feltforsøk viser at den statistiske metoden videre kan øke nøyaktigheten av luftinfiltrasjonsberegninger.

## List of Papers

### **Paper I**

Charisi, S.; Thiis, T.K.; Stefansson, P.; Burud, I.

Prediction model of microclimatic surface conditions on building façades, *Building and Environment* **2018**, 128, 46-54 (type: Journal article)

### **Paper II**

Charisi, S.; Waszczuk, M.; Thiis, T.K.

Investigation of the pressure coefficient impact on the air infiltration in buildings with respect to microclimate, *Energy Procedia* **2017**, 122, 637-642 (type: Journal article)

### **Paper III**

Charisi, S.; Thiis, T.K.; Aurlien, T.

Effect of microclimate on wind-induced pressurization of the building envelope: a test case of twin high-rise buildings. *Proceedings of 7<sup>th</sup> International Building Physics Conference (IBPC2018)*, 23-26 September 2018, Syracuse, NY, USA. (type: Article in proceedings – peer reviewed)

### **Paper IV**

Charisi, S.; Waszczuk, M.; Thiis, T.K.

Determining building-specific wind pressure coefficients to account for the microclimate in the calculation of air infiltration in buildings. *Advances in Building Energy Research* **2019**, DOI: 10.1080/17512549.2019.1596835 (type: Journal article)

### **Paper V**

Charisi, S.; Thiis, T.K.; Aurlien, T.

Full-scale measurements of wind-pressure coefficients in twin high-rise buildings. *Buildings* **2019**, 9, 63 (type: Journal article)

In **Paper I**, a model predicting the surface hygrothermal conditions of building façades with respect to the microclimate is presented. The surface temperature and moisture content are determined spatially along building façades by taking into account the building's surroundings, geometry and unique architectural characteristics.

In **Paper II**, the use of wind pressure coefficients ( $C_p$ ) in BES for the determination of air infiltration rates is investigated. Two different microclimatic cases are tested in order to determine the method's suitability for accounting for the microclimate. The accuracy of using  $C_p$  in the BES for calculating air changes is validated against tracer gas measurements.

In **Paper III**, the effect of microclimate on the wind-induced pressures developed on building façades is explored. Full-scale measurements on a twin medium-rise building complex are performed in order to research the microclimatic effect. The study discusses how the wind-induced pressures vary spatially along large façades and how they are affected by the surroundings.

In **Paper IV**, the wind pressure coefficient ( $C_p$ ) as appropriate microclimatic boundary condition on the building energy simulation is investigated. Two different microclimatic cases are explored and the air infiltration rates are calculated using building-specific wind pressure coefficients determined through CFD simulations. Tracer gas measurements on a reference building are used to define the method's accuracy. The method is compared with two other conventional methods used to define air infiltration rates, and the accuracy of each method is researched.

In **Paper V**, full-scale measurements for the determination of wind pressure coefficients ( $C_p$ ) are presented. The measurements indicate high variations on the measured  $C_p$  values spatially along the façades due to the microclimatic effect. The measured wind pressure coefficients present also significant fluctuations over time. The use of fluctuating  $C_p$  values on the calculation of air infiltration by means of the Monte Carlo method is investigated. The accuracy of incorporating fluctuating  $C_p$  values into the calculation of air changes is determined, and is also compared with other conventional methods.





3.3	Wind-induced pressure variations.....	49
3.4	Building-specific wind pressure coefficients.....	54
3.5	Improving the accuracy of air infiltration calculation.....	59
3.6	Fluctuating wind pressure coefficients.....	63
<b>4.</b>	<b>Conclusions, limitations and further research.....</b>	<b>68</b>
	<b>References.....</b>	<b>73</b>
	<b>Papers (<i>individual numbering</i>).....</b>	<b>86</b>

# 1. Introduction

It is well established that the building stock globally is responsible for 40% of the total energy consumption and 36% of the greenhouse gas emissions.

The European Commission first introduced the EU's energy efficiency policy in 2012 that led the way towards nearly-zero energy buildings (nZEB) by the end of 2020 (European Commission 2010; 2012; 2018). At the dawn of 2020, terms such as 'nearly-zero energy buildings' and 'zero energy buildings' are becoming mainstream and already the challenge has progressed even further, towards the development of zero-energy neighbourhoods and zero-emission neighbourhoods (Cacha et al., 2019; Skaar et al., 2018; Marique and Reiter, 2014; Orehounig et al., 2014). Furthermore, modern cities aim to modernize not only their building sector, but also their transportation and infrastructure by transitioning to clean energy (Jacobson et al., 2018; Ma et al., 2018; Notton et al., 2017; Anthopoulos et al., 2016; Kohler et al., 2009; Yuan et al., 2015).

Oslo is the fastest-growing capital in whole Europe and this rapid growth led to a vast reconstruction need and architectural rise. Oslo is also the European Green Capital in 2019 as it aims to create sustainable solutions to deal with its rapid growth. Pilot programs that include the upgrade of existing neighbourhoods into zero-emission neighbourhoods and nearly-zero energy neighbourhoods is one of the measures taken towards a more sustainable future (FME ZEN, 2018; ZenN, 2013; Zen, 2014). The goal for a car-free city centre and the bold subsidy of electrical cars is another measure towards lower CO<sub>2</sub> emissions (SSB, 2018; EVUE, 2015; Berroir et al., 2018; Ajanovic and Haas, 2016; Høyer, 2008). According to the municipality's agenda, Oslo plans to reduce the municipality emissions by 95% by 2030 and aims to set an example for sustainable urban development with solutions that can be applicable for many European cities.

Today, 78% of the total energy consumption in Norwegian households is covered by electricity, and almost the total amount of electricity production is derived from renewable sources, such as hydro and wind power (SSB, 2014; 2018). The increasing number of hybrid and electric cars in the city of Oslo automatically creates an extra electricity demand. The correct management and distribution of energy becomes essential (Lund et al., 2015; Calvillo et al., 2016; Bonnema et al., 2015). Therefore, the improvement of the energy demands prediction in a neighbourhood scale becomes a necessity for the

green cities of the future, as it will facilitate the energy distribution on the grid and avoid potential problems, such as electricity deficits and blackouts. However, contemporary norms address only the energy consumption at individual building level and usually regard the surroundings.

The development of zero-energy and zero-emission neighbourhoods does not revolve only around lowering the energy demands and the greenhouse gas emissions. The preservation of the architectural identity and the design of aesthetic solutions play an important role for both the city and the inhabitants (Kellert, 2005; Andersen, 2015; Xu et al., 2019). The use of local materials that are linked with the building tradition, such as wood in the Nordic countries, seems like a promising and trending sustainable solution that can contribute towards the reduction of the CO<sub>2</sub> footprint and increased life-cycle (Woodard and Milner, 2016; Nordwall and Olofsoon, 2019; Nadoushani et al., 2017; Saleem et al., 2018). However, such materials are susceptible to degradation caused by the natural weathering process. The ability to predict the potential deterioration caused by the local micro-scale climate can improve the decision-making process during the design phase and increase the life cycle of buildings, thus leading one more step closer sustainability. Once again, standard methods usually treat the hygrothermal performance of the building envelope uniformly and one-dimensionally, thus omitting any spatial microclimatic effect caused by the surroundings on the building façades.

Basic keystones in mitigating climate change and achieving sustainability include: (1) energy efficiency, (2) increased durability and life-cycle of building materials and (3) low greenhouse gas emissions. Contemporary norms address only the energy consumption at individual building level and usually regard the surroundings. They also treat the hygrothermal performance of the building envelope uniformly and one-dimensionally, thus omitting any spatial microclimatic effect caused by the surroundings on the building façades. Inspired by the leading example of the Norwegian capital and urged by the contemporary imperative for sustainability, this PhD study aims to explore such aspects of the building performance simulation with respect to the local micro-scale. Increased prediction accuracy can help towards the sustainable development direction, as it can improve the quality of both the design and retrofitting phase of buildings.

## 1.1 Building performance

Building performance expresses how well a building performs with regards to its energy demands, indoor air quality, operational functions, durability, safety and environmental impact. A building with ideal performance should fulfil all the above terms of efficiency, comfort and safety. Developing sustainable establishments is inextricably linked with designing buildings with high building performance. However, the design of high quality building performance consists a complex process as it combines so many different aspects. Computational methods (i.e. simulations) is an invaluable tool that can facilitate the building design phase by simulating the engineering problems of realistic cases. More specifically, building performance simulations employ physics laws and numerical methods, and by assuming boundary conditions, are able to provide an approximate solution for an actual problem in the real world (Hensen and Lamberts, 2011). In praxis, most simulation tools focus mainly on one aspect of the building performance, such as energy consumption or hygrothermal conditions of the building envelope, since it is rather complicated to balance the various physical phenomena (Woloszyn and Rode, 2008). However, building performance simulation has been constantly developing the past 50 years and is able to combine appropriate input from various scientific fields, such as physics, mathematics, material science, biophysics, as well as human behavioural, environment and computational sciences, in order to approximate as closely as possible the reality (Hensen and Lamberts, 2011; Becker, 2008). Heat, Air and Moisture (HAM) transport are interrelated physical phenomena that govern the building performance. Contemporary whole-building HAM simulation tools can balance adequately the various physical phenomena and produce high accuracy prediction regarding energy consumption, building envelope hygrothermal conditions and indoor climate (Woloszyn and Rode, 2008; Rode and Grau, 2010).

## 1.2 Climatic loads

Besides the physical phenomena, the weather conditions are another key parameter during the building performance simulation (Figure 1.1). The weather conditions introduced as an input to the simulation determine the climate-driven loads acting on the building examined and set the necessary boundary conditions for the simulation models (Barnaby and Crawley, 2011).

The climate-driven or climatic loads are a category of live loads that are imposed on structures as the result of the dynamic driving functions of ambient temperature, humidity, wind, solar radiation, precipitation, snow, and they are crucial to the building performance (Hunn, 1996). The current PhD project has focused on the climate-driven loads imposed by wind, wind-driven rain and solar radiation, and their impact on the building performance was researched.

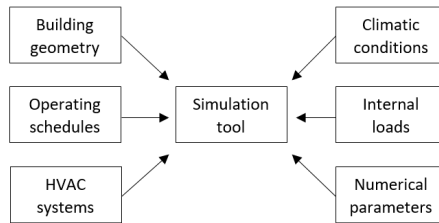


Figure 1.1. Overview of data required to perform building performance simulation (redrawn from Nugraha et al., 2013)

### 1.2.1 Wind

Wind is basically moving air. When wind impinges on a structure, the dynamic energy is transformed into pressure, and pressure acting on surface is directly translated to forces. Wind forces acting on buildings are crucial for its structural integrity, and wind-induced pressurization is also important for natural ventilation, operation and safety of the building. More specifically, wind-induced pressures is one of the driving mechanisms of air infiltration in buildings, along with stack effect and the potential existence of mechanical ventilation systems (Lyberg, 1997). Buildings with mechanical ventilation systems employ inlet and extract fans to maintain the internal air at the same pressure levels as outside, thus minimizing the air infiltration (Kragh et al., 2005). On the other hand, the design of natural ventilation depends on the wind-induced pressure variations along the building envelope (Karava et al., 2007).

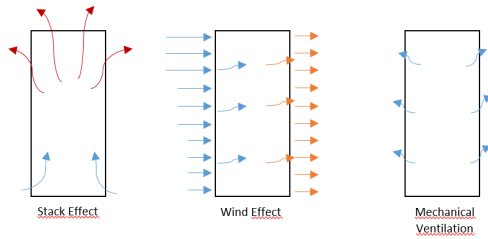


Figure 1.2. Air infiltration driving mechanisms (redrawn from Straube, 2007)

Air infiltration is defined as the phenomenon of air flow through the building envelope and its openings. Air infiltration is crucial for the building performance as it affects aspects such as the energy demands, indoor air quality, mould growth and thermal comfort (Straube, 2007). Air infiltration is mainly affected by the building's airtightness level. More significantly, for buildings with low airtightness, air infiltration is crucial to the total building energy balance as it can account for up to 25%-40% of the total heating load (Younes et al., 2011; Jokisalo et al., 2008; Liddament, 1996). Even though most modern buildings have quite tight building envelopes, it was found that in some cases, the airtightness is overestimated, and air infiltration can still account for up to 15% of the total heating load (NIST, 1996). In most cities, the majority of the building stock consists of old and rather leaky buildings. The accurate prediction of the air infiltration rates of such existing buildings can lead to more accurate prediction of energy demands.

Wind is considered the dominant driving mechanism of air infiltration, especially when the temperature gradients are small or the height of the building is small resulting in low buoyancy forces (Shaw, 1981)(Figure 1.3). In order to succeed high accuracy of air infiltration prediction, the wind flow around a building, and consequently the wind pressures acting on the building should be determined as realistically as possible. Wind flows around buildings are complex and depend on a variety of factors, such as architecture, terrain, surroundings, and climatic characteristics of the location. Wind is also a very dynamic phenomenon and just considering averaged values over time is an oversimplification that has great impact on the overall building performance. Wind storms and gusts can impose great forces on the structure and even increase significantly the air infiltration rates (Haghighat et al., 2000; Etheridge, 2000; Kraniotis et al., 2014). Tall, slender structures are susceptible to dynamic

wind loads, while low-rise buildings are usually examined only under static wind loads (Mendis et al., 2007).

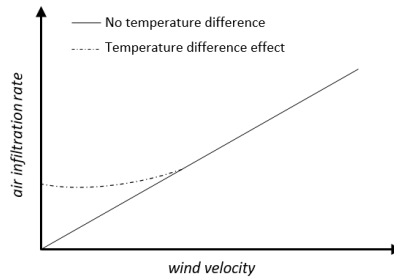


Figure 1.3. Significance of wind (redrawn from Liddament, 1986)

### 1.2.2 Wind-driven rain

Wind-driven rain (WDR) is rain that is given a horizontal velocity component by the wind and falls diagonally (obliquely). WDR is important for the building performance, as it is the most important moisture source affecting the hygrothermal performance and durability of building façades. WDR can be responsible for a variety of construction problems, such as moisture accumulation in porous materials, frost damage, moisture induced salt migration, mould growth, discoloration and structural cracking (Abuku et al., 2009; Tang et al., 2004; Blocken and Carmeliet, 2004; Blocken et al., 2007; Janssen et al., 2007; Abuku et al., 2009; Tariku et al., 2007; Thiis et al., 2017, Lie et al., 2018). The amount of wind driven rain impinging on a building façade depends on a plethora of parameters, such as the building surroundings and geometry, topology, position on the building façade, wind speed, wind direction, turbulence intensity, rainfall intensity, raindrop size distribution and rain event duration, rendering thus WDR as a highly complex phenomenon (Blocken and Carmeliet 2004).

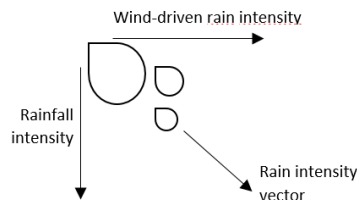


Figure 1.4. Wind driven rain (redrawn from Blocken and Carmeliet, 2004)

Field measurements and wind tunnel testing throughout the years have revealed several features of what is nowadays known as the 'classic' wetting pattern of building façades. The windward façade is wetted whereas the other façades remain relatively dry. At the windward façade, the wetting increases from bottom to top and from the middle to the sides; the top corners are most wetted, followed by the top and side edges. For high and wide buildings, most of the windward façade only receives little WDR, except for the corner and the top and side edges. The WDR intensity at a given position increases approximately proportionally with the wind speed and the horizontal rainfall intensity (Blocken and Carmeliet, 2004).

### 1.2.3 Solar radiation

Solar radiation is high-energy electromagnetic radiation 250 to 4000 nm in wavelength, including the near-ultraviolet (UV), visible light and near-infrared (IR) radiation. The visible light lies between 400 and 780 nm, where the UV and the IR lie below and above the visible region correspondingly. The UV light is further divided into three subregions: UV-A (315-380 nm), UV-B (280-315 nm) and UV-C (100-280 nm) (Iqbal, 1983).

The total solar radiation – usually referred to as global – consists of direct and diffuse radiation. As the wording implies, direct radiation describes solar radiation travelling in straight line, while diffuse radiation describes the solar radiation that has been scattered in various directions due to molecules and particles in the atmosphere. Under clear sky, the direct radiation is very high, while under atmospheric conditions, such as clouds and pollution, the diffuse radiation is much higher. Direct and diffuse radiation depend on both the geographic location (latitude, longitude) and the climate of a region. The total amount of both direct and diffuse solar radiation incident on a surface is influenced by location, surface facing angle and tilt, as well as by the surface's surroundings.

Solar gains are significant for the thermal loads of buildings. Direct solar gains include sunlight entering the building through windows, while indirect solar gains refer to solar radiation increasing the surface temperature of exterior building elements or the energy getting stored in the thermal mass of the building (Figure 1.5). Solar gains should be taken into consideration during the



design phase since they are essential to the hygrothermal performance of the building envelope, daylight and thermal comfort.

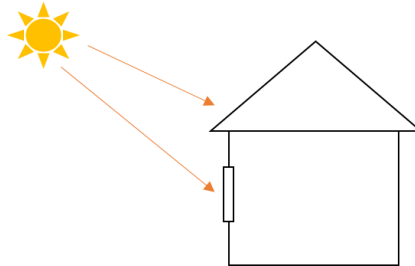


Figure 1.5. Direct and indirect solar gains

Primarily, solar radiation impinging on a building surface (solar irradiation) has an immediate impact on the external surface of the building envelope. The heat balance of the exterior building surface is a function of incident radiation, conduction and convection. Since shortwave radiation is high-energy radiation, the incident solar radiation on a surface can heat up significantly the external surfaces of the building and introduce a dominant radiation heat flux through the building envelope (McClellan and Pedersen, 1997; Chwieduk, 2009; Li and Lam, 2000; Lam et al., 2005; Lee et al., 2013; Lam and Li, 1999). However, only a fraction of the solar incident radiation is absorbed by the external surface. The amount of absorbed radiation depends on the material properties, and more specifically on the material absorptivity. The absorption coefficient of the material should always be chosen after careful consideration, as heat fluxes and surface temperatures strongly depend on it (Kontoleon and Bikas, 2007; Mazzeo et al., 2016). High external surface temperatures caused by solar irradiation can induce biological activity on the façade materials, as well as discoloration and degradation of the surface building materials (Sedlbauer, 2002; Feist, 1989).

The ultraviolet radiation, which is the high-energy part of the solar spectrum, has documented damage effect on materials. Especially building materials, such as wood, plastic and paint, are particularly vulnerable due to large exposure to solar radiation. The degradation of building materials can vary from discoloration to extensive loss of mechanical properties (Andrady et al., 1998; Andrady et al., 2011; Berdahl et al., 2008). Therefore, it can significantly affect the materials' life cycle not only aesthetically, but also in terms of performance.

### 1.3 Microclimate

All the aforementioned climatic loads – wind, wind-driven rain, solar radiation – significantly affect aspects of the building performance. Furthermore, these climatic loads are substantially influenced by the local weather conditions, the local topography, and the building’s surroundings and geometry. In other words, they are affected by the microclimate (Figure 1.6). As a result, the building performance depends at a large extent on the microclimate, since the latter determines largely the climatic loads acting on the building.

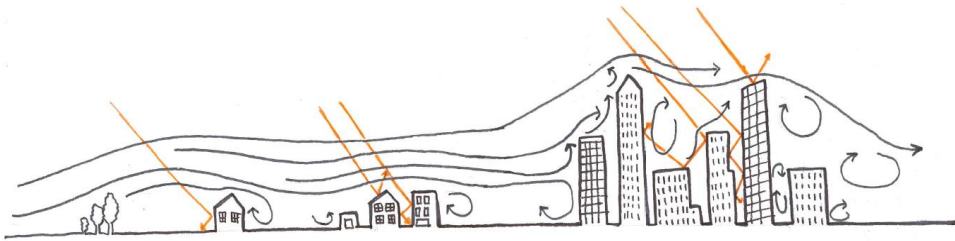


Figure 1.6. Microclimate effect on the climatic loads of wind and solar radiation acting on buildings (original drawing by Aleksander Lundby).

The effect of microclimate on the energy and hygrothermal performance of the building has already been documented (Moonen et al., 2012; Allegrini et al., 2012; Allegrini et al., 2013; Priyadarsini et al., 2009; Oxizidis et al., 2011; Stewart and Oke, 2012;). The increasing growth rates and urban development tend to expand a city’s boundaries and develop new urban areas with characteristic morphologies (Ren et al., 2016). Especially in large cities, the urban and suburban typologies can vary significantly, and consequently the corresponding microclimates can differ from neighbourhood to neighbourhood (Figure 1.7). Similarly, rural places can also be governed by different microclimates according to their morphology (Figure 1.7).

In an ideal case, the weather data that would be used in building performance simulations would be observed exactly at the project site investigated and be subject to the local microclimate (Barnaby and Crawley, 2011). However, it is rarely possible to have all the necessary environmental data for building performance simulation collected on-site. Therefore, other methods are usually

employed in order to introduce the microclimatic boundary conditions into building performance simulation and subsequently increase the prediction accuracy.

Some of the studies that aim to introduce microclimate on the building performance simulation employ computational fluid dynamics (CFD) simulations. As a result, they manage to define the air flows and air temperatures around buildings, and alternate accordingly the typical climate data used in the building performance simulations (Nikkho et al., 2017; Pisello et al., 2015). Most scientific reports focus on the determination of building specific convective heat transfer coefficients (CHTC) through CFD simulations. The CHCT can be incorporated on the building performance simulations and help quantify the microclimatic effect on the building performance (Allegrini et al., 2013; Malys et al., 2015; Gobaki and Kolokotsa, 2017; Dorer et al., 2013; Vallati et al., 2015). Other suggested methods for improving the building performance simulation with regards to microclimate include: (1) the generation of specific weather datasets from urban microclimate simulations; (2) using experimental data to calibrate simulation inputs, such as velocity profile and discharge coefficients for natural ventilation; (3) heat removal by wind and buoyancy (Tsoka et al., 2017; Shirzadi et al., 2019; Allegrini et al., 2015).

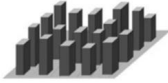
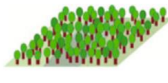



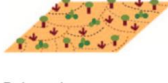



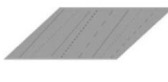
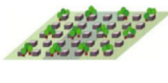
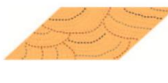
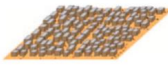




Built types	Definition	Land cover types	Definition
1. Compact high-rise 	Dense mix of tall buildings to tens of stories. Few or no trees. Land cover mostly paved. Concrete, steel, stone, and glass construction materials.	A. Dense trees 	Heavily wooded landscape of deciduous and/or evergreen trees. Land cover mostly pervious (low plants). Zone function is natural forest, tree cultivation, or urban park.
2. Compact midrise 	Dense mix of midrise buildings (3–9 stories). Few or no trees. Land cover mostly paved. Stone, brick, tile, and concrete construction materials.	B. Scattered trees 	Lightly wooded landscape of deciduous and/or evergreen trees. Land cover mostly pervious (low plants). Zone function is natural forest, tree cultivation, or urban park.
3. Compact low-rise 	Dense mix of low-rise buildings (1–3 stories). Few or no trees. Land cover mostly paved. Stone, brick, tile, and concrete construction materials.	C. Bush, scrub 	Open arrangement of bushes, shrubs, and short, woody trees. Land cover mostly pervious (bare soil or sand). Zone function is natural scrubland or agriculture.
4. Open high-rise 	Open arrangement of tall buildings to tens of stories. Abundance of pervious land cover (low plants, scattered trees). Concrete, steel, stone, and glass construction materials.	D. Low plants 	Featureless landscape of grass or herbaceous plants/crops. Few or no trees. Zone function is natural grassland, agriculture, or urban park.
5. Open midrise 	Open arrangement of midrise buildings (3–9 stories). Abundance of pervious land cover (low plants, scattered trees). Concrete, steel, stone, and glass construction materials.	E. Bare rock or paved 	Featureless landscape of rock or paved cover. Few or no trees or plants. Zone function is natural desert (rock) or urban transportation.
6. Open low-rise 	Open arrangement of low-rise buildings (1–3 stories). Abundance of pervious land cover (low plants, scattered trees). Wood, brick, stone, tile, and concrete construction materials.	F. Bare soil or sand 	Featureless landscape of soil or sand cover. Few or no trees or plants. Zone function is natural desert or agriculture.
7. Lightweight low-rise 	Dense mix of single-story buildings. Few or no trees. Land cover mostly hard-packed. Lightweight construction materials (e.g., wood, thatch, corrugated metal).	G. Water 	Large, open water bodies such as seas and lakes, or small bodies such as rivers, reservoirs, and lagoons.
8. Large low-rise 	Open arrangement of large low-rise buildings (1–3 stories). Few or no trees. Land cover mostly paved. Steel, concrete, metal, and stone construction materials.	<b>VARIABLE LAND COVER PROPERTIES</b>	
9. Sparsely built 	Sparse arrangement of small or medium-sized buildings in a natural setting. Abundance of pervious land cover (low plants, scattered trees).	<i>b. bare trees</i>	Leafless deciduous trees (e.g., winter). Increased sky view factor. Reduced albedo.
10. Heavy industry 	Low-rise and midrise industrial structures (towers, tanks, stacks). Few or no trees. Land cover mostly paved or hard-packed. Metal, steel, and concrete construction materials.	<i>s. snow cover</i>	Snow cover > 10 cm in depth. Low admittance. High albedo.
		<i>d. dry ground</i>	Parched soil. Low admittance. Large Bowen ratio. Increased albedo.
		<i>w. wet ground</i>	Waterlogged soil. High admittance. Small Bowen ratio. Reduced albedo.

Figure 1.7. Local climate zone scheme based on urban/suburban/rural morphology (Stewart and Oke, 2012, © American Meteorological Society. Used with permission)

## 1.4 Research Objectives

Summarizing, the total climatic load of wind, wind-driven rain and solar radiation reaching a building is significantly affected by the microclimate. Taking into consideration a building's geometry and the microclimate it belongs to, the exact amount of climatic loads enforced on the building's façades can be determined with spatial accuracy.

Two important building attributes that play a significant role to the overall building performance are the air infiltration of the building (Younes et al., 2011; Jokisalo et al., 2008; Liddament, 1996) and the external surface hygrothermal conditions, and both are strongly dependent on climate-driven loads.

The micro scale determines the air-flow around a building, and the air flow will determine the wind-induced pressurization of the building. The wind-induced pressurization of a building in turn, is the dominant driving mechanism of the air infiltration in old and leaky buildings, and air infiltration plays a major role in the overall energy demands of such buildings. Therefore, knowing the wind induced pressures with respect to microclimate on such buildings can help determine more accurate air infiltration rates and plan strategies that can improve their overall building energy performance. Furthermore, higher accuracy on the energy demand calculation with respect to microclimate can potentially help with the energy distribution at a neighbourhood level within the boundaries of a city.

The micro scale also affects the amount of solar-radiation and wind-driven rain impinging on the building surfaces. These loads can significantly affect the heat and moisture transport through the building envelope, as well as induce biological growth, discoloration and degradation of the façade materials. The microclimate in combination with the building's geometry and architecture can define sheltered and exposed areas on the building façades. Therefore, the surface hygrothermal conditions can be determined spatially along the building façades, revealing significant variations, interesting patterns and high-risk areas.

Introducing appropriate microclimatic boundary conditions into simulation models for buildings can significantly improve the accuracy of the building energy prediction and contribute to more efficient decision-making during the building design phase that can increase the durability and life cycle of the construction.

In this context, the research objectives of this PhD study can be summarized as following:

- Determine climatic loads, such as solar radiation, wind and wind-driven rain, reaching a building by taking into account the microclimate and the building's geometry. Determine the microclimatic loads spatially along the building façades (Paper I, II, III, IV, V).
- Predict how the surface hygrothermal conditions (temperature and moisture content) vary spatially along a building's façades by taking into consideration the microclimate and the spatial architectural characteristics of the building (Paper I).
- Determine the wind-induced pressure variations along a building's façades by taking into consideration the microclimate and the building geometry (Paper II, III, IV, V). Determine spatially over each façade building-specific wind pressure coefficients with respect to microclimate (Paper II, IV, V).
- Investigate the use of building-specific wind pressure coefficients as appropriate boundary conditions to account for the microclimate in the calculation of air infiltration in buildings (Paper II, IV, V).
- Compare the use of building-specific wind pressure coefficients as microclimatic boundary conditions on building energy simulations with common practice methods (Paper II, IV). Research the accuracy of each method by cross validating them with on-site measurements (Paper II, IV).
- Investigate the suitability of fluctuating wind pressure coefficients for the calculation of air infiltration. Explore the accuracy of fluctuating  $C_p$  and mean  $C_p$  values on the calculation of airflows by comparing them with on-site measured data (Paper V).

## 2. Methodology

In order to investigate and achieve all the research objectives presented above, a set of on-site measurements and numerical simulations were organised and performed. The microclimatic effect on both the exterior surface of the building envelope and the air infiltration through the building envelope was explored. Figure 2.1 presents schematically the overview of the methodology used in the framework of the current PhD project.

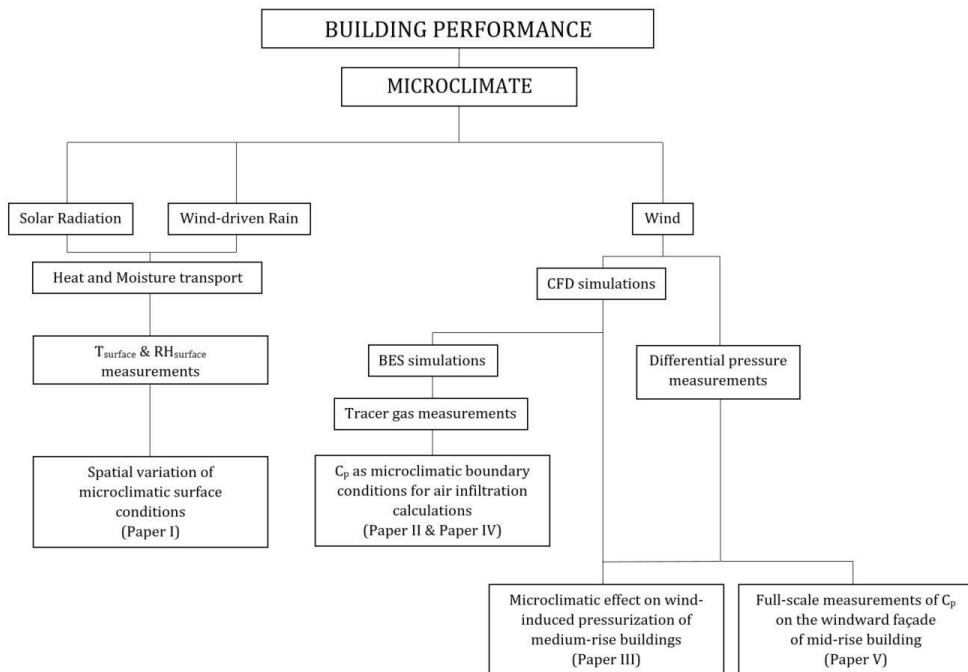


Figure 2.1. Schematic overview of the methods employed and research objects reached.

### 2.1 The experimental sites

Various on-site measurements were performed for the purposes of the research work conducted within the framework of the PhD and are presented in this thesis. In total five different buildings, where the measurements took place, were used as reference cases. Each one of them – or in some cases two of the buildings - was used for a specific research project that constitutes part of

this thesis. All the reference buildings are situated in the rural town of Ås, Norway (59.66°N, 10.78°E).

Furthermore, the weather data used in every research study under this PhD project were collected in the local meteorological station. The meteorological station belongs to the Norwegian University of Life Sciences (NMBU) and is also located in Ås, Norway. The meteorological station is placed in a field of an area of approximately 50000 m<sup>2</sup>, where advanced meteorological equipment is installed. The meteorological station consists a fully automated field laboratory with extensive logging and measuring equipment for continuous recordings of meteorological observations, energy conversion, radiation measurement, soil temperature profiles, lysimetry etc. 24-hour observations are recorded from over 50 instruments. Instruments and logging systems are subject to daily supervision and manual control routines. The meteorological field is considered as open terrain since its surface consists mainly of grass and there are no fences and buildings in close proximity (Figure 2.2).



Figure 2.2. The meteorological field of NMBU (in the red square) and its surroundings. (Google Maps, 2019)

### 2.1.1 The timber and masonry façades

Surface temperature and RH measurements were performed in two different building façades: i) a building with timber façade (Figure 2.3.a) and ii) a building with masonry façade (Figure 2.3.b).



The building with the timber façade belongs to the local high school (Ås Videregående skole). The two-storey building was erected in 2010 and consists of a highly insulated and airtight building envelope. The timber cladding is made of aspen (*populus tremula*) of 30 mm thickness. A layer of stagnant air exists between the cladding and the building envelope. The area of the timber façade investigated has a length of approximately 45 m and a height of 7 m.

The one-storey masonry building belongs to NMBU and is used as storage space for robotic equipment. The construction consists of a massive masonry wall. The exterior façade of the building is made of red clay fire bricks, which have a typical thickness of 80 mm. The area of the masonry façade investigated has a length of approximately 8 m and a height of approximately 5 m.

For more details regarding the reference buildings and the materials, the reader is referred to Paper I.

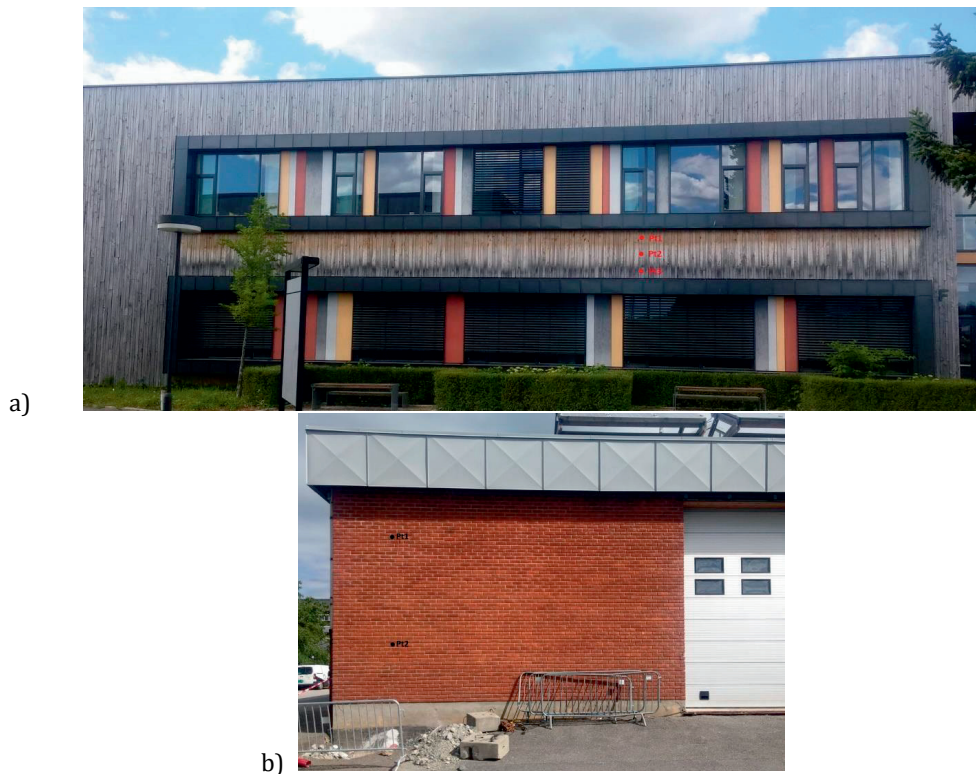


Figure 2.3. The two buildings used for surface temperature and RH measurements.

### 2.1.2 The main building of the meteorological station

The main building of the meteorological station belongs to NMBU and is located on the meteorological field at Ås, Norway (Figure 2.4.a). Therefore, it is considered fully exposed in open terrain. The building's long axis runs North-South with a deviation angle of  $6.5^\circ$ . The building is a one-storey light timber construction and consists of an insulated room, a non-insulated garage space, and a cold attic (Figure 2.4.b).

The office space of this building was used for tracer gas measurements. The inner dimensions of the office room are  $3.85\text{m} \times 2.55\text{m} \times 2.10\text{m}$ , which result to a total inner volume of  $20.6\text{ m}^3$ . The office space includes two window openings, one door that connects it with the garage space, an air vent of area of  $0.023\text{ m}^2$ , and a large hole of area of  $0.0025\text{ m}^2$  (used for cables). The vent, the hole, as well as the joints alongside the windows were considered as air leakages in the relevant study. During the measurements the office door was closed but not sealed, therefore the joints around the door was also taken into account as potential leakage.

For more details regarding the reference building, the reader is referred to Paper IV.

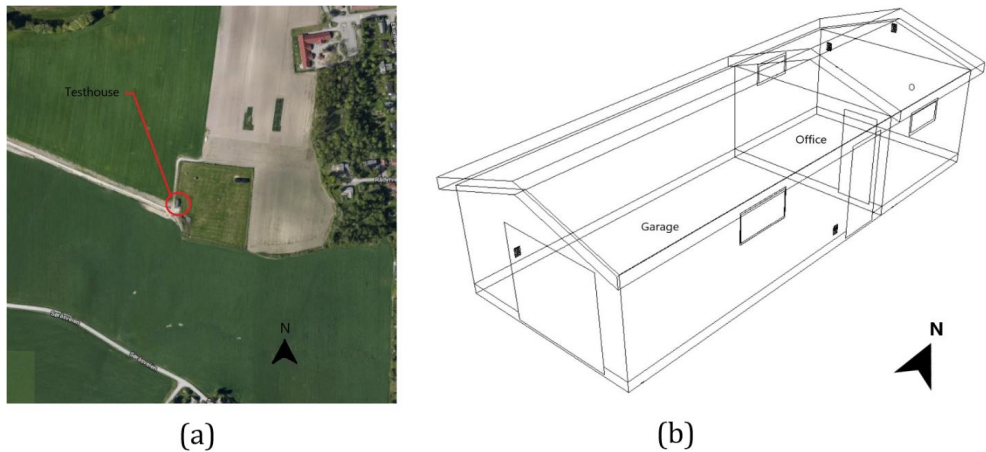


Figure 2.4. The main building of the meteorological station used for tracer gas measurements. (a) position on the meteorological field (red circle) and its surrounding (Google Maps, 2018); (b) perspective drawing showing the existing room spaces.

### 2.1.3 The twin medium-rise building complex

Full-scale pressure measurements were conducted in a twin medium-rise building complex situated in Ås, Norway. The twin buildings are partially surrounded by low-rise buildings and are located next to a forest area (Figure 2.5.a).

The building complex was built in 2013 and the twin buildings are built from Cross Laminated Timber (CLT). The two identical buildings have simple geometry of rectangular prism and consist of eight storeys, resulting in a total building height of approximately 25 m (Figure 2.5.b). Their long-axes run East-West and the twin buildings are almost parallel to each other. The North Building's long axis is completely aligned to the East-West direction, while the South Building's long-axis deviates by an angle of  $10^\circ$  from the East-West direction. The twin buildings have an average distance of 12 m between them, with 10 m being the shortest intermediate distance and 14 m the longest intermediate distance.

For more details, the reader is referred to Paper III and Paper IV.

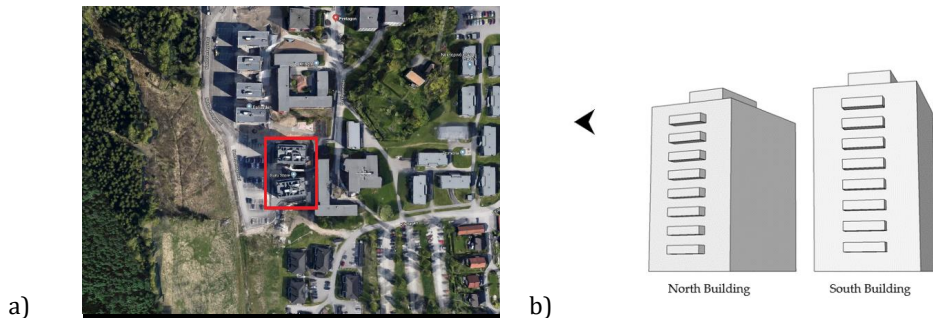


Figure 2.5. The twin medium-rise building complex where differential pressure measurements were performed. (a) Satellite view of the twin buildings (red square) and their surroundings (Google Maps, 2018); (b) perspective drawing of the twin buildings.

## 2.2 Numerical Simulations

### 2.2.1 Computational Fluid Dynamics

Computational Fluid Dynamics (CFD) is a branch of fluid mechanics that uses numerical analysis and data structures to solve and analyse problems that involve fluid flows. CFD simulations for engineering applications have been extensively developed and advanced the last 50 years (Blocken, 2014).

Some of basic topics have been of interest since the rising of the field and huge progress has been made on them the past decades. These are the simulation of the Atmospheric Boundary Layer (ABL) that is a fundamental prerequisite for accurate simulation of wind-flow around structures, bluff-body aerodynamics, which is basically the application of CFD for analysing fluid mechanical/physical processes of wind flow around buildings, and turbulence modelling (Blocken, 2014). As a result, nowadays CFD simulations can help predict with high accuracy, among others, velocity and pressure fields around structures, and consist a powerful tool in analysing fluid-structure interaction. 50 years of progress have significantly contributed into the development of more accurate and precise numerical analysis, development of advanced solving algorithms and sophisticated turbulence models. The increased availability of CFD codes with user-friendly graphical interfaces, as well as the increased computational capacity, has made CFD simulations popular and frequently applied for the calculation of wind loads. However, the use of CFD techniques without proper knowledge of fluid dynamics can lead to misuse of CFD and large errors (Blocken, 2014). The Architectural Institute of Japan (AIJ), as well as the European COST Action, provide guidelines for the correct use of the numerical parameters and boundary conditions that can help the user quality-assure their applications (Mochida et al., 2006; Tominaga et al., 2008; COST Action 732, 2007).

In the current PhD project, CFD simulations were performed for the determination of the wind-induced pressure variations on building façades (Paper II & Paper IV). The wind-induced pressure on the building envelope is critical for the building's air infiltration (Lyberg, 1997). Knowing the spatial wind-induced pressure variations on a building can help define appropriate wind-pressure coefficients, which can be later introduced in the building energy simulations and define the wind-induced air infiltration (Costola et al., 2009).

For both studies, the steady Reynolds-Averaged Navier-Stokes (RANS) equations were employed for determining the wind pressure variations on the façades of the examined reference buildings. The three-dimensional steady RANS equations were solved in combination with the two-equation standard  $k-\epsilon$  turbulence model. The use of steady RANS equations in combination with the  $k-\epsilon$  turbulence model for predicting mean wind pressure distributions on buildings has been validated against experimental data, and was found to be a

rather accurate method for different building geometries (Montazeri and Blocken, 2013; Yang et al., 2006; Tominaga et al., 2015; Delaunay et al., 1995; Murakami and Mochida, 1988). The Semi-Implicit Method for Pressure Linked Equations (SIMPLE algorithm) was used for the velocity-pressure coupling (Versteeg and Malalasekera, 2007). Second-order discretization schemes were used for both the convection and viscous terms of the governing equations. Since turbulence models, such as the k-e, are only valid for the area where turbulence is fully developed, wall functions were employed for the ground and building surfaces in order to model the near wall region (Liu, 2016).

The vertical profiles for the mean wind velocity  $U$ , turbulent kinetic energy  $k$  and dissipation rate  $\varepsilon$  were defined as boundary conditions and applied at the inlet of the domain according to the COST recommendations (COST Action 732). The inlet boundary conditions assume constant shear stress with height and are considered acceptable for cases that computational domain is lower than the atmospheric boundary layer (Tominaga et al., 2008; Delaunay et al., 1995). A logarithmic wind profile was assumed, where the roughness class and length of the area around the reference buildings was taken into consideration. The logarithmic wind profile is based on the following equation:

$$U_z = U_h \frac{\ln\left(\frac{z}{z_0}\right)}{\ln\left(\frac{h}{z_0}\right)} \quad (2.1)$$

Where  $U_h$  [m/s] is the reference speed measured at height  $h$  [m] and  $U_z$  [m/s] is the wind speed at height  $z$  [m].  $z_0$  is the roughness length [m] that corresponds to the area around the reference building.

The vertical profiles for turbulent kinetic energy  $k$  [m<sup>2</sup>/s<sup>2</sup>] and dissipation rate  $\varepsilon$  [m<sup>2</sup>/s<sup>3</sup>] were calculated based on the equations suggested by Richards and Hoxey (1993) and are given by the following equations:

$$k_z = \frac{U_{ABL}^2}{\sqrt{C_\mu}} \quad (2.2)$$

$$\varepsilon_z = \frac{U_{ABL}^3}{\kappa(z + z_0)} \quad (2.3)$$

Where  $\kappa$  is the Karman constant (=0.4) and  $U_{ABL}$  [m/s] is the atmospheric boundary layer friction velocity given by the following formula:

$$U_{ABL} = \frac{\kappa U_h}{\ln\left(\frac{h + z_0}{z}\right)} \quad (2.4)$$

Where  $U_h$  [m/s] is the specified velocity at reference height  $h$  [m].

Furthermore, for all studies where CFD simulations were performed (Paper II, Paper III, Paper IV), the computational domain sizes were defined according to the best practice guidelines (Tominaga et al., 2008; COST Action 732, 2007).

For more details regarding the inflow boundary conditions, computational domains, grid sensitivity analysis, the reader is referred to Paper II, Paper III and Paper IV.

### 2.2.2 Building Energy Simulation

Building Energy Simulation (BES) are used to predict the energy performance of buildings based on a set of physics laws, such as energy and mass balance, coupled heat and moisture transport, etc. (Coackley et al. 2014). For the purpose of this PhD project, BES were employed in order to determine the wind-induced air infiltration for the reference building investigated (Paper II & Paper IV). A third-party graphical user interface for EnergyPlus was used.

The common practice for determining air infiltration rates during BES is based on the building's air leakage number. According to the European Standard for Heating Systems in Buildings EN12831:2003, the air infiltration flow rate of a heated space due to wind and stack effect can be calculated from the following formula:

$$V_{inf} = 2 \cdot V \cdot n_{50} \cdot e \cdot i \quad (2.5)$$

Where

$V_{inf}$  = the air infiltration rate [m<sup>3</sup>/h]

$V$  = the volume of the heated space [m<sup>3</sup>]

$n_{50}$  = the air leakage number at 50Pa [h<sup>-1</sup>]

$e$  = a shielding coefficient

$i$  = a height correction coefficient

The air leakage number  $n_{50}$  describes the air changes per hour that are the result of a pressure difference of 50 Pa between the inside and the outside of the building, including the effects of air inlets (EN12831:2003). The air leakage number  $n_{50}$  can be measured through a fan pressurization test as described on

NS-EN ISO 13829. However, national annexes to the standard provide databases with characteristic values for  $n_{50}$ . The standard database comprise fan pressurization data that have been collected through the years and that are classified in different typical categories based on common factors, such as building typology, height and age of construction.

EnergyPlus calculates infiltration load based on design infiltration rate ( $I_{design}$ ), schedule fraction ( $F_{schedule}$ ), temperature difference between the zone and outdoor air, and wind speed, using the following basic equation:

$$Infiltration = I_{design} * F_{schedule} * (A + B * |T_{zone} - T_{odb}| + C * Windspeed + D * Windspeed^2) \quad (2.6)$$

The four coefficients A, B, C and D can be defined by users in order to account for the effect of microclimate conditions of temperature and wind speed at each simulation time step (EnergyPlus™ Documentation, 2017). The default values are set to 1, 0, 0, and 0, which gives a constant flow of infiltration under all conditions. The design volume flow rate (noted as  $I_{design}$  in the above equation) corresponds to the maximum amount of infiltration expected at design conditions and is the air infiltration rate calculated using the air leakage number  $n_{50}$ . The resulting volume flow rate is converted to mass flow using the current outdoor air density at each time step.

More advanced infiltration calculations are possible using the EnergyPlus and include the use of wind pressure coefficients  $C_p$ .

The air flow rate through the building envelope is driven by pressure differences due to wind and stack effect and can be described by the following power law equation:

$$Q = C \cdot \Delta P^n \quad (2.7)$$

Where

- $Q$  = the volumetric air flow through the building [ $m^3/s$ ]
- $C$  = flow coefficient related to the size of opening/cracks in the building envelope
- $\Delta P$  = total pressure difference across the construction including wind pressure and stack effect [Pa]
- $n$  = flow exponent varying between 0.5 for fully turbulent flow and 1.0 for fully laminar flow

Characteristic flow coefficients and flow exponents are defined for each component of the buildings, such as openings, walls, doors, floors, ceilings and

roofs. Relevant crack data can be found on the 'Numerical Data for Air Infiltration and Natural Ventilation Calculations' by AIVC (Orme et al., 1998). In order to calculate the pressure difference over the building envelope, the wind-induced pressure on the exterior surface is determined by Bernoulli's equation:

$$p_w = C_p \rho \frac{U_{ref}^2}{2} \quad (2.8)$$

where

- $p_w$  = wind surface pressure relative to static pressure in undisturbed flow [Pa]
- $\rho$  = air density [kg/m<sup>3</sup>]
- $U_{ref}$  = reference wind speed at local height [m/s]
- $C_p$  = wind pressure coefficient

Consequently, the resulting air infiltration over an element will depend on the wind pressure coefficient, wind speed, wind direction and air density. The three latter can be retrieved by the weather data at each time step. The wind pressure coefficient data can be given at any wing angle increment. The third-party interface used during the PhD project only employs surface-averaged  $C_p$  values for eight different wind directions in 45° increments (N, E, S, W, NE, SE, SW, NW) (Figure 2.6).  $C_p$  values can be explicitly defined in the input by the user, otherwise the software will use default values from the database provided by AIVC (1996). The user may also find  $C_p$  values on the European Standard for Ventilation in Buildings (EN 15242). Within the context of the current PhD project, all database  $C_p$  values used derive solely from the AIVC database. In addition, for the purpose of the PhD project, wind pressure coefficients were calculated through CFD simulations. For further details, the reader is referred to Paper II and Paper IV.



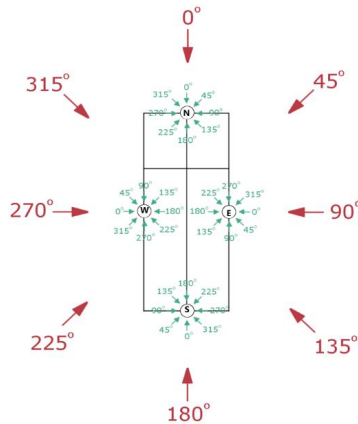


Figure 2.6. The eight wind directions in 45° increments that were used in the building energy simulations. 0° corresponds to North, 90° to East, 180° to South and 270° to West. For each façade, the surface-averaged  $C_p$  values are given for wind directions normal to the wall that is represented by the green arrows.

### 2.2.3 Monte Carlo Method

The Monte Carlo method was first introduced by Metropolis and Ulam in 1949 as a statistical approach to problems that are described by integro-differential equation, such as plenty in physical sciences (Metropolis and Ulam, 1949). The Monte Carlo method is usually used for three different types of problem solution: optimization, numerical integration, and generating draws from probability distribution (Kroese et al., 2014).

The basic principle of the Monte Carlo method lays in the random generation of input parameter values from probability distributions. The random input parameters – potentially along with deterministic values - are applied on the relevant physical equation describing the phenomenon investigated (Figure 2.7). This process involving sampling and calculation is called iteration and is repeated for an amount of times. As a result, a sample of predicted values belonging to the resulting distribution is generated (Vu et al., 2018). The number of iterations depends on the result accuracy required. Generally, the more iterations are performed, the higher the accuracy achieved. However, depending on the physical problem examined, the necessary amount of iterations needed to ensure convergence can be determined (Oberle, 2015).

In the framework of this PhD project, the Monte Carlo method was applied in order to define air infiltration through an ideal crack (Paper V). For further details regarding the probability distribution functions, the physical model, and the Monte Carlo simulations specifics, the reader is referred to Paper V.

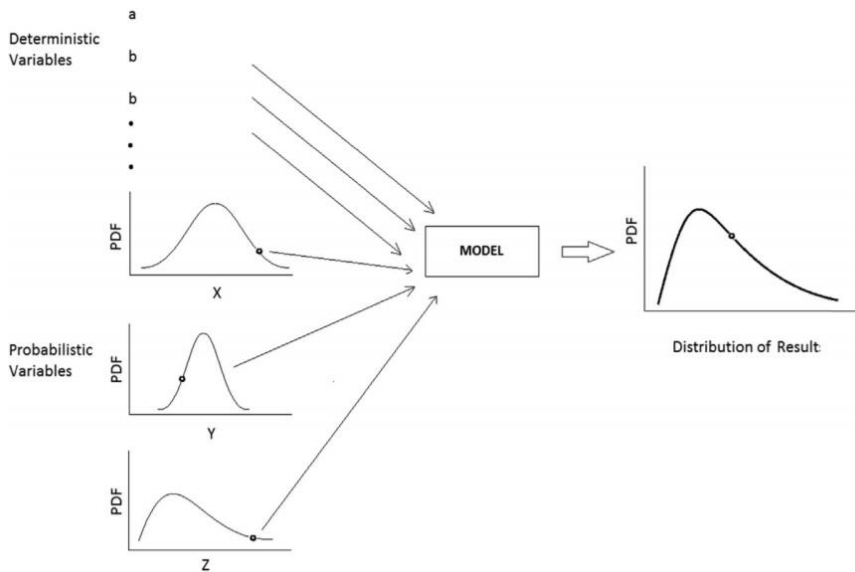


Figure 2.7. Schematic representation of the Monte Carlo method. Random values are selected from each probability distribution function and along with the constant values are applied on the physical model in order to calculate a resulting value. The process is repeated for an amount of iterations until the resulting probability distribution reaches desired accuracy. (Vu et al., 2018).

#### 2.2.4 Heat and Moisture transport

Heat, air and moisture flows across the building envelope are crucial to the building hygrothermal performance. It is known that heat, air and moisture transport across the building envelope are interrelated phenomena and they can be affected not only by each other, but also by the properties of the materials comprising the building envelope components (Bomberg, 2013; Woloszyn and Rode, 2008; Kunzel, 1995; Kunzel and Kiessl, 1996). In the context of the current PhD study, the driving mechanisms of heat and moisture transport have been studied in order to facilitate the development of a simplified calculation model and its validation, and therefore are presented

briefly below. Published findings and existing knowledge from the building physics scientific field have been combined and applied, in order to create a simplified one-dimensional simulation hygrothermal model, which allows to determine spatially the surface hygrothermal conditions along a façade with respect to microclimate (Paper I).

#### 2.2.4.1 Heat transport

Heat can be transferred across a building component, but also from the environment towards the building and vice versa. The heat transport mechanisms are: conduction, convection, radiation and latent heat flow (Figure 2.8).

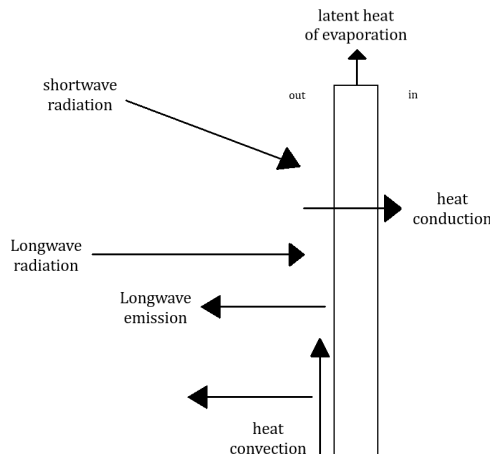


Figure 2.8. Heat transport mechanisms acting on an external building component

The heat conduction through a material can be described by Fourier's law:

$$q = k\nabla T \quad (2.9)$$

Where

$q$  = is the heat flux [ $\text{W}/\text{m}^2$ ]

$k$  = is the thermal conductivity of the material [ $\text{W}/\text{mK}$ ]

$\nabla T$  = temperature gradient across the material [ $\text{K}$ ]

The convective heat transfer can be described by Newton's law of cooling (Burmeister, 1993). The heat flux due to convection from a surface to a moving fluid is given by the following equation:

$$q = h(T_s - T_\infty) \quad (2.10)$$

Where

$h$  = is the convective heat transfer coefficient [ $W/m^2K$ ]

$T_s$  = is the surface temperature [K]

$T_\infty$  = is the temperature of the ambient air [K]

The radiation heat transfer is described by the Stefan-Boltzmann law:

$$q = \varepsilon\sigma T^4 \quad (2.11)$$

Where

$\varepsilon$  = is the emissivity of the body

$\sigma$  =  $5.67 \cdot 10^{-8} W/m^2K^4$  is the Stefan-Boltzmann constant

$T$  = is the body's temperature [K]

The shortwave solar radiation is high-energy electromagnetic radiation ranging from 0.25 to 4.0  $\mu m$  in wavelength, including the near-ultraviolet (UV), visible light and near-infrared (IR) radiation. The total solar radiation – usually referred to as global – consists of direct and diffuse radiation. As the wording implies, direct radiation describes solar radiation travelling in straight line, while diffuse radiation describes the solar radiation that has been scattered in various directions due to molecules and particles in the atmosphere. Under clear sky, the direct radiation is very high, while under atmospheric conditions, such as clouds and pollution, the diffuse radiation is much higher. Direct and diffuse radiation depend both on the geographic coordinates and the climate of a region. The solar radiation is usually measured on meteorological stations with the help of proper equipment, such as pyrhemometers, pyranometers and photoelectric sunshine recorders (Duffie and Beckman, 2013). In building energy simulations, the amount of solar radiation, including both the direct and diffusive fraction, of each location is provided by the corresponding weather file or typical meteorological year (TMY).

Longwave radiation is the energy radiating from Earth as infrared radiation at low energy. It is known that every object with temperature larger than absolute 0 (0 K) emits radiations, therefore buildings and their surroundings also emit longwave radiation. The amount of radiative heat flux emitted from the building envelope towards its surroundings can be determined by applying the Stephan-Boltzmann (Equation 2.11).

Latent heat is energy absorbed or released at constant temperature due to phase change. Unlike the other three transport mechanisms, whose driving potential is the temperature gradient, the latent heat flow is driven by the phase

change of the matter. When impinging rain water is absorbed by the building envelope, it is later evaporated, resulting in a significant heat flow across the element (Kunzel, 1995; Bittelli et al., 2008). Therefore, the latent heat flux can be taken into consideration using the following equation:

$$q = h_v \cdot g_v \quad (2.12)$$

Where

$q$  = is the latent heat flux density [ $\text{J}/\text{m}^2\text{s}$ ]

$h_v$  = is the latent heat of phase change [ $\text{J}/\text{kg}$ ]

$g_v$  = water vapour flux density [ $\text{kg}/\text{m}^2\text{s}$ ]

#### 2.2.4.2 Moisture transport

In porous materials, moisture transport is described by three transport mechanisms: vapour diffusion, surface diffusion and capillary conduction (Figure 2.9). In materials with no rigid pore structure, the transport mechanism is solution diffusion, which in the frame of building physics can also be treated as vapour diffusion (Kunzel, 1995). The driving potential of vapour diffusion is vapour pressure, while surface diffusion and capillary conduction are driven by relative humidity RH.

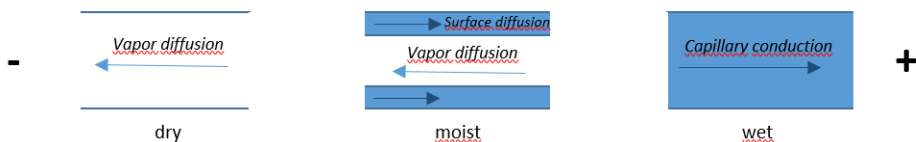


Figure 2.9. Moisture transport mechanisms in the pores of an exterior wall for different levels of moisture (redrawn from Kunzel, 1995)

Water vapour diffusion has three driving potentials: the mass fraction, the temperature and the total pressure (Bear, 1988). Within the framework of building physics, the total pressure differences are considered negligible. Similarly, diffusion caused by temperature gradient is also considered negligible (Kunzel, 1995). Therefore, the water vapour diffusion across building components is considered to be driven by the fraction mass, and can be mathematically described by Fick's law of diffusion. Although diffusion takes place in the porous of the material, it can be altered by changes on the pore path. Especially when the pores are really small, the collision between the

molecules and the pore walls are more frequent than the collisions among them, a phenomenon known as effusion. The effect of micro pores and effusion are introduced by a water vapour diffusion resistance factor that is characteristic of the material (Kunzel, 1995). The water vapour diffusion is given by the following equation:

$$g_v = -\frac{\delta}{\mu} \nabla p \quad (2.13)$$

Where

$g_v$  = is the vapour diffusion flux density [kg/m<sup>2</sup>s]

$\delta$  = is the water vapour diffusion coefficient [kg/msPa]

$\mu$  = is the water vapour resistance factor [-]

$p$  = is the water vapour partial pressure [Pa]

Surface diffusion is a liquid transport mechanism whose driving potential is relative humidity. Although vapour diffusion and liquid transport have the same driving potential, the inclusion of surface diffusion in the vapour diffusion by means of a moisture-dependent diffusion resistance value has been found to lead to substantial errors (Kunzel, 1995). Therefore, the surface diffusion is calculated along with capillary conduction.

Capillary conduction occurs on the micro-capillaries of the materials and only at water contents above the critical moisture. Although, capillary liquid transport is a convection phenomenon, it is acceptable to be treated as diffusion phenomenon for building physics applications. For that reason, and in combination with the fact that capillary conduction and surface diffusion take place simultaneously during liquid transport, both phenomena are quantified through the same diffusion equation:

$$g_w = -D_w w \nabla w \quad (2.14)$$

Where

$g_w$  = is the liquid transport flux density [kg/m<sup>2</sup>s]

$D_w$  = is the liquid transport coefficient [m<sup>2</sup>/s]

$w$  = is the moisture content [kg/m<sup>2</sup>]

The liquid transport coefficient is strongly dependent on the moisture content and is considered to give a good approximation of the capillary suction process under certain conditions, i.e. rain.

Besides the heat and moisture that is transferred across the building components, heat and moisture is also stored within each component and affect in a great degree the overall hygrothermal performance of the building.

The enthalpy of a material is given by the following equation:

$$H_s = \rho_s c_s \vartheta \quad (2.15)$$

Where

$H_s$  = is the enthalpy of the dry building material [J/m<sup>3</sup>]

$\rho_s$  = is the bulk density of the dry material [kg/m<sup>3</sup>]

$c_s$  = is the specific heat capacity of the dry material [J/kgK]

$\vartheta$  = is the temperature [k]

In reality, a building material at use is never completely dry and contains an amount of water content. Therefore, the contribution of this built-in moisture should also be taken into account by calculating the enthalpy of water  $H_w$  (Kunzel, 1995). Consequently, the heat storage of the moist material  $H_m$  is determined by the sum of the corresponding enthalpies of dry material and water as following:

$$H_m = H_s + H_w \quad (2.16)$$

Moisture in building materials can be stored in the form of vapour, water or ice. The water content is defined as the total moisture in a material. Especially for hygroscopic materials, their pores will absorb or release moisture until they reach an equilibrium with the humidity of the surrounding ambient air. The Equilibrium Moisture Content (EMC) is the moisture content at which the material is neither gaining nor losing moisture (Karagiozis et al., 2001). Each material's tendency to reach the EMC can be described by a sorption curve that shows the change of the water content present in the material versus the ambient relative humidity (Figure 2.10).

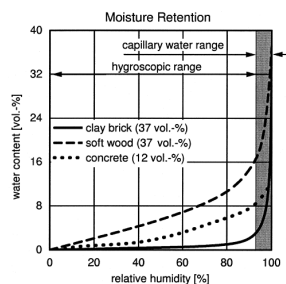


Figure 2.10. Moisture sorption curve for three building materials (Karagiozis et al., 2001)

### 2.2.4.3 Simplified one-dimensional hygrothermal model

The moisture transport part of the aforementioned model has been developed within the framework of the current PhD study, which complemented previous research work, such as the calculation of surface heat temperature and the determination of the RH on the boundary layer around the building envelope, both presented by Thiis et al. (2017). In addition, the validation of the simplified one-dimensional hygrothermal model has been part of the current PhD research work.

Heat and moisture transport are complex coupled physical phenomena, and therefore a series of assumptions were made in order to create a simplified calculation model that can be solved analytically. Particularly, in the context of the current PhD study, moisture transport was treated solely as a diffusion phenomenon (ISO 13788:2012). Crank (1975) gives a thorough guide on the mathematics of diffusion, which allow the prediction of the moisture content changes below the saturation point. The equation presented by Crank (1975) for calculating the surface moisture content  $m_0$  has been employed by the model in Paper I and is given below:

$$m_{0,j+1} = m_{0,j} + 2RD_{0,j}[m_{1,j} - m_{0,j} - \left(\frac{S}{D}\right)\Delta x(m_{0,j} - m_e)] \quad (2.17)$$

$$R = \Delta t / (\Delta x)^2 \quad (2.18)$$

Where

$D$  = moisture absorption coefficient [ $\text{m}^2/\text{s}$ ]

$S$  = surface emission coefficient [ $\text{m}/\text{s}$ ]

$m_e$  = equilibrium moisture content [ $\text{kg}/\text{m}^3$ ]

$m_{i,j}$  = moisture content at thickness increment  $i$  and time step  $j$  [ $\text{kg}/\text{m}^3$ ]

$\Delta t$  = time step [ $\text{s}$ ]

$\Delta x$  = thickness of surface material [ $\text{m}$ ]

The simplification that  $m_{1,j}$  is equal to  $m_{0,j}$  has been made, assuming that the water content of the material does not vary significantly on its exterior layer. The material thickness used for calculating the exterior surface moisture



content on the calculation model was 0.001 m, and therefore it is assumed that the moisture content difference is negligible in this thickness.

Knowing the RH on the boundary layer next to exterior building surface, allows the determination of the material's equilibrium moisture content  $m_e$  through its corresponding sorption curve.

The diffusion coefficient D is a material property that describes the material's internal resistance to moisture movement, and is strongly dependent on moisture content and temperature (Simpson and Liu, 1991; Sargent et al., 2010). Diffusion coefficients increase slightly and linearly for low moisture content levels between 10% and 50%, while change significantly during capillary uptake at higher moisture content levels over 80% (Simpson, 1993). Values of diffusion coefficients can be found on literature for some materials. For more information regarding the diffusion coefficients used within the context of the current PhD, the reader is referred to Paper I.

The surface emission coefficient S describes the material's surface resistance to moisture movement and is also dependent on moisture content and temperature, as well as air velocity (Simpson and Liu, 1991). Liu (1989) suggested an equation that allows the calculation of the surface emission coefficient S based on the diffusion coefficient D and is given below:

$$S = \frac{0.701D}{\left(\frac{\alpha}{2}\right) \left[\left(\frac{Dt}{\alpha^2}\right) - 0.196\right]} \quad (2.19)$$

Where

S = is the surface emission coefficient [m/s]

$\alpha$  = is half of the specimens thickness [m]

After selecting appropriate diffusion coefficients from relevant literature, the above equation was used to define the material's surface emission coefficient. Once all the parameters were defined, the surface moisture content was calculated through equation 2.17 (Crank, 1975).

As it has been described in section 1.2.2, wind-driven rain is a significant moisture source that can increase the surface moisture content. Therefore, the amount of absorbed water due to wind-driven rain had also to be included in the moisture transport modelling. As a result, the amount of absorbed rain

water was added to the calculated moisture content by equation (Crank, 1975). The amount of absorbed water can be given by the equation suggested by Beijer (1977).

$$G_t = \min \left\{ \begin{array}{l} R_{wdr} \\ a\sqrt{t} \end{array} \right. \quad (2.20)$$

Where

$R_{wdr}$  = the amount of wind-driven rain [mm]

$a$  = the capillary absorption coefficient equal to 0.007

$t$  = time [s]

The amount of wind-driven rain was calculated according to the international standard ISO 15927-3:2009 based on the following equation:

$$R_{wdr} = \frac{2}{9} C_R C_T O W U_{10} R_{hor}^{0.88} \cos \vartheta \quad (2.21)$$

Where

$C_R$  = roughness coefficient [-]

$C_T$  = topography coefficient [-]

$O$  = obstruction factor [-]

$W$  = wall factor [-]

$U_{10}$  = wind speed at 10m height [m/s]

$R_{hor}$  = rainfall intensity [mm/h]

$\vartheta$  = angle between wind direction and surface normal vector [°]

The amount of wind-driven rain impinging on a building surface depends significantly on the buildings surroundings and the buildings architectural façade characteristics. Sheltered parts of a building façade are expected to have significantly lower surface moisture content compared to the most exposed parts to wind-driven rain, such as higher building zones. In order to account for the spatial façade variations on the calculation of the amount of wind-driven rain, the proposed model by Tsoka and Thiis (2018) was employed. The Tsoka-Thiis ray-tracing model allows the determination of building-specific wall

factors that capture the microscale effect and account for the spatial characteristics of the façade.

For more details regarding the simplified one-dimensional hygrothermal model, the reader is referred to Paper I.

## 2.3 Measurement Techniques

For the purposes of this PhD project, various measurement techniques have been employed. The on-site measurements were used to validate results deriving from simulations or to form a more spherical overview over a specific topic.

### 2.3.1 Tracer gas

Tracer gas techniques have been established as an acceptable method for determining air changes, and has been widely used in various studies that deal with air infiltration and natural ventilation applications (Sherman, 1990; Loomans et al., 2008; Laussman and Helm, 2011; Alfonso, 2013; Hou et al., 2015). Tracer gas methods are non-destructive methods and they are designed on the basic principle of conservation of mass (air and tracer gas).

An ideal tracer gas that can be used for leak detection should fulfil some specific properties (Sherman, 1990). It should be *non-toxic* for humans, animals or the environment. It should be *inert*, viz. not to react chemically or physically with the rest parts of the system under investigation. It should be *unique* in order not be confused with other components of the ambient air. It should be *easily detectable* and if possible not present or in the smallest possible concentration in the ambient air. It should be *quantifiable* through existing equipment. Last but not least, an ideal gas should not affect the air flow or the air density of the system under investigation. Table 2.1 presents common tracer gases used to determine air changes along with their main properties, as given by the relevant International Standard (ASTM E741, 2006).

Table 2.1. Tracer gases and safety Issues (ASTM E741, 2006)

Tracer Gas	PEL	Toxicology	Chemical Reactivity	Comments
Hydrogen	Asphyxiant	Non-toxic	Highly reactive in presence of heat, flame, or O <sub>2</sub>	Fire and explosion hazard when exposed to heat, flame, or O <sub>2</sub>
Helium	Asphyxiant	Non-toxic	Inert	
Carbon Monoxide	50 ppm	Combines with hemoglobin to cause anoxia	Highly reactive with O <sub>2</sub>	Fire and explosion hazard when exposed to heat or flame
Carbon Dioxide	5000 ppm	Can be eye irritant	Reacts vigorously with some metals; soluble in water	
Perfluorocarbon tracers (PFTs)	Asphyxiant	Non-toxic	Inert	Thermal decomposition may produce toxic compounds
Nitrous Oxide	25 ppm	Moderately toxic by inhalation	Violent reaction with aluminum; water soluble	Can form explosive mixture with air; ignites at high temperature
Ethane	Asphyxiant	Non-toxic	Flammable	Incompatible with chlorine and oxidizing materials
Methane	Asphyxiant	Non-toxic	Flammable	Incompatible with halogens and oxidizing materials
Octafluorocyclobutane (Halocarbon C-318)	1000 ppm	Low toxicity	Nonflammable	Thermal decomposition yields highly toxic compounds
Bromotrifluoromethane (Halocarbon 13B1)	500 ppm	Moderately toxic by inhalation	Incompatible with aluminum	Dangerous in a fire
Dichlorodifluoromethane (Halocarbon 12)	1000 ppm	Central nervous system and eye irritant; can be narcotic at high levels	Nonflammable; can react violently with aluminum	Thermal decomposition yields highly toxic fumes
Dichlorotetrafluoromethane (Halocarbon 116)	1000 ppm	Can be asphyxiant, mildly irritating, narcotic at high levels	Can react violently with aluminum	Thermal decomposition yields highly toxic fumes

Carbon dioxide (CO<sub>2</sub>) is a tracer gas that has high permissible exposure limit (PEL), it is easily obtainable and affordable, and it can be easily quantified. Furthermore, the relevant measuring equipment comes at relatively low cost and rather high accuracy (Roulet and Foradini, 2002). Therefore, CO<sub>2</sub> is a popular choice as tracer gas and has been used in several studies that investigate air infiltration and natural ventilation (Mahyuddin and Awbi, 2012; van Hoof and Blocken, 2013; Kraniotis et al., 2014; Cui et al., 2015; ). CO<sub>2</sub> was selected as tracer gas for the purpose of this PhD project as well.

The ‘concentration test decay method’ was employed for measuring the average air infiltration rate of the reference building (ASTM-E741, 2006). According to the standard’s guidelines, tracer gas was inserted into the room from a gas tank and a fan was used to ensure sufficient mixing conditions into the room. The tracer gas concentration was measured at regular time intervals using two CO<sub>2</sub> loggers. The two CO<sub>2</sub> sensors were placed in two representative positions within the room in order to ensure the concentration uniformity. The CO<sub>2</sub> sensors used for the purposes of the PhD study offer an accuracy of  $\pm 30\text{ppm} \pm 5\%$  of measured value in the range of 0-5000 ppm, which fulfils the requirement of the ASTM-E741 standard regarding maximum acceptable error. The CO<sub>2</sub> sensors have an automatic calibration function. An ‘Outside Air Calibration’ at 400 ppm was performed according to the manufacturer’s guidelines (CP11 – short instruction manual 2014). Since CO<sub>2</sub> already exists in the ambient air, before each measurement the outdoor level (background) of CO<sub>2</sub> was also determined. The normalized concentration  $C_N$  was determined based on the following equation:

$$C_N(t) = \frac{C(t) - C_o}{C(0) - C_o} \quad (2.22)$$

Where

$C(t)$  = the CO<sub>2</sub> concentration measured at each time interval [ppm]

$C(0)$  = the CO<sub>2</sub> concentration measured at  $t = 0$ s [ppm]

$C_o$  = the outdoors (background) CO<sub>2</sub> concentration [ppm]

The 'optional regression method' was applied in order to determine the average air infiltration rates (ASTM-E741, 2006) according to the following equation:

$$\ln C_N(t) = -At + \ln C_N(0) \quad (2.23)$$

Plotting  $\ln C_N(t)$  against  $t$ , the mean infiltration rate ACH can be determined as the slope  $A$  of the graph (Figure 2.11). The measurement error was defined according to the standard (ASTM-E741, 2006) and the maximum error on air changes per hour was defined at  $\pm 0.0046$  ac/h.

For more details regarding the tracer gas method followed and the statistical analysis of the measurement data, the reader is referred to Paper IV.

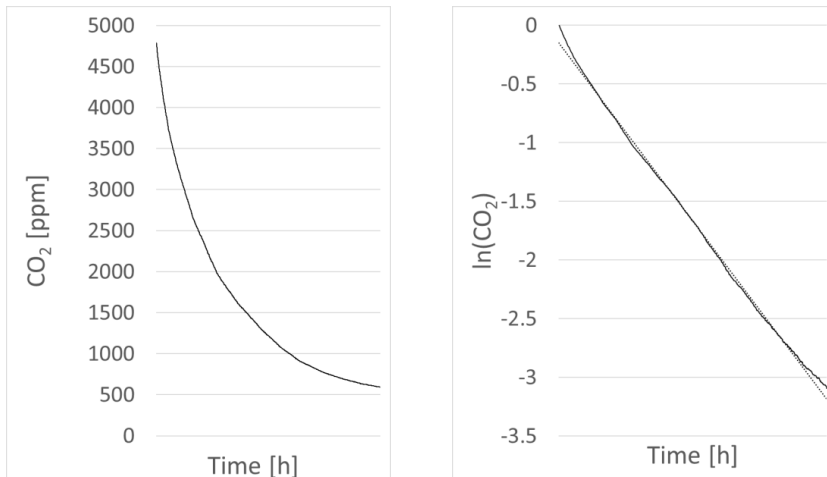


Figure 2.11. Example of tracer gas concentration vs. time elapsed; (a) untransformed; (b) after logarithmic regression.

### 2.3.2 Pressure measurements

Full-scale pressure measurements consist an invaluable data source for wind-induced loads in buildings, and along with reduced-scale pressure measurements (wind-tunnel testing), they are considered the most accurate methods for determining wind pressure coefficients (Costola et al., 2009). Full-scale measurements present the advantage that it is not necessary to reproduce boundary conditions, adopt physical models or perform downscaling. On the other hand, it is not possible to control the wind conditions, such as speed, direction and turbulence intensity.

Full-scale installations for wind-induced pressure measurements usually employ an apparatus of pressure taps with PVC or silicon tubing in combination with pressure transducers and a data acquisition system (Levitan et al., 1991; Cochran and Cermak, 1992; Richards et al., 2001; Yoshida et al., 1992). The pressure taps are positioned on the external surface under investigation and usually have a typical internal diameter (3mm-10mm). The tapping points are connected through tubes of similar internal diameter to the pressure transducers. The pressure signal is transmitted pneumatically through the tube to the pressure transducers, and consequently the transducers convert the air pressure into electrical signal, which is stored to an appropriate data acquisition system.

There are three types of pressure measurements (Figure 2.12):

- Gauge pressure: the pressure relative to the atmospheric pressure
- Absolute pressure: the pressure relative to a high vacuum reference
- Differential pressure: the difference between two points

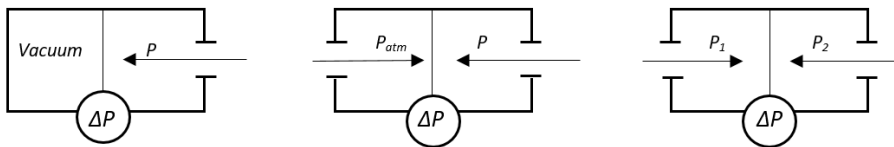


Figure 2.12. Principle of (a) an absolute pressure sensor; (b) a gauge pressure sensor; (c) a differential pressure sensor.

For the current PhD project, a series of differential pressure measurements were performed in order to investigate the spatial wind-induced pressure

variations over the building envelope. More specifically, full-scale pressure measurements were performed to acquire spatially the pressure differences between windward and leeward façades (Paper III), as well as to determine spatial wind pressure coefficients over the windward façade of a mid-rise building (Paper V).

Twelve SDP1000 low-range differential pressure sensors for air were used during the on-site measurements. The specific sensors have a measurement range of -5 Pa to 125 Pa, and they include a digital built-in temperature compensation circuit that renders the measurements temperature independent.

Pressure taps with an internal diameter of 3mm were placed on specific measuring positions along the building façades investigated, and they were connected through silicon tubes of an internal diameter 3mm to the pressure transducers. The lengths of the tubes varied from 5m to 25m. The 'noise' due to the length of the silicon tubing was filtered out by the means of moving average (Smith, 1997). The differential pressure sensors were connected to the data acquisition system 'LabView', which was recording the instantaneous pressure difference values with a frequency of 5 Hz (Figure 2.13).

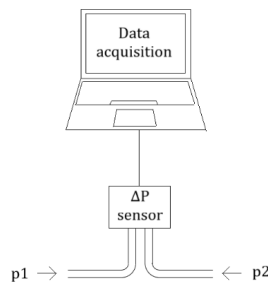


Figure 2.13. Schematic display of the differential pressure measurement apparatus principle.

For the purpose of Paper III, the two pressure taps belonging to the differential pressure sensor were placed on the windward and leeward facades of the twin buildings, thus providing the pressure difference between wind and leeward façade during the measuring period. During the measuring period corresponding to Paper III, the dominant wind direction was South (180°). For the purpose of Paper V, the pressure taps were placed on the windward façade and the rooftop of the twin buildings. As a result, it was possible to calculate wind pressure coefficients on the windward façade of the buildings using the measured pressure difference between the impinging wind pressure on the

windward façade and the reference wind pressure on the free stream over the rooftop. During the measuring period corresponding to Paper V, the dominant wind direction was North (0°), and therefore only wind pressure coefficients on the windward North façade were possible to be acquired.

For more detailed description of the methodology followed in each study, the reader is referred to Paper III and Paper V.

### 2.3.3 Thermography techniques

Infrared thermography (IRT) is a non-invasive imaging technique that allows the visualizing of the infrared energy emitted by objects. IRT has been extensively used for building diagnostics, as it easily allows the detection of irregularities, such as air leakages, thermal bridges and moisture damages (Kirimtat and Krejcar, 2018; Balaras and Argiriou, 2002; Bagavathiappan et al., 2013). Furthermore, it allows the spatial inspection of surface temperatures and thermal transmittance (U-value) on large façade areas (Datcu et al., 2005; Nardi et al., 2016; Nardi et al., 2014).

Thermography measuring techniques employ infrared (IR) cameras, which can measure the emitted radiation from object surfaces and convert this radiation into thermal images (Figure 2.14). The thermography measurement methods are separated into two categories: qualitative and quantitative. Qualitative measurements are used to detect visually wide variations in the thermal properties of the components under investigation, while the quantitative method can evaluate the condition of a component by quantifying properties, such as the U-value (Kirimtat and Krejcar, 2018).

Thermography measuring techniques are based on the Stefan-Boltzmann law, which states that the total emissive power of a blackbody is proportional to the fourth power of its absolute temperature as following:

$$W_b = \sigma T^4 \quad (2.24)$$

Where

$W_b$  = is the blackbody radiant emittance [ $W/m^2$ ]

$\sigma$  =  $5.67 \cdot 10^{-8} W/m^2K^4$  is the Stefan-Boltzmann constant

$T$  = is the body's temperature [K]

However, real objects might approach the blackbody behaviour in certain spectral intervals, but generally, they do not comply with the above law over an



extended wavelength region. Therefore, the factor emissivity is introduced and describes the ratio of the spectral radiant power from an object,  $W_{\lambda o}$ , to that from a blackbody,  $W_{\lambda b}$ , at the same temperature and wavelength. Mathematically, the spectral emissivity is given by the following formula:

$$\varepsilon_{\lambda} = \frac{W_{\lambda o}}{W_{\lambda b}} \quad (2.25)$$

Three types of radiation sources are distinguished based on the way the spectral emittance of each varies with wavelength:

- A blackbody for which  $\varepsilon_{\lambda} = \varepsilon = 1$
- A graybody for which  $\varepsilon_{\lambda} = \varepsilon = \text{constant less than } 1$
- A selective radiator for which  $\varepsilon$  varies with wavelength

Infrared cameras used the Stefan-Boltzmann formula adjusted for a graybody radiator as shown below:

$$W = \varepsilon \sigma T^4 \quad (2.26)$$

Where

$\varepsilon$  = is the emissivity of the body [-]

$\sigma$  =  $5.67 \cdot 10^{-8} \text{ W/m}^2\text{K}^4$  is the Stefan-Boltzmann constant

$T$  = is the body's temperature [K]

Emissivity is a significant material property that is crucial to the correct data retrieved through thermographic techniques. For some materials, emissivity values under various conditions may be available on literature. However, the emissivity of any material can be determined through experimental techniques (Avdelidis and Moropoulou, 2003). The International standard ASTM E1933 (1997) dictates that the emissivity of material can be measured in laboratory after exposure in a climate chamber and convection oven. An empirical procedure suggests the determination of material emissivity during exposure at a defined temperature and using as a reference a piece of electrical tape with known emissivity (Avdelidis and Moropoulou, 2003; Charisi et al., 2016).

However, when an IR camera views an object, it receives radiation not only from the object itself, but also reflected radiation from the surroundings via the object. Furthermore, this total amount of radiation will be attenuated during its path from object to camera through the atmosphere (Figure 2.14).

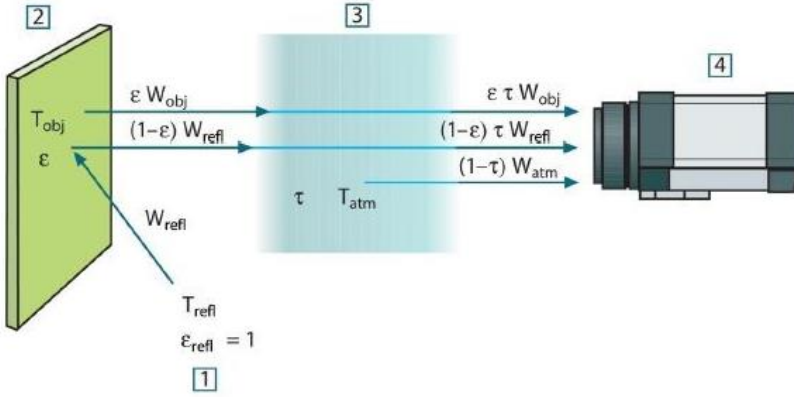


Figure 2.14. Schematic representation of the thermography measuring technique principle; (1) surroundings; (2) object; (3) atmosphere; (4) camera. (Flir Tools: User's manual. Used with permission)

Therefore, the total radiation power received by the camera is given by the following equation:

$$\begin{aligned}
 W_{tot} &= \varepsilon \tau W_{obj} + (1 - \tau) W_{refl} + (1 - \tau) W_{atm} \\
 &= \varepsilon \tau \sigma T_{obj} + (1 - \varepsilon) \tau \sigma T_{refl} + (1 - \tau) \sigma T_{atm}
 \end{aligned} \quad (2.27)$$

Where

$\varepsilon$  = is the emittance of the object [-]

$\tau$  = is the transmittance of the temperature [-]

$T_{atm}$  = is the temperature of the atmosphere [K]

$T_{refl}$  = is the reflected ambient temperature [K]

The IR camera operator usually has to supply all the four above mentioned values, as well as the distance between object and camera and the relative humidity level during the measurement. The reflected temperature  $T_{refl}$  can be determined through an empirical approach called the 'reflector method' (Charisi et al., 2016). However, assumptions regarding the transmittance, reflected temperature and ambient temperature, can be acceptable in cases where the object surface temperatures are quite high (Flir Tools, 2011).

In the current PhD project, thermography techniques were employed in order to define the spatial surface temperatures along two building façades (Paper I). According to the manufacturer, the IR camera used for the purpose of this PhD study has an accuracy of  $\pm 2^\circ\text{C}$  or 2% of the reading. This error accounts for errors that can derive from a variety of factors during measurement, such as

emissivity, reflected ambient temperature, transmittance, atmospheric temperature and camera response.

For further information regarding the measuring equipment and the methodology followed, the reader is referred to Paper I.

#### 2.3.4 Resistance moisture meters

The potential of using the electrical resistance of wood as a measure of its moisture content has been explored since the beginning of the 20<sup>th</sup> century (Stamm, 1927). Wood, as a hygroscopic material, has the tendency to absorb or release water until it reached equilibrium (EMC) with the atmospheric conditions. However, water has much higher conductivity than wood, thus its presence inside wood will increase wood's conductivity and consequently decrease its electrical resistance (Stamm, 1927; Dietsch, 2015). For example, the wood resistance at a moisture content of 8% is approximately 1000 times larger than at a moisture content of 19% (Hartley and Marchant, 1995). At moisture levels lower than the fiber saturation of wood, a linear relationship exists between the logarithm of conductance and the logarithm of moisture content, and therefore the resistance method gives good accuracy (James, 1988; Dietsch, 2015, Hartley and Marchant, 1995). However, at levels above the fiber saturation point, the correlation between conductance and moisture content is weaker and less accurate results are produced (James, 1988), while for moisture content lower than 6% the wood resistance is too large to be measured (Hartley and Marchant, 1995).

One of the most commonly used resistance-type meter for building applications is the two-pin electrode (Figure 2.15). In that case, two electrodes, with a defined distance of usually 30mm between them, are inserted into the timber specimen investigated. The measurement system applies a current to the electrodes and measures the loss of voltage due to moisture (Dietsch, 2015).

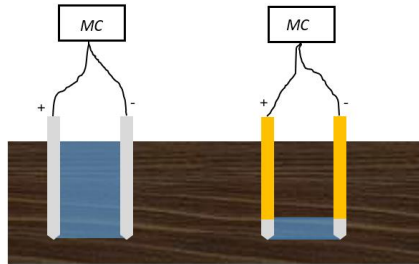


Figure 2.15. Schematic of areas measured by resistance method using insulated and non-insulated electrodes (redrawn from Dietsch, 2015)

The relationship between resistance and moisture content depends on various parameters, such as the wood species, the temperature, and the grain direction (Hartley and Marchant, 1995). The International Standard EN 13183-2 (2002) provides guidelines for correct estimation of the wood moisture content by electrical resistance method. Wood electric resistance sensors are widely used for building applications and experience has shown that they deliver acceptable accuracy (Dietsch, 2015). Field measurements have also shown that they present good reliability and performance even in exterior environments, thus rendering them suitable even for building envelope monitor applications (Ueno and Straube, 2008).

In the context of the current PhD project, wood resistance humidity sensors were used for the validation of simulated values (Paper I). According to the manufacturer, the humidity sensors used give results with a measuring accuracy lower than 3% of RH within the range 20%-80% of RH.

### 3. Results and Discussion

The most important findings of the current PhD study are presented on the following section. The results are aligned with the research objectives presented in Chapter 1, thus presenting the answers to the scientific questions set on the beginning of the research.

#### 3.1 Micro scale effect on climatic loads

As it has been discussed in Section 1.2, the climatic loads acting on buildings can be determined through on-site measurements, as well as numerical simulations or empirical models. For the purpose of the current PhD project, established methods and standards were employed in order to define the climatic loads acting on the various reference buildings examined with respect to the microclimate.

Both CFD simulations and on-site measurements were performed in order to define the air flows around buildings, and consequently the wind-induced pressure variations on the buildings' façade (Paper II, Paper III, Paper IV, Paper V), as it has been described in Section 2.2.1. The microclimate effect on the wind loads on buildings is presented in detail on Sections 3.3 and 3.4.

The simulation tool DIVA-for-Rhino was used in order to generate climate-specific annual surface irradiation in Paper I. The tool employs the ray-tracing technique in order to calculate annual irradiation at building node locations defined by user, and by taking into consideration the building's surrounding and architectural characteristics (Robinson and Stone, 2004). As a result, a mesh for the surface of interest can be produced, and it describes the amount of incident radiation on each mesh node. Figure 3.1 shows the annual irradiation over a node grid generated for the timber façade of the local high school. The mesh consists of thousands of nodes and the tool is able to capture the shadowing effect created by the neighbouring building, as well as the sheltering effect caused by the existing windowsills on the façade.

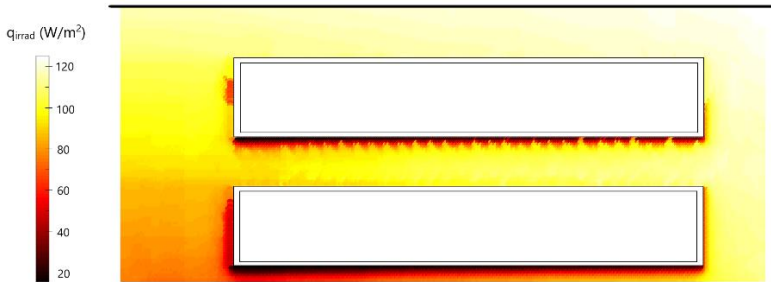


Figure 3.1. Mean annual solar radiation impinging on the façade of the local high-school building.

The amount of wind driven rain impinging on a building vertical surface can be defined, among else, through the international standard ISO 15927-3 (2009). In Paper I, a method that combines the use of ray tracing with the ISO for WDR was employed (Tsoka and Thiis, 2018). Building-specific wall factors for the calculation of the impinging wind-driven rain were determined according to the above method. Figure 3.2 shows that the building-specific wall factors are able to capture the sheltering effect provided by the windowsills on the local high school’s façade.

In the context of the current PhD study, contemporary numerical methods, as well as analytical models, were applied in order to introduce the microclimatic effect on the determination of climatic loads acting on buildings. Furthermore, it was possible to define the microclimatic loads spatially along the façades, thus accounting for details such as architectural characteristics of the building shell.

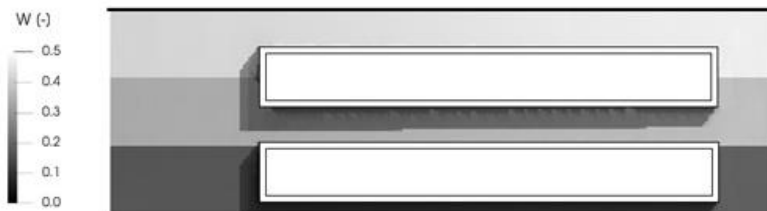


Figure 3.2. Building-specific wall factor for the local high-school’s timber façade (Paper I).

### 3.2 Microclimatic surface hygrothermal conditions

Employing the basics of heat and moisture transport, as described in section 2.2.4, a simplified one-dimensional hygrothermal model that can predict the

surface temperature and moisture content of the façade material was presented (Paper I). The main equations of the suggested model are presented in detail in Paper I. The equation model was applied to two different building façades: the timber façade of the local high school and the masonry façade of the NMBU storage building (Figure 2.3). Among else, the model used as input climate data taken from the local weather station and spatial grids along the façade for solar radiation and wind driven rain. The incident solar radiation and impinging wind-driven rain for each grid node were calculated as described in Section 3.1, by employing the simulation tool DIVA-for-Rhino and applying the suggested methodology for building-specific wall factors by Tsoka and Thiis (2018). The model was applied at each one of the grid nodes of the façade investigated, thus capturing the spatial microclimatic effect along the whole façade. The time interval of the simulation model was defined at 1 hour, similarly to the format of a typical weather year (TMY) climate file.

On-site measurements of surface temperature using thermography techniques were performed on both buildings. The measurements were used to validate the accuracy of the developed model in predicting surface temperatures. The recording interval of the IR camera was set at 15 minutes. The hourly-averaged measured surface temperature was calculated and compared with the corresponding simulated surface temperature. The spatial root mean square error (RMSE) for both building façades was lower than 5%, with the exception of areas close to the metal door and metal windowsills, where the error increased significantly (Figure 3.3). The reflected radiation from the metal elements of the buildings, which are not part of the model computational mesh, are not included on the simulations, and therefore their effect cannot be quantified, and in addition with the thermal bridge formed between the wall and the opening, can potentially lead to this larger error.

Resistance moisture meters were installed on the timber cladding of the wooden façade. The measuring interval of the moisture sensors was 30 minutes. The hourly-averaged measured surface moisture content values were compared with the calculated surface moisture content values through the developed model. The RMSE was defined at 0.05 (5 M.%). Due to lack of measurements on the masonry building, the model's results were compared to the surface moisture contents calculated through the well-established software WUFI (Karagiozis et al., 2001). Specifically, the one-dimensional WUFI Pro 4

tool was used. The comparison showed that the developed model's results deviate only by 0.0067 (0.67 M.%) of RMSE from the advanced software WUFI.

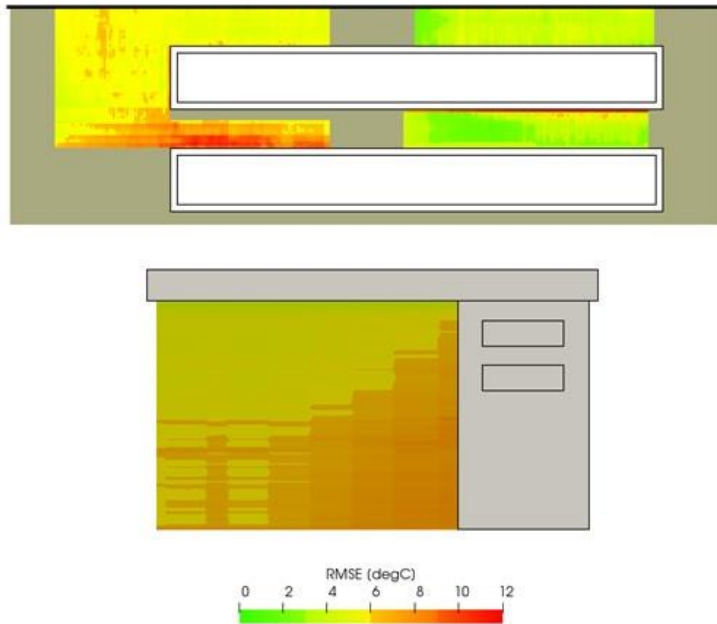


Figure 3.3 RMSE of the simulated surface temperature compared to the IR measurements for (a) wood façade and (b) masonry façade (Paper I).

The determination of the microclimatic loads of solar radiation and wind-driven rain using ray tracing technique captures not only the microclimatic effect caused by the building's surroundings, such as neighbouring buildings and vegetation, but also the impact of architectural details on the façade, such as the sheltering effect of window sills. Figure 3.4 shows the simulated surface hygrothermal conditions on the wooden façade of the school building. The sheltering effect of the window extrusions from sunlight and rain, is captured both on the calculation of surface temperature and moisture content. Furthermore, the lower surface temperatures at the low left part of the façade are the result of the shadow provided by the neighbouring building.

Summarizing, the developed model gives the possibility to define spatially along a whole façade the surface hygrothermal conditions by taking into consideration the building's surroundings and its unique architectural characteristics. In contrast to conventional hygrothermal models that treat the



whole façade uniformly, the developed model can reveal spatial variations and patterns. Combined with appropriate discoloration or mould-growth models, it can reveal interesting discoloration patterns and high-risk areas for biological activity. Therefore, it can facilitate the decision-making process during the design phase and help engineers and architects pick sustainable materials with high durability.

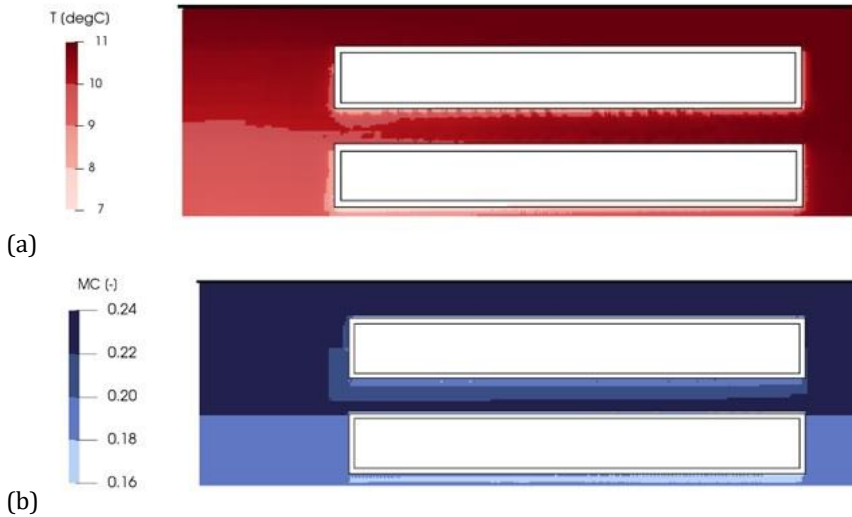


Figure 3.4 Spatial simulation of (a) yearly mean surface temperature and (b) yearly mean moisture content on the wooden façade of the local school building (Paper I).

However, as it has been described in Section 2.2.4, the presented model attempts a simplified approach to the complex coupled phenomena of heat and moisture transport, allowing for a number of assumptions and simplifications.

More specifically, the model does not consider latent heat of phase change, longwave radiation and thermal bridging effect. As far as the heat transport modelling is concerned, it only takes into consideration temperature differences and shortwave solar radiation in order to calculate the heat fluxes across the building envelope. The longwave radiation is introduced in the calculation only through the convective heat transfer coefficient, which has been appropriately increased in order to account for the radiative heat transfer coefficient too. The radiative night-time cooling due to longwave emission is also neglected due to lack of information regarding cloud coverage and ground

temperatures. However, the omission of radiative night-time cooling has been done on the basis that radiative cooling affects mostly horizontal surfaces, such as roofs, and surfaces in building envelopes with low thermal inertia (Kehrer and Schmidt, 2008). The cases tested are vertical surfaces in highly insulated building envelopes.

The thermal bridging effect is a dynamic multi-dimensional heat transfer phenomenon that cannot be approximated by a simplified one-dimensional model. The simplification that thermal bridging effect is neglected in the current model has been made on the basis that the model is designed for well-insulated building envelopes where the thermal bridges are usually minimised. Also, thermal bridges affect mostly the internal building surfaces by causing condensation and mould growth (ISO 13788:2001), while the presented model focuses only on the exterior building surface.

Nevertheless, all the aforementioned omissions, simplifications and assumptions consist considerable limitations and contribute to the model's numerical errors. Despite its limitations, the results for the test cases examined indicate that the presented model can reproduce the spatial variations of the microclimatic surface conditions along the building envelope in a simple and cost-effective way.

### 3.3 Wind-induced pressure variations

CFD simulations were performed, as described in Section 2.2.1, for the reference buildings of two different experimental sites: the main building of the meteorological station and the twin medium-rise building complex (Figure 2.4 & 2.5). The terrain and the surroundings of the buildings of interest were also included on the three-dimensional models used for the CFD simulations. As a result, the microclimate impact on the wind-induced pressures along the building façades could be quantified (Paper II, Paper III and Paper IV).

Figure 3.5 shows the impact of the surroundings' morphology on the wind-induced pressure variations for the main building of the meteorological station. During the first CFD simulations that the building is fully exposed, the simulated North-East wind (45°) exerts high pressure on the North (and East) façades of the reference building. Furthermore, the CFD results reveal the pressure variations along the buildings façades according to the impinging wind

direction. For example, for North-East wind, high pressures are developed on the North-East corner of the reference building and gradually are decreasing moving West along the North façade, while negative pressures are developed on the eaves of the building roof (Figure 3.5).

The second microclimatic case was created by an obstacle, with similar height as the reference building, that is placed at approximately 5 meters from the North-East corner of the building. The CFD results show that the obstacle provides essential shelter to the reference building from the impinging North-East wind, as the wind-induced pressures on the North (and East) façade decrease significantly.

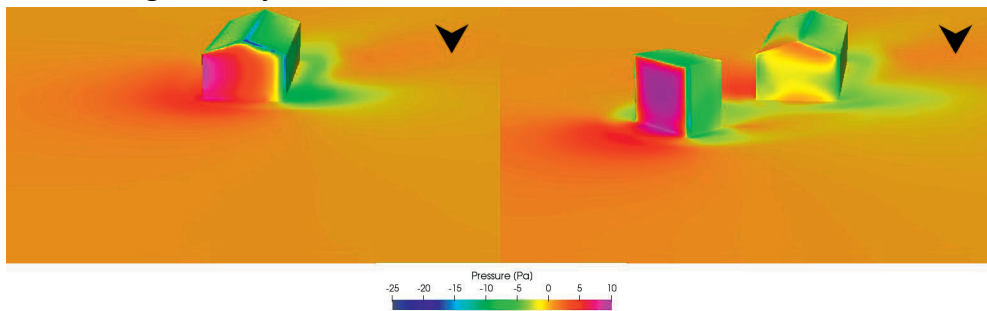


Figure 3.5 Wind-induced pressure variations calculated through CFD simulations for the main building of the meteorological station and for two different microclimatic cases: (a) exposed and (b) partially sheltered.

Similarly, Figure 3.6 shows the pressure variations along the façades of the twin medium-rise buildings with respect to the local micro scale climate. The three-dimensional model used for the CFD simulations included all the neighbouring buildings of the complex in a radius of approximately 100 meters, as well as the terrain altitude variations within the same radius. As a result, the impact of the local terrain and surroundings is taken into account during the determination of the wind flow around the reference buildings, and consequently it can be reflected on the wind-induced pressure variations along the building façades. The CFD results reveal also the significant wind shelter one building is providing to each twin, as well as the wind sheltering effect from neighbouring obstructions and buildings. As it can be seen from Figure 3.7, for North wind direction ( $0^\circ$ ), the windward side of one the buildings develops high pressures, while the windward side of its twin is completely sheltered from the impinging wind and maintains low pressure.

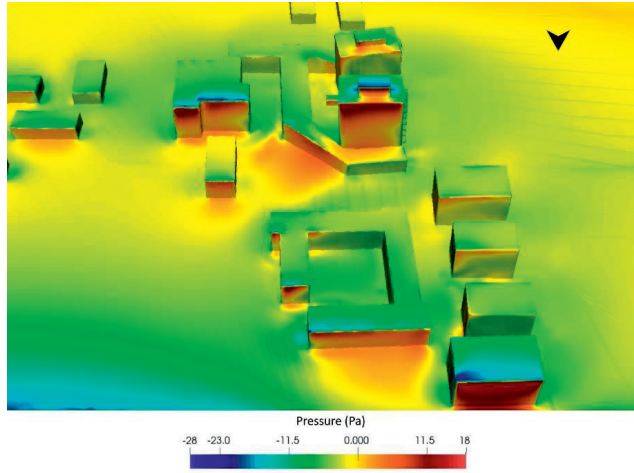


Figure 3.6 Wind-induced pressure variations calculated through CFD simulations for the twin medium-rise complex.

Differential pressure measurements, as described in Section 2.3.2, were performed also on the twin medium-rise building complex (Figure 2.5). The pressure difference between the windward and leeward side of each of the twin buildings was measured simultaneously at several points. The pressure taps were placed symmetrically on the windward and leeward façades of each of the building (Figure 3.7).

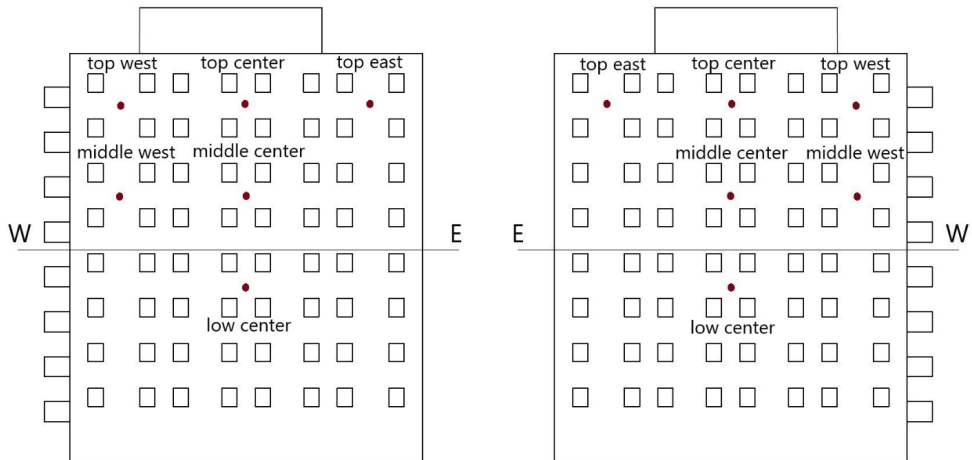


Figure 3.7 Positions of the pressure taps, represented by red dots, on the South and North façade of the twin buildings (Paper III).

During the measuring period, the dominant wind direction was South ( $180^\circ$ ) (Figure 3.8.a). Therefore, it was expected that the windward (South) façades of the twin buildings would develop high wind-induced pressures, while their leeward (North) façades would remain at similarly low levels. Subsequently, the measured pressure difference between windward and leeward façade at each building, would give an indication for the difference in the wind-induced pressures between the two windward façades of the two buildings.

Figure 3.8.b presents the measured differential pressures between windward and leeward façades on the various measuring positions on the two buildings. The results show that the center top part of the exposed South building develops high differential pressures throughout the measurements that rise up to 15 Pa. High differential pressures between the leeward and windward façade, imply high wind-induced pressures on the windward façade. Moving down along the vertical axis of the windward façade of the South building, the differential pressures tend to drop significantly around 0, suggesting substantial decrease on the wind-induced pressures along the vertical axis of the windward façade. The negative differential pressure on the 'low center' measuring position is potentially the effect of the neighbouring parapet that surrounds the twin buildings (Figure 3.6), thus signifying the impact the surroundings can have on the wind-induced pressure variations along building façades. Similarly, the two top measuring positions on the East and West side of the exposed South building present high pressure difference fluctuating between 5 to 10 Pa, meaning that high wind-induced pressures are developed on the top of the windward façade. The 'Middle West' measuring position presents significantly lower differential pressure around 0-1 Pa, suggesting that lower wind-induced pressure is exerted on it.

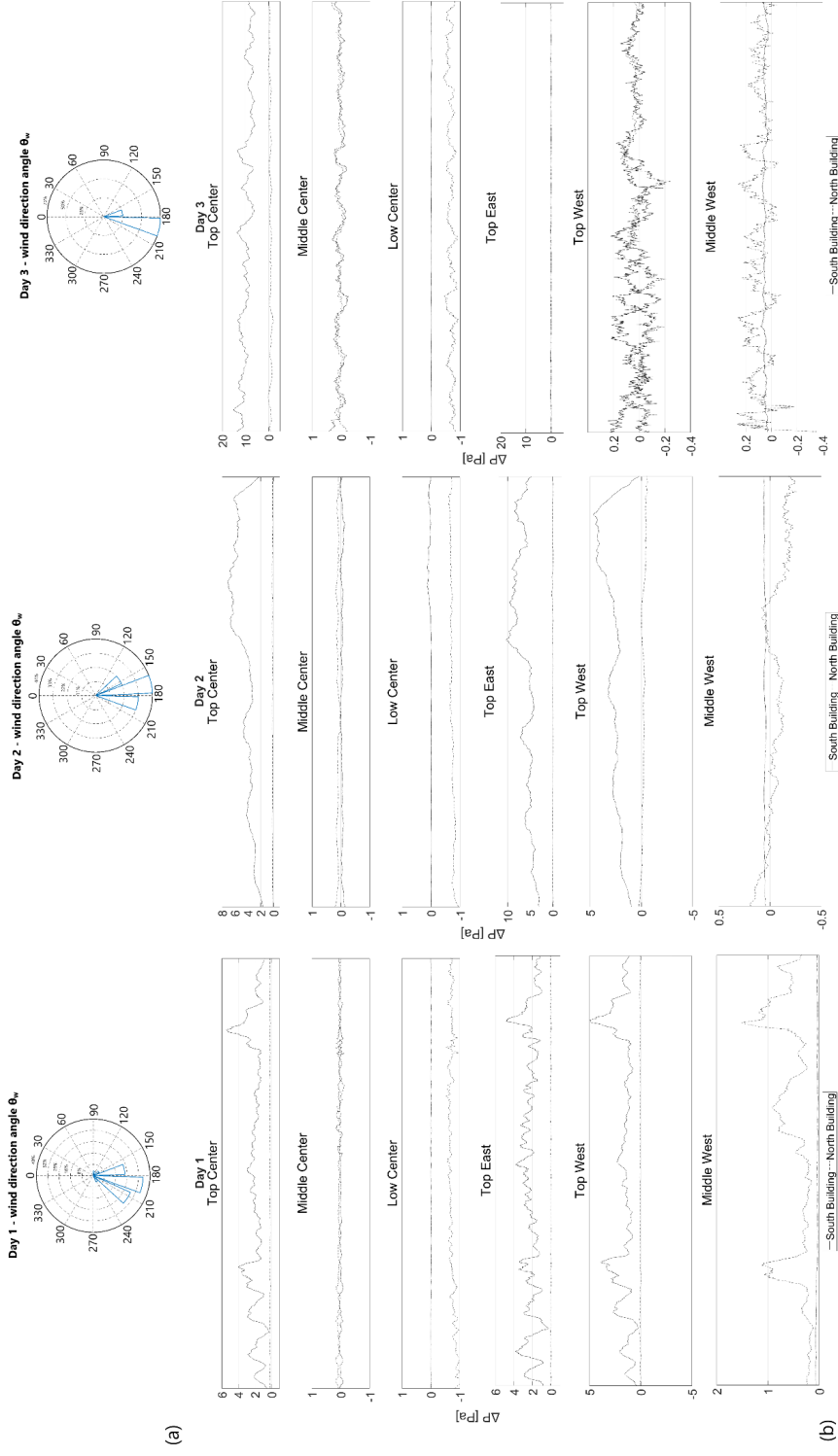


Figure 3.8. (a) Wind roses depicting the variation of the direction angle  $\theta_w$  during each measurement 'day' ( $\theta_w = 0^\circ$  corresponds to North wind,  $\theta_w = 90^\circ$  to East,  $\theta_w = 180^\circ$  to South and  $\theta_w = 270^\circ$  to West); (b) Measured pressure differences on the six positions of the two twin buildings along the whole measuring period of approximately 6 days.

It is worth noticing that the central positions develop higher pressures compared to the edges. Especially during 'Day 3', that the wind direction remained South during the whole measuring period, the measured pressure difference on the 'top center' position is slightly fluctuating around 10 Pa. The corresponding measured pressure differences on the 'top east' and 'top west' positions fluctuate around 0.

Furthermore, the results show that in all measuring positions on the sheltered North building and during every measurement 'Day', the measured pressure differences fluctuate around 0. This fact indicates that negligible wind-induced pressures are developed on the windward façade of the North Building, which is entirely sheltered by its twin South building, highlighting once again the impact of the microclimate formed by the twin buildings on the wind-induced pressurization of the buildings.

The on-site measurements indicate a significant spatial variation of the wind-induced pressures along the façade of a medium-scale building. Furthermore, the on-site measurements reveal the essential sheltering effect one building is providing to its twin, as well as the effect of the surroundings.

Both on-site measurements and CFD simulations highlight that the microclimate can have essential impact on the spatial variation of the wind-induced pressures along building façades for both small- and medium- scale buildings. Various building aspects depend on wind, such as wind-induced air infiltrations. As a result, the determination of the wind-induced pressure variations along the building façades with spatial accuracy can account for the microclimatic effect, and can be used as appropriate microclimatic boundary conditions in order to improve the calculation methods and increase the prediction accuracy.

### 3.4 Building-specific wind pressure coefficients

The effect of microclimate on the wind-induced pressure variations along building façades was established and potential methods to incorporate it on the building performance simulation were investigated (Paper II, Paper IV and Paper V). Wind pressure coefficients ( $C_p$ ) represent the wind-induced pressure over a body relative to the freestream pressure, and can be included on the building energy simulation for the calculation of the wind-induced air infiltration, as described in Section 2.2.2. Especially for old and leaky buildings,

where the wind-induced pressurization of the building envelope is catalytic for their air infiltration rate, the use of wind pressure coefficients can help significantly to improve the air infiltration calculation.

In order to capture the microclimatic conditions of any building investigated, building-specific wind pressure coefficients should be determined based on the building's actual surroundings and geometry. Once the building pressure variations are determined through CFD simulations or pressure measurements, the wind pressure coefficients can be calculated through Equation 2.8 (Section 2.2.2).

For the purpose of the current PhD study, building-specific wind pressure coefficients were calculated for two reference buildings: the main building of the meteorological station and the twin medium-rise building complex. The building-specific  $C_p$  values for the building meteorological station were calculated through CFD simulations (Paper II and Paper IV). The on-site measurements on the twin buildings were used to determine building-specific  $C_p$  values spatially along the windward façades of the twin buildings (Paper V). The spatial distribution of the wind pressure coefficient on the façades of the reference building at the meteorological field for wind normal to the surfaces is presented on Figure 3.9. The  $C_p$  values correspond to the exposed microclimatic case (Figure 3.5). It is reminded that the reference building's long axis runs North-South with a deviation angle of  $6.5^\circ$  (Figure 2.4). The CFD simulation provides spatial pressure variations in detail, making it possible to capture even the effect of such a small axis rotation. As a result, it is possible to calculate the slight shift of maxima  $C_p$  from the center of the façades due to the  $6.5^\circ$  angle. Furthermore, due to this slight axis rotation, slightly different mean  $C_p$  values arise for identical façades, such as North and South, and East and West façades.

Figure 3.10 shows the  $C_p$  distribution on the North and East façades for two microclimatic cases: exposed and partially sheltered reference building (Figure 3.5). The shielding effect provided by the obstacle placed closed to the North-East corner of the reference building is reflected on the calculated wind pressure coefficient distribution along the two façades (Figure 3.10). The microclimatic effect is also captured at the calculated surface-averaged wind pressure coefficients for the two façades. Indicatively, the calculated mean  $C_p$  value for the North façade for the exposed microclimatic case is 0.36, while for the sheltered microclimatic case is -0.22. As far as the East façade is concerned,



the mean  $C_p$  value for the exposed microclimatic case is 0.20, while the corresponding  $C_p$  value for the sheltered microclimatic case is calculated at 0.24, suggesting an interesting change on the wind flow around the reference building due to the obstacle placement that lead to increased wind-induced pressures. As a result, the determination of wind pressure coefficients at building level, by taking into account the actual surroundings of the building investigated, seems to be a suitable method to capture the microclimatic effect with high spatial accuracy.

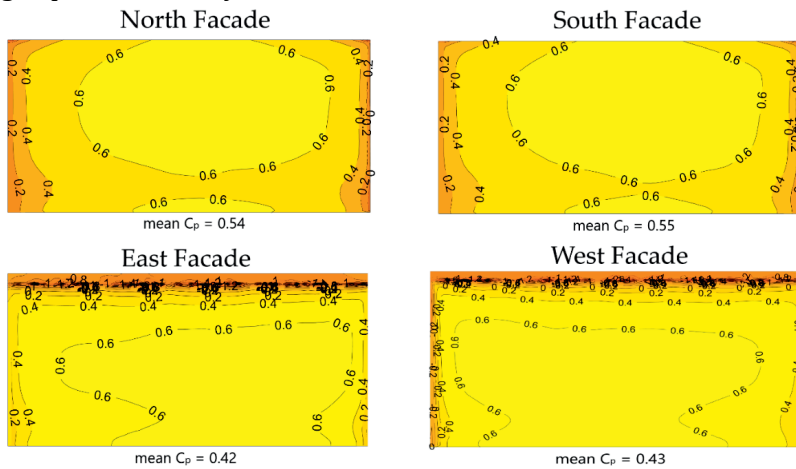


Figure 3.9.  $C_p$  variation on the four exposed building façades for wind direction normal to façade, calculated through OpenFOAM (Paper IV).

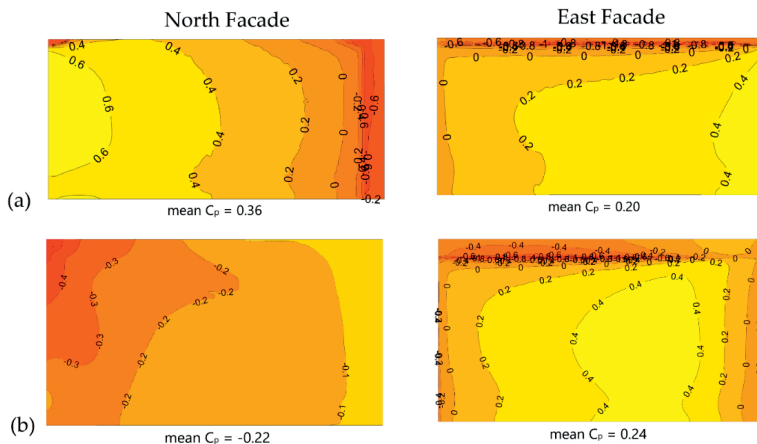


Figure 3.10.  $C_p$  variation on a) the exposed and b) the sheltered North and East building façades for wind direction of 45 degrees, calculated through OpenFOAM (Paper IV).

The wind pressure coefficients for the twin reference buildings were calculated based on the on-site pressure measurements and are presented below (Figure 3.12). Due to the fact that the dominant wind direction during the measuring period was North (Figure 3.11), only wind pressure coefficients corresponding to North wind direction ( $337.5^\circ < \theta_w < 22.5^\circ$ ) were calculated. The freestream pressure and wind velocity used for the calculation of the wind pressure coefficient according to Equation 2.8 (Section 2.2.2) were also measured on site, while the air density was calculated based on the temperature, humidity and pressure values provided by the local weather station (Paper V).

Figure 3.12 shows that the measured wind pressure coefficients on the windward façade of the exposed to wind, North building, vary significantly spatially. The  $C_p$  value of the 'top east' measuring position presents a negligible deviation from the corresponding 'top center' position that has a measured  $C_p$  value of 0.68. However, the 'top west' measuring position presents a noticeable difference as the measured  $C_p$  value is 0.56, which is the potential result of the microclimate formed and the effect of the surroundings on the determination of the air flow around buildings, and consequently on the wind-induced pressures. Furthermore, the lowest measured wind pressure coefficients are on the 'middle' measuring zone of the windward façade, and not on the 'low', contrary to what might have been expected, viz. the  $C_p$  values decreasing as the positions are moving lower across the vertical axis of the building. Characteristically, the  $C_p$  value of the 'middle center' measuring position is measured at 0.32, while the corresponding  $C_p$  value of the 'low center' position is at 0.65. Despite the fact that the 'middle center' position is approximately situated at the stagnation point where the pressure is expected to be the highest, the measured wind pressure coefficient is unexpectedly low. Since neither wind or turbulence measurements have been performed on site, it can only be assumed that this peculiar distribution of wind pressure coefficients along the vertical axis of the building envelope is potentially the result of a unique wind microclimate formed by the local site morphology. Small difference is presented between the center and west position along the 'middle' height zone with the 'middle west'  $C_p$  value measured at 0.35.

The substantial wind shelter provided by the North building to its twin is also captured by the measured wind pressure coefficients on the South Building that remain significantly low, fluctuating slightly around 0. Furthermore, since the windward façade of the sheltered South building is entirely sheltered by its

twin, negligible spatial variations on the measured wind pressure coefficients occur.

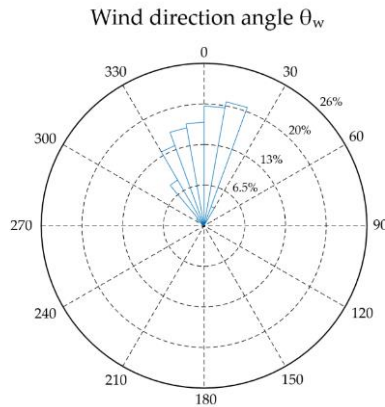


Figure 3.11. Wind direction measured at the local weather station during the measurement period. Only data that correspond to North wind direction ( $337.5^\circ < \theta_w < 22.5^\circ$ ) were used for the determination of the wind pressure coefficients (Paper V).

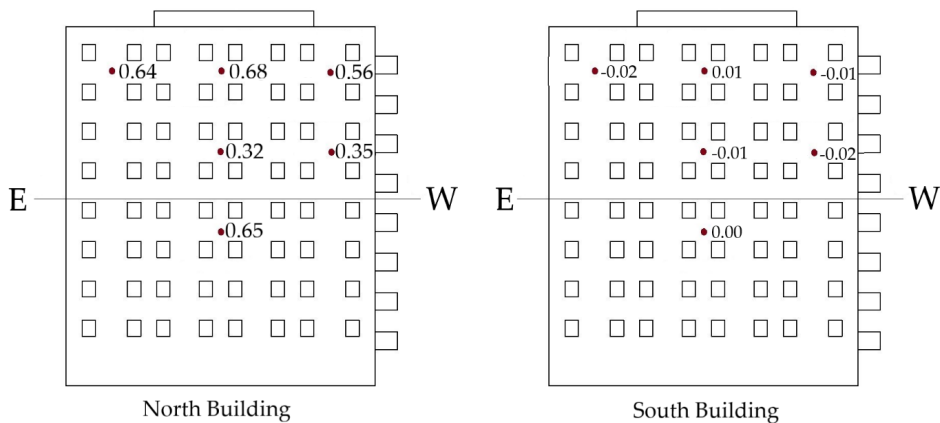


Figure 3.12. Measured wind pressure coefficients on the windward façades of the twin buildings for North ( $0^\circ$ ) wind direction (Paper V).

Both CFD simulations and full-scale measurements reveal spatial variations of the wind-induced pressure coefficients. Especially, for medium- and large-scale buildings, the wind pressure coefficients can vary significantly along the building surfaces. The spatial  $C_p$  distributions are essentially influenced by the microclimate. The determination of building-specific wind pressure coefficients can capture both small and large microclimatic effects, such as the

sheltering effect of neighbouring buildings or obstructions, or even slight deviations from the orthogonal axes. Consequently, the determination of building-specific wind pressure coefficient can be beneficial for both small- and large- scale buildings, as it can reflect sufficiently the microclimatic boundary conditions of the building investigated based on its individual surroundings and architecture.

### 3.5 Improving the accuracy of air infiltration calculation

The wind pressure coefficients can be used on building energy simulation for the calculation of the wind-induced air infiltration, as described in Section 2.2.2. Therefore, the use of building-specific wind pressure coefficients, that bear incorporated the building's microclimatic conditions, on the building energy simulations was investigated (Paper II and Paper IV).

The building-specific  $C_p$  values calculated for the main building of the meteorological station through CFD simulations, were used as microclimatic boundary conditions on building energy simulations performed with a third-party interface for EnergyPlus. The air infiltration rates calculated using building-specific  $C_p$  were compared with the corresponding rates calculated using the reference building's air leakage number  $n_{50}$  and also using tabulated  $C_p$  values provided by the Air Infiltration and Ventilation Center (Orme, 1998). Tracer gas methods performed on the reference building determined the accuracy of each method followed on the calculation of air infiltration rates.

As it has already been discussed in Section 3.4, the building-specific wind pressure coefficients calculated for the meteorological station building were able to capture the microscale effect. On the other hand, the wind pressure coefficients provided by the AIVC database address only simple cases of rectangular or square buildings under generic exposure conditions. The generic nature of the building geometries and exposure/shelter conditions given, consist a limitation of the tabulated  $C_p$  values, as the wind pressure coefficients represent very generic microclimatic conditions and not building-specific. The database  $C_p$  values from the category that approximates better the reference building were chosen. The differences between building-specific  $C_p$  values and tabulated  $C_p$  for the two microclimatic cases considered are displayed on Tables 3.1 and 3.2.

Although the reference building is a simple architectural case and its geometry can be found on the categories provided by the AIVC database, the database  $C_p$  values differ from the building-specific  $C_p$  values even for the exposed microclimatic case. In contrast to the tabulated  $C_p$  values, that are identical for symmetrical wind directions, such as  $0^\circ$  and  $180^\circ$ , the building-specific values calculated through CFD simulations can capture even the effect caused by the orientation angle of  $6.5^\circ$ . For example, the database  $C_p$  value for wind direction  $0^\circ$  (normal to wall) is 0.6 for both the North and the South façade, while the corresponding building-specific  $C_p$  values are 0.54 for the North façade and 0.55 for the South façade (Table 3.1).

Table 3.1. Surface-averaged  $C_p$  values for the exposed microclimatic case given by AIVC database and calculated through CFD simulations using OpenFOAM (OF) (Paper IV)

Wind direction (normal to wall)	North Façade		East Façade		South Façade		West Façade	
	AIVC	OF	AIVC	OF	AIVC	OF	AIVC	OF
$0^\circ$	0.6	0.54	0.5	0.42	0.6	0.55	0.5	0.43
$45^\circ$	0.2	0.36	0.25	0.29	0.2	0.36	0.25	0.27
$90^\circ$	-0.9	-0.54	-0.5	-0.2	-0.9	-0.51	-0.5	-0.21
$135^\circ$	-0.6	-0.26	-0.8	-0.34	-0.6	-0.26	-0.8	-0.33
$180^\circ$	-0.35	-0.09	-0.7	-0.24	-0.35	-0.09	-0.7	-0.25
$225^\circ$	-0.6	-0.24	-0.8	-0.32	-0.6	-0.23	-0.8	-0.32
$270^\circ$	-0.9	-0.34	-0.5	-0.28	-0.9	-0.36	-0.5	-0.28
$315^\circ$	0.2	0.19	0.25	0.2	0.2	0.19	0.25	0.22

Table 3.2. Surface-averaged  $C_p$  values for the sheltered microclimatic case given by AIVC database and calculated through CFD simulations using OpenFOAM (OF) (Paper IV)

Wind direction (normal to wall)	North Façade		East Façade		South Façade		West Façade	
	AIVC	OF	AIVC	OF	AIVC	OF	AIVC	OF
$0^\circ$	0.4	0.53	0.25	0.59	0.4	0.57	0.25	0.48
$45^\circ$	0.2	-0.22	0.06	0.31	0.2	0.38	0.06	0.27
$90^\circ$	-0.6	-0.14	-0.35	-0.13	-0.6	-0.48	-0.35	-0.19
$135^\circ$	-0.5	-0.27	-0.6	-0.32	-0.5	-0.26	-0.6	-0.18
$180^\circ$	-0.3	-0.07	-0.5	-0.27	-0.3	-0.06	-0.5	-0.24
$225^\circ$	-0.5	-0.2	-0.6	-0.34	-0.5	-0.23	-0.6	-0.33
$270^\circ$	-0.6	-0.47	-0.35	-0.24	-0.6	-0.35	-0.35	-0.26
$315^\circ$	0.2	0.21	0.06	0.24	0.2	0.19	0.06	0.24

The most important differences appear on the sheltered microclimatic case. The building-specific wind pressure coefficients are able to capture the sheltering effect caused by the specific obstacle placed close to the North-East corner of the reference building. More specifically, the calculated  $C_p$  value through CFD simulations for the North façade and for North-East wind ( $45^\circ$ ) is -0.22. On the other hand, the generic sheltering conditions of the database are not able to capture such individual microscale effects and the corresponding  $C_p$  value given is 0.2.

Figures 3.13 and 3.14 show that for both microclimatic cases the use of building-specific wind pressure coefficients on the building energy simulation leads to more accurate air infiltration rates compared to the other two methods tested. The use of the air leakage number  $n_{50}$  gives similar results for every measuring 'Day' regardless the microclimatic case tested. The air leakage number  $n_{50}$  describes the air changes caused by 50 Pa pressure difference along the building envelope, and expresses the building's airtightness level. The representative air leakage number  $n_{50}$  provided by national standard cannot introduce any microclimatic information on the building energy calculation, as it depends only on building characteristics, such as construction type, age, etc. The energy simulation tool uses the air leakage number  $n_{50}$  as a reference in order to calculate the air changes of the building based on the actual wind conditions that usually cause lower than 50 Pa pressure difference along the building envelope. Therefore, the calculated air changes for the reference building are lower than the given air leakage number. The results indicate that the use of the air leakage number  $n_{50}$  as input on the building energy simulation produce a deviation of approximately 5% for the exposed case and approximately 28% for the sheltered microclimatic case. However, it is reminded the results are calculated using the measured on-site air leakage number  $n_{50}$ . The corresponding  $n_{50}$  provided by the national standard is approximately 50% lower than the measured, and therefore it is expected that the errors corresponding to the air infiltration calculation would increase proportionally.

The tabulated  $C_p$  values give a crude approximation of the actual air infiltration rates due to their generic nature. Overall, the results show that they tend to overestimate the air infiltration rates of the reference building by average 20% for the exposed microclimatic case, and underestimate them by up to 35% for the sheltered microclimatic case.

On the other hand, the use of building-specific  $C_p$  values predicts air infiltration rates that deviate only by an average 2% from the corresponding measured rates for the exposed microclimatic case. Although, the calculation error increases for the sheltered microclimatic case, they still produce the lowest deviation from the measured air infiltration rates by an average 20%.

The use of building-specific wind pressure coefficients improved significantly the accuracy of the air infiltration calculation during building energy simulations, since building-specific  $C_p$  values manage to introduce rather efficiently the microclimatic conditions of the building examined. Consequently, the more accurate calculation of air infiltration can improve the overall building energy calculation. Indicatively, it is mentioned that the heat loss coefficient due to air infiltration on the Norwegian national standard is calculated based on the following equation:

$$H_{inf} = 0.33 \cdot n_{inf} V \quad (2.28)$$

Where

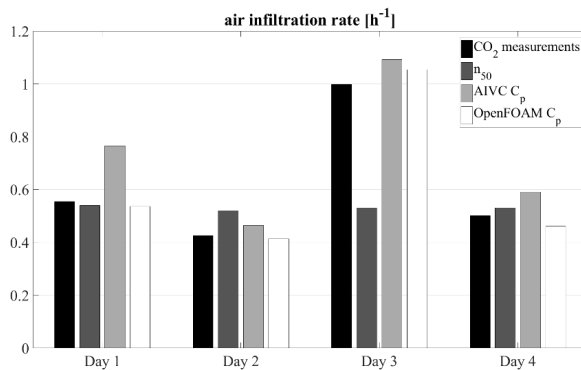
$H_{inf}$  = is the heat loss coefficient [W/K]

0.33 = is the air's heat capacity per volume [Wh/m<sup>3</sup>K]

$n_{inf}$  = is the air change rate [h<sup>-1</sup>]

$V$  = is the heated volume [m<sup>3</sup>]

As a result, the error on the air infiltration rate calculation introduces a proportional error to the calculation of the heat losses due to infiltration.



3.13. Measured and calculated air infiltration rates for the exposed microclimatic case (Paper IV).

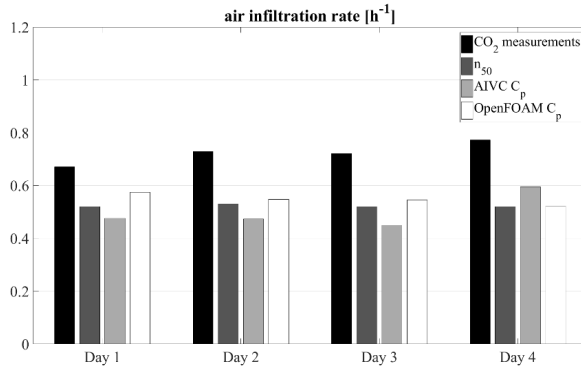


Figure 3.14. Measured and calculated air infiltration rates for the sheltered microclimatic (Paper IV).

### 3.6 Fluctuating wind pressure coefficients

The full-scale measurements of wind pressure coefficients that were performed on the reference twin buildings showed that the measured wind pressure coefficients vary significantly spatially along the windward façade of the exposed building (Figure 3.12), as well as that they fluctuate significantly within time (Figure 3.15).

The use of fluctuating wind pressure coefficients for the calculation of air flows through an ideal crack was researched in Paper V. An ideal gap was chosen due to the fact that wind pressure coefficients were acquired only on the windward façades of the reference twin buildings. Therefore, a qualitative evaluation was performed, and the pressure difference across the ideal gap was assumed to be equal to the pressure difference between the impinging wind pressure on façade and the free stream wind pressure. Since all reference pressure taps were placed at the same position over the rooftop of the reference buildings, the free stream wind pressure is equal for all positions. Therefore, the calculated air flows through an ideal crack can reveal the impact of position-specific wind induced pressures along the various measuring positions, since the reference pressure is equal for all measuring positions.

Probability distribution functions (pdf) have previously been used in literature to describe the fluctuation of wind speed and wind-pressure coefficients (Quan et al., 2014; Calif and Schmitt, 2012; Zaharim et al., 2009). In order to combine the probability distribution function (pdf) of the measured fluctuating wind pressure coefficients with the pdf of the measured wind speeds (Figure 3.16.a),



the Monte Carlo method was chosen to be employed. Furthermore, the airflows through an ideal gap were calculated using the time-averaged  $C_p$  value in combination with the wind speed pdf (Figure 3.16.b). The results were compared with the actual air flow distribution calculated using the instantaneous measured wind pressure coefficient and the corresponding measured wind speed at each time step (Figure 3.17). The applicability and accuracy of the statistical Monte Carlo method, that can account for the fluctuating nature of wind pressure coefficients, for the determination of air infiltration rates was evaluated

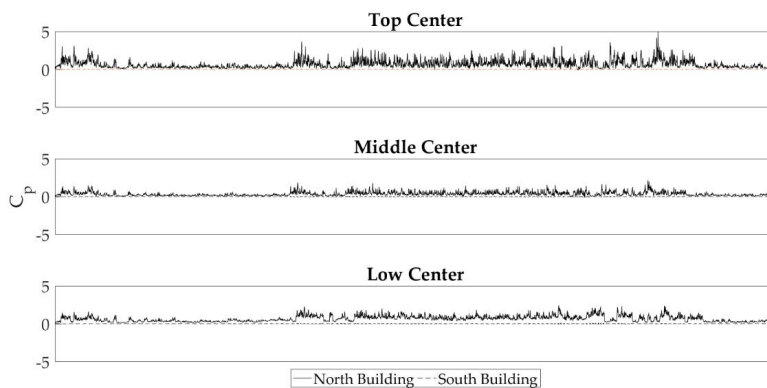


Figure 3.15. Measured pressure coefficients at the center measuring positions of the windward façades of the twin buildings (Paper V). The abscissa axis correspond to the complete measuring period of approximately 5 days.

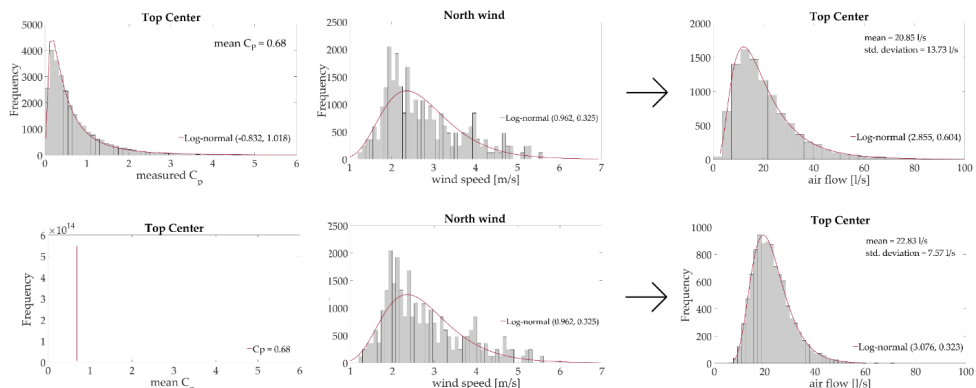


Figure 3.16. Example of Monte Carlo simulations: (a) using the probability distribution of measured  $C_p$  values; (b) using the time-averaged measured  $C_p$  value (Paper V).

Figure 3.17 shows that both the use of fluctuating  $C_p$  and mean  $C_p$  values produce resulting air flow pdfs that capture the actual distribution's shape. Both methods tend to overestimate the airflow through the ideal gap, with the use of mean  $C_p$  value having the biggest deviation. The RMSE deriving from the comparison of the sample mean airflow and measured airflow at each measuring position was calculated (Table 3.3). The sample mean airflow corresponds to the mean value of airflows produced using Monte Carlo simulations, while the measured airflow corresponds to the mean value of the actual airflows calculated using the measured wind pressure coefficient and the corresponding measured wind speed at each time step. The use of fluctuating  $C_p$  values produces the lowest prediction error with only 1.51 l/s, while the use of mean (time-averaged)  $C_p$  values produces an error of 3.12 l/s.

Table 3.3. Mean air flows using measured data and sample average air flows calculated through the Monte Carlo Simulations. '*Measured*' corresponds to the actual flows calculated using measured wind pressure coefficient and corresponding measured wind speed at each time step. '*Fluctuating  $C_p$* ' corresponds to the sample air flows calculated through the Monte Carlo method using pdf for both wind speed and wind pressure coefficients. '*Mean  $C_p$* ' corresponds to the sample air flows calculated through the Monte Carlo method using pdf for wind speed and a mean (time-averaged)  $C_p$  value. '*Mean  $C_p$  +  $U_{hourly}$* ' corresponds to air flows calculated using hourly wind speeds and a mean (time-averaged)  $C_p$  value.

	Top East	Top Center	Top West	Middle Center	Middle West	Low Center	RMSE
<b>Measured</b>	18.59 l/s	19.27 l/s	17.68 l/s	13.52 l/s	13.32 l/s	19.29 l/s	
<b>Fluctuating <math>C_p</math></b>	20.22 l/s	20.85 l/s	19.18 l/s	14.92 l/s	14.73 l/s	20.80 l/s	1.51 l/s
<b>Mean <math>C_p</math></b>	22.12 l/s	22.83 l/s	20.75 l/s	16.61 l/s	15.62 l/s	22.29 l/s	3.12 l/s
<b>Mean <math>C_p</math> + <math>U_{hourly}</math></b>	20.37 l/s	22.44 l/s	20.37 l/s	16.10 l/s	15.40 l/s	21.94 l/s	2.53 l/s

The use of probability distribution functions for both wind pressure coefficients and wind speeds seems to be able to reflect the wind gustiness effect, which is crucial to the wind-induced air infiltration. The results give an indication that the use of fluctuating  $C_p$  values can improve even further the accuracy of the air infiltration calculation. Indicatively, it is mentioned that the use of probability distribution functions for  $C_p$  values and wind speeds can potentially increase the accuracy of air infiltration calculation by approximately 32% compared to the conventional calculation method that employs mean  $C_p$  values and hourly-averaged wind speeds.

In addition, the measured wind pressure coefficients highlight once more the importance of determining  $C_p$  values spatially. The difference on the  $C_p$  values

of the various measuring positions has an immediate impact on the calculation of their corresponding air flows, as positions with higher  $C_p$  values correspond to significantly higher calculated air flows. Previous studies have also highlighted that the use of spatially local  $C_p$  values instead of surface-averaged can be beneficial for the calculation of wind-driven infiltration (Costola et. al, 2010). For medium- and high-rise buildings, local  $C_p$  values can be attributed in detail to the various building components or surfaces by taking into consideration their height from ground and distance from the central axis of the building. As a result, the microclimatic boundary conditions would be better represented during the building energy simulation and the accuracy of the air infiltration rate calculation is expected to increase.

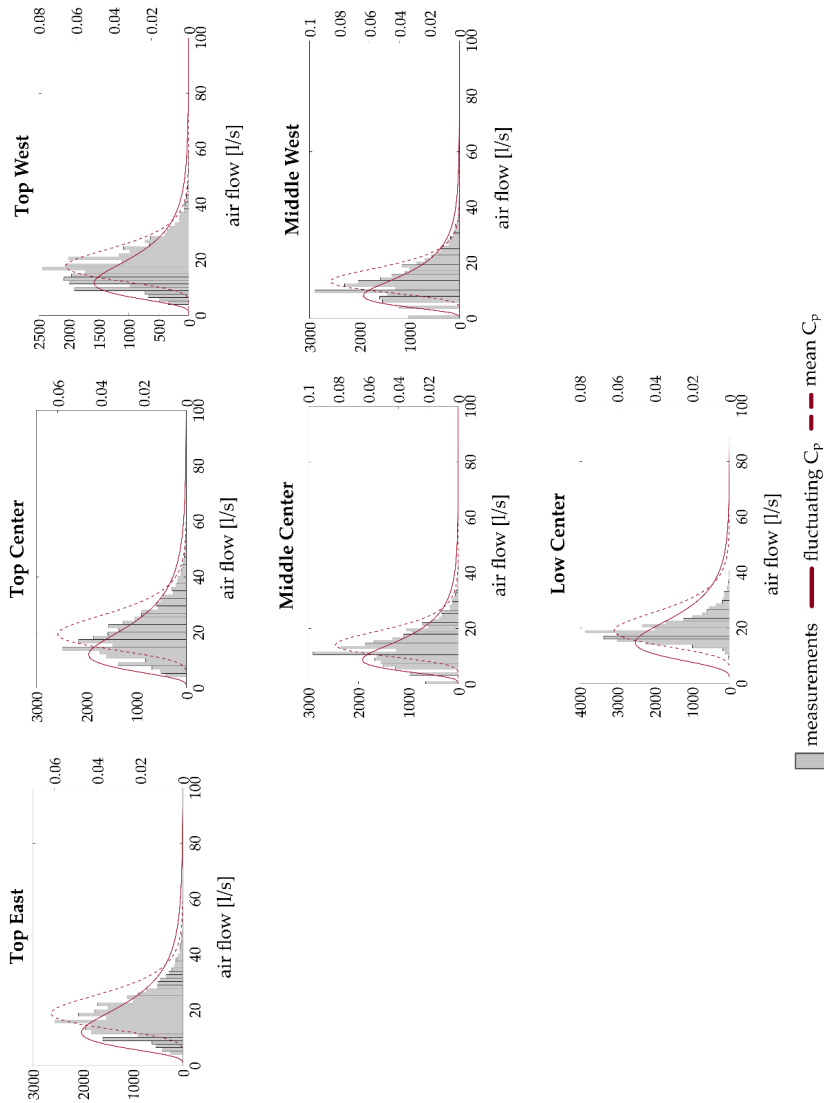


Figure 3.17. Distributions of calculated air flows based on measured  $C_p$  values and measured wind speeds on the six measuring positions on the windward façade of the exposed North Building, and the probability distribution functions of air flows calculated using fluctuating  $C_p$  values and mean  $C_p$  values through Monte Carlo simulations (Paper V).

## 4. Conclusions, limitations and further research

The research conducted highlights that the micro scale climate is of great significance for the building performance simulation. The introduction of microclimate in simulation models for buildings can lead towards more accurate and realistic predictions, thus facilitating the development of more sustainable building solutions.

Solar radiation and wind-driven rain are crucial to the surface temperature and moisture content of external building surfaces. The research conducted showed that the impinging solar radiation and rain on a building façade is determined by the surroundings and the façades spatial architectural details. The one-dimensional model developed is able to predict the microclimatic surface conditions of a building surface with high spatial accuracy. As a result, a spatial illustration of the façade's hygrothermal conditions can be generated. The model can be combined with existing mould-growth, decay or discoloration models, in order to define high-risk areas that can encourage such phenomena. The test cases examined reflect two characteristic building envelope examples of the Scandinavian architecture and, therefore, the model is applicable to the majority of building stock, which consists of well-insulated building envelopes with wooden cladding or brick façades. As a result, it can be used as a decision support for façade material during both the design and retrofitting phase.

The micro scale wind effects were also documented during the research conducted within the context of this PhD project. On-site measurements on both low- and medium- rise buildings showed that the wind-induced pressures along the building façades essentially reflect the local microclimate. Furthermore, they revealed important spatial pressure variations along the building façades, especially for medium-scale buildings.

Wind-induced pressure coefficients, that are determined at building level, were found to be capable to capture the microclimatic effect, as they vary accordingly to wind-induced pressures along the building surfaces. Computational fluid dynamics (CFD) methods can be employed to define building-specific  $C_p$  values with high spatial accuracy.

The use of building-specific wind pressure coefficients as appropriate microclimatic boundary conditions on the building energy simulation (BES), and specifically for the air infiltration calculation, was evaluated. Tracer gas measurements performed on a reference building indicated the advantage of

using the CFD method over other conventional methods, in the air infiltration calculation. According to the results, the use of building-specific  $C_p$  values on BES produces more accurate air infiltration rates compared to conventional methods, due to the fact that it can account for the microclimatic effect. Large majority of the building stock consist of old and rather leaky buildings, like the reference case. The use of building-specific  $C_p$  values can improve the overall building energy demand calculation at a very local scale and can be useful for planning energy distribution on city grid or retrofitting old buildings.

On-site measurements of wind pressure coefficients revealed that  $C_p$  values, not only vary significantly spatially along building façades, but also they fluctuate within time. Probability distribution functions (pdf), such as logarithmic normal distribution, were found to represent adequately the fluctuating nature of  $C_p$  values. Furthermore, the research showed that the use of such  $C_p$  pdf in combination with wind speed probability distribution functions by means of the Monte Carlo method has the potential to improve even further the air infiltration calculation.

Summarizing, the main findings of the current PhD research in brief are:

- Microclimate can significantly affect the building performance and should be taken into account during the simulation process. Consequently, the prediction accuracy regarding both the hygrothermal performance of the building envelope and the building energy consumption increases.
- The façade hygrothermal conditions can be predicted with spatial accuracy through the suggested model, accounting for both the microclimate and the building's architectural characteristics.
- Wind pressure coefficients vary significantly along the building façades, especially for medium- and large-scale buildings, and are essentially determined by the micro scale (surroundings, terrain, obstacles, etc).
- Building-specific wind pressure coefficients can account for the microclimate and introducing them into building energy simulation can increase the accuracy of the air infiltration calculation, even for low-rise buildings. Consequently, the use of building-specific wind pressure coefficients as microclimatic boundary conditions in BES can contribute to the increased prediction accuracy of a building's energy demands.

- The use of probability distribution functions of  $C_p$  values and wind speeds by means of the Monte Carlo Method has the potential to increase even more the accuracy of the air infiltration calculation.

Due to limited resources and time restrictions within the PhD framework, some omissions, assumptions and simplifications were made in order to facilitate the research process. These constitute the basis of the limitations of the current PhD research work.

As far as the simplified hygrothermal model is concerned, its main limitations revolve around the fact that the model disregards the latent heat of phase change, longwave radiation and thermal bridging effect. Furthermore, the model has been developed for and validated against well-insulated building envelopes that are usually found in cold climates. Its applicability for lightly insulated constructions in warmer climates remains to be further tested and validated. In addition, a limitation of the current model is that its accuracy for predicting surface moisture content in masonry façades has not been validated against on-site measurements, but only against simulation results derived from an advanced numerical tool.

Regarding the building-specific wind pressure coefficients and their significance for the calculation of air infiltration rates, only indirect and qualitative methods have been used for the validation of the method. The indirect method involved the comparison of calculated air infiltration rates using building-specific  $C_p$  values with the corresponding measured air infiltration rates. A direct comparison of the simulated wind pressure coefficients with measured wind pressure coefficients on the reference building, and consequently the comparison of the corresponding calculated and measured air changes, would have been more appropriate. The qualitative method involved the air flow through an ideal gap for the medium-rise, since it was possible to acquire measured wind pressure coefficients only for the windward façade of the building.

In addition, the boundary conditions and the discretization schemes used during the CFD simulations should have been tested in advance against a known benchmark. Although they have been based on previous studies and findings, the validation against a benchmark would have provided a better indication regarding the accuracy of the methodology followed.

Furthermore, during the measurements of wind pressure coefficients on the medium-rise only the freestream pressure and wind velocity on the rooftop of the building, along with wind-induced pressures on the windward façade, were recorded. Due to lack of measuring equipment, the wind velocity and turbulence on the various measuring positions were not possible. These additional information would have probably given a deeper understanding over the wind-induced pressure variations along the façade, as well as the fluctuating nature of the wind pressure coefficients.

The current PhD research project has been focused on the microclimate effect on buildings and on determining potential methods to introduce it in simulation models for buildings. Further research can enhance and improve even more the building performance simulation by accounting for the microclimate.

The surface hygrothermal model presented in the current PhD project has the possibility to be developed further by including the latent heat of phase change and longwave radiation. More details on the geometrical modelling can also improve the spatial accuracy of the presented model. Furthermore, surface moisture measurements on brick façades can help define with higher accuracy the performance of the presented model and potentially help with further optimization of the moisture modelling.

Moreover, the studies regarding the building-specific wind pressure coefficients have been limited in only two microclimatic cases (exposed and partially sheltered). However, it has been shown that various microclimates can be found within the border of the same geographic area depending on the local typology scheme (Figure 1.7). Therefore, full-scale measurements of wind pressure coefficients at various district typologies could lead to the development of updated  $C_p$  databases that include a plethora of characteristic typologies and represent more accurately the corresponding microclimates.

Although the PhD research has been limited in low- and medium- rise buildings, the spatial variation of the wind-induced pressures along building façades has been illustrated quite clearly. However, surface-averaged  $C_p$  values can be inappropriate microclimatic boundary conditions for medium- or large- scale buildings and lead to miscalculation of the air infiltration. Further tracer gas measurements on large-scale buildings can help determine the spatial



resolution required for determining local building-specific wind pressure coefficients that can be used as input for the calculation of air infiltration.

The current PhD study indicated that the use of probability distribution functions (pdfs) for fluctuating  $C_p$  values and wind speeds can improve the air infiltration calculation. Further research can aim on introducing the pdfs of  $C_p$  values and wind speeds by means of the Monte Carlo method to building energy simulation tools in order to ameliorate the overall building energy calculation and consequently the overall building performance simulation.

## References

- A.J. Stamm. (1927). The Electrical Resistance of Wood as a Measure of its Moisture Content. *Industrial and Engineering Chemistry, September*, 1021-1025
- Abuku, M., Janssen, H. and S. Roels. (2009). Impact of wind-driven rain on historic brick wall buildings in a moderately cold and humid climate: Numerical analyses of mould growth risk, indoor climate and energy consumption. *Energy and Buildings, 41(1)*, 101-110
- Abuku, M., Janssen, H., Poesen, J. and S. Roels. (2009). Impact, absorption and evaporation of raindrops on building façades. *Building and Environment, 44(1)*, 113-124
- Ajanovic, A. and R. Haas. (2016). Dissemination of electric vehicles in urban areas: Major factors for success. *Energy, 115(2)*, 1451-1458
- Allegrini, J., Dorer, V. and J. Carmeliet. (2012). Influence of the urban microclimate in street canyons on the energy demand for space cooling and heating of buildings. *Energy and Buildings, 55*, 823-832
- Allegrini, J., Dorer, V. and J. Carmeliet. (2015). Coupled CFD, radiation and building energy model for studying heat fluxes in a urban environment with generic building configurations. *Sustainable Cities and Society, 19*, 385-394
- Allegrini, J., J. Kampf, V. Dorer and J. Carmeliet. (2013). Modelling the urban microclimate and its influence on building energy demands of an urban neighbourhood. *Proceedings of CISBAT 2013 Cleantech for Smart Cities and Buildings II* (pp. 867-872)
- American Society for Testing and Material (ASTM). (2006). *International Standard E741-06. Standard test method for determining air change in a single zone by means of a tracer gas dilution*
- Andrady, A.I., Hamid, S.H., Hu, X. and A. Torikai. (1998). Effects of increased solar ultraviolet radiation on materials. *Journal of Photochemistry and Photobiology, 46*, 96-103
- Andrady, A.I., Hamid, H. and A. Torikai. (2011). Effects of solar UV and climate change on materials. *Photochemical and Photobiological Sciences, 10*, 292-300
- Anthopoulos, L., Giannakidis, G. and Sakkas. (2016). Realizing, Modeling and Evaluating City's Energy Efficiency: the case of InSmart in the city of Trikala, Greece. *Proceedings of the 3rd International Conference for E-democracy and Open government, Asia*, p. 7-9
- Avdelidis, N.P. and A. Moropoulou. (2003). Emissivity considerations in building thermography. *Energy and Buildings, 35*, 663-667
- B. Blocken. (2014). 50 years of Computational Wind Engineering: Past, Present and Future. *Journal of Wind Engineering and Aerodynamics, 129*, 69-102
- B.D. Hunn. (1996). *Fundamentals of Building Energy Dynamics*. Solar Heat Technologies, USA

- Bagavathiappan, S., Lahiri, B.B., Saravanan, T., Philip, J. and T. Jayakumar. (2013). Infrared Thermography for condition monitoring – a review. *Infrared Physics and Technology*, 60, 35-55
- Balaras, C.A. and A.A. Argiriou. (2002). Infrared thermography for building diagnostics. *Energy and Buildings*, 34, 171-183
- Barnaby, C.S. and D.B. Crawley. (2011). Weather data for building performance simulation. *Building performance simulation for design and operation*. Spon Press, New York, NY, USA
- Beijer, O. (1977). Concrete walls and weathering. *RILEM/ASTM/CIB Symposium on Evaluation of the Performance of External Vertical Surfaces of Buildings*, Otaniemi, Espoo, Finland, 23-31 August & 1-2 September
- Berdahl, P., Akbari, H., Levinson, R. and W.A. Miller. (2008). Weathering of roofing materials – An overview. *Construction and Building Materials*, 22(4), 423-433
- Berroir, S., Debrie, J. and J. Maulat. (2018). Policy tools for post-car mobility: a comparative analysis of five European metropolitan areas – Amsterdam, Bruxelles, Geneve, Oslo, Paris. *AESOP Congress-Association of European Schools in Planning*
- Bittelli et al. (2008). Coupling of heat, water vapour, and liquid water fluxes to compute evaporation in bare soils. *Journal of hydrology*, 362, 191-205
- Blocken, B. and J. Carmeliet. (2004). A review on wind-driven rain research in building science. *Journal of Wind Engineering and Industrial Aerodynamics*, 95(7), 585-607
- Blocken, B., Roels, S. and J. Carmeliet. (2007). A combined CFD-HAM approach for wind-driven rain on building façades. *Journal of Wind Engineering and Industrial Aerodynamics*, 95(7), 585-607
- Bonnema, G. M., Muller, G. and L. Schuddeboom. (2015). Electric mobility and charging: Systems of systems and infrastructure systems. *Proceedings of the 10<sup>th</sup> Systems of Systems Engineering Conference (SoSE), San Antonio, TX, USA*
- C. Alfonso. (2013). Tracer gas technique for measurement of air infiltration and natural ventilation: case studies and new devices for measurement of mechanical air ventilation in ducts. *International Journal of Low-Carbon Technologies*, 10(3), 188-204
- C.Y. Shaw. (1981). *A correlation between Air Infiltration and Air Tightness for Houses in a Developed Residential Area*. National Research Council Canada, Ottawa, OT, Canada, 1981, 87, 333-341
- Calif, R., and F.G. Schmitt. (2012). Modelling of atmospheric wind speed sequence using a lognormal continuous stochastic equation. *Journal of Wind Engineering and Industrial Aerodynamics*, 109, 1-8

- Calvillo, C.F., Sanchez-Miralles, A. and J. Villar. (2016). Energy management and planning in smart cities. *Renewable and Sustainable Energy Reviews*, 55, 273-287
- Charisi, S., Kraniotis, D., Bruckner, C. and K. Nore. (2016). Latent heat sorption phenomena in three building materials: Norwegian spruce (*Picea Abies*), gypsum board and concrete. *Proceedings of World Timber Conference on Timber Engineering, 22-25 August, Vienna, Austria*
- Coakley, D., P. Raftery and M. Keane. (2014). A review of methods to match building energy simulation models to measured data. *Renewable and Sustainable Energy Reviews*, 37, 123-141
- Cochran, L.S. and J.E. Cermak. (1992). Full- and model-scale cladding pressures on the Texas Tech University experimental building. *Journal of Wind Engineering and Industrial Aerodynamics*, 43(1-3), 1589-1600
- COST Action 732. (2007). Best practice guideline for the CFD simulation of flows in the urban environment
- Costola, D., Blocken, B. and J.L.M. Hensen. (2009). Overview of pressure coefficient data in building energy simulation and airflow network programs. *Building and Environment*, 44(10), 2027-2036
- Costola, D., Blocken, B., Ohba, M. and J.L.M. Hensen. 2010. Uncertainty in airflow rate calculations due to the use of surface-averaged pressure coefficients. *Energy and Buildings*, 42(6), 881-888
- Cui, S., Cohen, M., Stabat, P. and D. Marchio. (2015). CO<sub>2</sub> tracer gas concentration decay method for measuring air change rate. *Building and Environment*, 84, 162-169
- D.A. Chwieduk. (2009). Recommendation on modelling solar energy incident on a building envelope. *Renewable Energy*, 34(3), 736-741
- D.W. Etheridge. (2000). Unsteady flow effects due to fluctuating wind pressures in natural ventilation design – mean flow rates. *Building and Environment*, 35, 111-183
- Datcu, S., Ibos, L., Candau, Y. and S. Matei. (2005). Improvement of building wall surface temperature measurements by infrared thermography. *Infrared Physics and Technology*, 46(6), 451-467
- Delaunay, D., Lakehal, D. and D. Pierrat. (1995). Numerical approach for wind loads prediction on buildings and structures. *Journal of Wind Engineering and Industrial Aerodynamics*, 57, 307-321
- Detlef Laussmann and Dieter Helm. (2011). *Air Change Measurements Using Tracer Gases: Methods and Results. Significance of air change for indoor air quality, Chemistry, Emission Control, Radioactive Pollution and Indoor Air Quality*, Dr. Nicolas Mazzeo (Ed.), ISBN: 978-953-307-316-3

Dietsch, P., Franke, S., Franke, B., Gamper, A. and S. Winter. (2015). Methods to determine wood moisture content and their applicability in monitoring concepts. *Journal of Civil Structural Health Monitoring*, 5(2), 115-127

Dorer, V., Allegrini, J., Orehounig, K., Moonen, P., Upadhyay, G., Kampf, J. and J. Carmeliet. (2013). Modelling the urban microclimate and its impact on the energy demand of buildings and building clusters. *13<sup>th</sup> Conference of International Building Performance Simulation Association, Chambéry, France*

Duffie, J.A. and W. Beckman. (2013). *Solar Engineering of Thermal Processes*. 4<sup>th</sup> Ed. John Wiley & Sons Ltd

EN 12831 (European Standard). (2003). Heating systems in buildings – Method for calculation of the design heat load.

EN 13183-2:2002 (European Standard). (2002). Moisture content of a piece of sawn timber-part 2: estimation by electrical resistance method. European Committee for Standardization CEN, Brussels

EN 13829 (European Standard). (2000). Thermal Performance of buildings – Determination of air permeability of buildings – Fan pressurization method

EnergyPlus<sup>TM</sup> Documentation. (2017). *Engineering Reference: The Reference to EnergyPlus Infiltration/Ventilation Calculations*. U.S. Department of Energy

European Commission. (2010). Directive 2010/31/EU of the European Parliament and of the Council of 19 May 2010 on the energy performance of building (recast). *Official Journal of the European Union*, L 153/3

European Commission. (2012). Directive 2012/27/EU of the European Parliament and of the Council of 25 October 2012 on energy efficiency, amending Directives 2009/125/EC and 2010/30/EU and repealing Directives 2004/8/EC and 2006/32/EC. *Official Journal of the European Union*, L 315/1

European Commission. (2018). Directive (EU) 2018/844 of the European Parliament and of the Council of 30 May 2018 amending Directive 2010/31/EU on the energy performance of buildings and Directive 2012/27/EU on energy efficiency. *Official Journal of the European Union*, L 156/75

EVUE-Electric Vehicles in Urban Europe. (2015). Available at: [http://urbact.eu/sites/default/files/import/Projects/EVUE/documents\\_media/EVUE\\_report\\_280912\\_FINAL.pdf](http://urbact.eu/sites/default/files/import/Projects/EVUE/documents_media/EVUE_report_280912_FINAL.pdf)

F. Haghghat, H. Brohus, J. Rao. (2000). Modelling air infiltration due to wind fluctuations – a review. *Building and Environment*, 35, 377-385

FLIR Tools: User Manual. (2011). Publication No. T559600

- FME ZEN – Research Centre on Zero Emission Neighbourhoods in Smart Cities. (2018). *Mapping of the pilot projects within the research centre on zero emission neighborhoods in smart cities*. ZEN Report No. 10-2018
- Gobakis, K. and D. Kolokotsa. (2017). Coupling building energy simulation software with microclimatic simulation for the evaluation of the impact of urban outdoor conditions on the energy consumption and indoor environmental quality. *Energy and Buildings*, 157, 101-115
- H.M. Kunzel. (1995). *Simultaneous Heat and Moisture Transport in Building Components. One- and two-dimensional calculation using simple parameters*. Report. Fraunhofer Institute of Building Physics, Stuttgart, Germany
- Hartley, J. and J. Marchant. (1995). *Methods of determining the moisture content of wood*. Technical Paper No. 41. State Forests of New South Wales, Beecroft, Australia
- Hensen, J.L.M. and R. Lamberts. (2011). *Building performance simulation for design and operation*. Spon Press, New York, NY, USA
- Hou, J., Sun, Y., Kong, X., Wang, P., Zhang, Q. and J. Sundell. (2015). Single and Multiple Zone Methods to Calculate Air change rate in Apartments. *Procedia Engineering*, 121, 567-572
- International Organization for Standardization, ISO 13788. (2012). Hygrothermal performance of building components and building elements -- Internal surface temperature to avoid critical surface humidity and interstitial condensation -- Calculation methods
- International Organization for Standardization, ISO 13788. Hygrothermal Performance of Building Components and Building Elements – Internal Surface Temperature to Avoid Critical Surface Humidity and Interstitial Condensation – Calculation Methods, 2001
- International Organization for Standardization. (2009). ISO 15927-3: Calculation of a Driving Rain Index for Vertical Surfaces from Hourly Wind and Rain Data.
- J. Bear. (1988). *Dynamics of fluids in porous media*. Dover Publications, New York, USA
- J. Crank. (1975). *The mathematics of diffusion*. (2nd Ed). Oxford University Press
- J. Straube. (2007). BSD-014: Air Flow in Buildings. *Building Science Digest*, October 15
- Jacobson et al. (2018). 100% clean and renewable wind, water and sunlight (WWS) all-sector energy roadmaps for 53 towns and cities in North America. *Sustainable Cities and Society*, 42, 22-37
- Janssen, H., Blocken, B. and J. Carmeliet. (2007). Conservative modelling of the moisture and heat transfer in building components under atmospheric excitation. *International Journal of Heat and Mass Transfer*, 50, 1128-1140
- Jokisalo, J., Kalamees, T., Kurnitski, J., Eskola, L., Jokiranta, K. and J. Vinha. (2008). A comparison of measured and simulated air pressure conditions of a detached house in a cold climate. *Journal of Building Physics*, 32(1), 67-89

- K. G. Høyer. (2008). The history of alternative fuels in transportation: The case of electric and hybrid cars. *Utilities Policy*, 16(2), 63-71
- K. Sedlbauer. (2002). Prediction of Mould Growth by Hygrothermal Calculation. *Journal of Building Physics*, 25(4), 321-336
- Karagiozis, A., Kunzel, H. and A. Holm. (2001). *WUFI-ORNL/IBP Hygrothermal Model*
- Karava, P., Stathopoulos, T. and A.K. Athienitis. (2007). Wind-induced natural ventilation analysis. *Solar Energy*, 81(1), 20-30
- Kehrer, Manfred, and Th Schmidt. (2018). Radiation effects on exterior surfaces. *Proceedings of the 8th Symposium on Building Physics in the Nordic Countries, Copenhagen, Denmark*
- Kellert, S.R. (2005). *Building for Life: Designing and Under-Understanding the Human-Nature Connection*; Island Press: Washington, DC, USA, p. 250.
- Kirimtata, A. and O. Krejcar. (2018). A review of infrared thermography for the investigation of building envelopes: Advances and prospects. *Energy and Buildings*, 176, 390-406
- Kohler et al. (2009). A transitions model for sustainable mobility. *Ecological Economics*, 68(12), 2985-2995
- Kohta, U. and J. Straube. (2008). Laboratory calibration and field results of wood resistance humidity sensors. *BEST 1: Building for Energy Efficiency and Durability at the Crossroads*, Minneapolis, MN
- Kontoleon, K.J. and D.K. Bikas. (2007). The effect of south wall's outdoor absorption coefficient on time lag, decrement factor and temperature variations. *Energy and Buildings*, 39, 1011-1018
- Kragh, J., Rose, J. and S. Svendsen. (2005). *Mechanical ventilation with heat recovery in cold climates*. Proceedings of the 7<sup>th</sup> Nordic Symposium on Building Physics
- Kraniotis D.; Aurlien T.; Thiis T.K. (2014). On investigating instantaneous wind-driven infiltration rates using CO<sub>2</sub> decay method. *Int. Journal of Ventilation*, 13(2), 111-124.
- Kraniotis, D., Aurlien, T. and T.K. Thiis. (2014). On investigating instantaneous wind-driven infiltration rates using CO<sub>2</sub> decay method. *International Journal of Ventilation*, 13(2), 111-124
- Kraniotis, D., Thiis, T.K. and T. Aurlien. (2014). A numerical study on the impact of wind gust frequency on air exchanges in buildings with variable external and internal leakages. *Buildings*, 4, 27-42
- Kroese, D.P., Brereton, T., Taimre, T. and Z.I. Botev. (2014). Why the Monte Carlo method is so important today. *WIREs Computational Statistics*, 6(6), 386-392
- Kunzel, H.M. and K. Kiessl. (1997). Calculation of heat and moisture transfer in exposed building components. *International Journal of Heat Mass Transfer*, 40(1), 159-167

- L.C. Burmeister. (1993). *Convective Heat Transfer*. 2<sup>nd</sup> Ed. John Wiley & Sons Inc.
- Lam, J.C. and D.H.W. Li. (1999). An analysis of daylighting and solar heat for cooling-dominated office buildings. *Solar Energy*, 65(4), 251-262
- Lam, J.C., Tsang, C.L., Li, D.H.W. and S.O. Cheung. (2005). Residential building envelope heat gain and cooling energy requirements. *Energy*, 30(7), 939-951
- Lee, J.W., Jung, H.J., Park, J.Y., Lee, J.B. and Y. Yoon. (2013). Optimization of building window system in Asian regions by analysing solar heat gain and daylighting elements, *Renewable Energy*, 50, 522-531
- Levitan, M.L., Mehta, K.C., Vann, W.P. and J.D. Holmes. (1991). Field measurements of pressures on the Texas tech building. *Journal of Wind Engineering and Industrial Aerodynamics*, 38(2-3), 227-234
- Li, D.H.W. and J.C. Lam. (2000). Solar heat gain factors and the implications to building designs in subtropical regions, *Energy and Buildings*, 32(1), 47-55
- Lie, S.K., Vestøl, G.I., Høibø, O.A. and L.R. Gobakken. (2018). Surface mould growth on wooden claddings – effects of transient wetting, relative humidity, temperature and material properties. *Wood Material Science and Engineering*, DOI: [10.1080/17480272.2018.1424239](https://doi.org/10.1080/17480272.2018.1424239)
- Liu, F. (2016). A Thorough Description of How Wall Functions are Implemented in OpenFOAM. *Proceedings of CFD with OpenSource Software*
- Liu, J.Y. (1989). A new method for separating diffusion coefficient and surface emission coefficient. *Wood and Fiber Science*, 21:133-141
- Loomans, M.G.L.C., van Houdt, W., Lemaire, A.D. and J.L.M. Hensen. (2008). Performance Assessment of an Operating Theatre Design Using CFD simulation and Tracer Gas Measurements. *Indoor and Built Environment*, 17(4), 299-312
- Lund, P. D., Mikkola, J. and J. Ypya. (2015). Smart energy system design for large clean power schemes in urban areas. *Journal of cleaner production*, 103, 437-445
- M. Bomberg. (2013). Heat, air and moisture interactions. *Frontiers of Architectural Research*, 2, 116-119
- M. Iqbal. (1983). *An introduction to solar radiation*. Academic Press, Canada
- M.D. Lyberg. (1997). Basic Air Infiltration. *Building and Environment*, 32(2), 95-100
- M.H. Sherman. (1990). Tracer-gas techniques for measuring ventilation in a single-zone. *Building and Environment*, 25(4), 365-374
- M.W. Liddament. (1986). *Air Infiltration Calculation Techniques – An application guide*. Air infiltration and Ventilation Centre, Coventry, Great Britain
- M.W. Liddament. (1996). *A guide to energy efficient ventilation*. Report AIC-TN-VENTGUIDE-1996. Air infiltration and Ventilation Centre, Coventry, Great Britain



- Ma et al. (2018). Dynamic simulation of the atmospheric environment improved by a focus on clean energy utilization of resource-based cities in China. *Cleaner Production*, 192, 396-410
- Mahyuddin, N. and H.B. Awbi. (2016). A review of CO<sub>2</sub> Measurement Procedures in Ventilation Research. *International Journal of Ventilation*, 10(4), 353-370
- Malys, L., M. Musy and C. Inard. (2015). Microclimate and building energy consumption: study of different coupling methods. *Advances in Building Energy Research*, 9(2), 151-174
- Marique, A.F. and S. Reiter. (2014). A simplified framework to assess the feasibility of zero-energy at the neighbourhood/community scale. *Energy and Buildings*, 82, 114-122
- Mazzeo, D., Oliveti, G. and N. Arcuri. (2016). Mapping of the seasonal dynamic properties of building walls in actual periodic conditions and effects produced by solar radiation incident on the outer and inner surfaces of the wall. *Applied Thermal Energy*, 102, 1157-1174
- McClellan, T.M. and Pedersen, C.O. (1997). *Investigation of outside heat balance models for use in a heat balance cooling load calculation procedure*. ASHRAE transactions: Technical and symposium papers, Volume 103, Part 2
- Mendis, P., Ngo, T., Haritos, N. and A. Hira. (2007). Wind Loading on Tall Buildings. *EJSE Special Issue: Loading on Structures*, 41-54
- Metropolis, N. and S. Ulam. (1949). The Monte Carlo Method. *Journal of the American Statistical Association*, 44, 335-341
- Mochida, A., Tominaga, Y. and R. Yoshie. (2006). AIJ guidelines for Practical Applications of CFD to Wind Environment around Buildings. *The Fourth International Symposium on Computational Wind Engineering (CWE2006)*, Yokohama, Japan
- Moonen, P., Defraeye, T., Dorer, V., Blocken, B. and J. Carmeliet. (2012). Urban Physics: Effect of the micro-climate on comfort, health and energy demand. *Frontiers of Architectural Research*, 1, 197-228
- Murakami, S. and A. Mochida. (1988). 3-D numerical simulation of airflow around a cubic model by means of the k- $\epsilon$  model. *Journal of Wind Engineering and Industrial Aerodynamics*, 31:2-3, 283-303
- N. B. Andersen. (2015). Sustainable transformation: building heritage, transformation and sustainability in a holistic perspective. *PHN Conference: Sustainable cities and buildings*, Copenhagen, Denmark
- Nadoushani, Z.S.M., Akbarnezhad, A., Jornet, J.F. and J. Xiao. (2017). Multi-criteria selection of façade systems based on sustainability criteria. *Building and Environment*, 121, 67-78
- Nardi, I., Domenica, P., Ambrosini, D., de Rubeis, T. and S. Sfarra. (2016). U-value assessment by infrared thermography: a comparison of different calculation methods in a guarded hot box. *Energy and Buildings*, 122, 211-221

- Nardi, I., Sfarra, S. and D. Ambrosini. (2014). Quantitative thermography for the estimation of U-value: state of the art and a case study. *Journal of Physics: Conference Series*, 547, 012016
- National Institute of Standards and Technology. (1996). NIST estimates nationwide energy impact of air leakage in U.S. buildings. *Journal of Research of the NIST*, 101(3), 413
- Nikkho, S. K., M. Heidarinejad, J. Liu and J. Srebric. (2017). Quantifying the impact of urban wind sheltering on the building energy consumption. *Applied Thermal Engineering*, 116, 850-865
- Nordwall, U. and T. Olofsoon. (2019). Sustainable Architecture in Northern Subarctic and Arctic Climate. In: Johansson, D. Bagge, H. and Å. Wahlstrom. *Cold Climate HVAC 2018. Springer Proceedings in Energy, Springer, Cham*.
- Notton et al. (2017). Tilos, the first autonomous renewable green island in Mediterranean: A Horizon 2020 project. *Proceedings of the 15<sup>th</sup> International Conference on Electrical Machines, Drives and Power Systems (ELMA), Sofia, Bulgaria*
- Nugraha, Y., Pere, C., Landrieu, J. and C. Nicolle. (2013). A thermal simulation tool for building and its interoperability through the Building Information Modelling (BIM) platform. *Buildings*, 3, 380-398
- Orehounig, K., Mavromatidis, G., Evins, R., Dorer, V. and J. Carmeliet. (2014). Towards an energy sustainable community: An energy system analysis for a village in Switzerland. *Energy and Buildings*, 84, 277-286
- Orme, M., Liddament, M.W. and A. Wilson. (1998). *Numerical Data for Air Infiltration and Natural Ventilation Calculations. Annex V. AIVC*
- Oxizidis, S., Dudek A.V. and N. Aquilina. (2011). Typical Weather Years and the Effect of Urban Microclimate on the Energy Behaviour of Buildings and HVAC Systems. *Advances in Building Energy Research*, 1, 89-103
- Pisello, A. L., G. Pignatta, V. L. Castaldo and F. Cotana. (2015). The Impact of Local Microclimate Boundary Conditions on Building Energy Performance. *Sustainability*, 7, 9207-9230
- Quan, Y., Wang, F. and M. Gu. (2014). A method for estimation of extreme values of wind pressure on buildings based on the generalized extreme value theory. *Mathematical problems in Engineering*, Article ID 926253, 22 pages
- R. Becker. (2008). Fundamentals of performance-based building design. *Building Simulation*, 1(4), 356-371
- R. Priyadarsini. (2009). Urban Heat Island and its Impact on Building Energy Consumption. *Advances in Building Energy Research*, 3, 261-270
- Ren, C., Cai, M., Wang, R., Xu, Y. and E. Ng. (2016). Local Climate Zone (LCZ) classification using the World Urban Database and Access Portal Tools (WUDAPT) method: A case study

in Wuhan and Hangzhou. *4<sup>th</sup> International Conference on Countermeasure to Urban Heat Islands, Singapore*

Richards, P.J. and R.P. Hoxey. (1993). Appropriate boundary conditions for computational wind engineering models using the k- $\epsilon$  turbulence model. *Proceedings of the 1<sup>st</sup> International Symposium on Computational Wind Engineering*, 145-153

Richards, P.J., Hoxey, R.P. and L.J. Short. (2001). Wind pressures on a 6m cube. *Journal of Wind Engineering and Industrial Aerodynamics*, 89, 1553-1564

Robinson, D. and A. Stone. (2004). Irradiation modelling made simple: the cumulative sky approach and its applications. *Proceedings of 21<sup>st</sup> Conference on Passive and Low Energy Architecture, Eindhoven, The Netherlands*

Rode, C. and S.K. Grau. (2010). Whole building simulation model. *ASHRAE, Recent Advances in Energy Simulation: Building Loads, Symposium CH-03-09, Chicago, USA*

Rotronic AG. (2014). *CP11 – Handheld instrument for CO<sub>2</sub>, Humidity and Temperature – Short instruction manual*

Roulet, C.A. and F. Foradini. (2002). Simple and cheap air change rate measurement using CO<sub>2</sub> concentration decays. *International Journal of Ventilation*, 1, 39-44

S.W. Smith. (1997). *The Scientist and Engineer's Guide to Digital Signal Processing*. 2<sup>nd</sup> Ed. California Technical Publishing: San Diego, California, USA

Saleem, M., Chhipi-Shrestha, G., Andrade, M.T.B. and R. Dyck. (2018). Life Cycle Thinking-Based Selection of Building Facades. *Journal of Architectural Engineering*, 24(4), 04018029

Sargent, R., Riley S. and L. Schottle. (2010). Measurement of dynamic sorption behaviour of small specimens of *Pinus Radiata* – Influence of wood type and moisture content of diffusion rate. *Ciencia y Tecnologia*, 12:93-103

Shirzadi, M., Naghashzadegan, M. and P.A. Mirzaei. (2019). Developing a framework for improvement of building thermal performance modelling under urban microclimate interactions. *Sustainable Cities and Society*, 44, 27-39

Simpson, W.T. (1993). Determination and use of moisture diffusion coefficient to characterize drying of northern red oak (*Quercus rubra*). *Wood Science and Technology*, 27:409-420

Simpson, W.T. and J.Y. Liu. (1991). Dependence of the water vapour diffusion coefficient of aspen (*Populus spec.*) on moisture content. *Wood Science and Technology*, 26:9-21

Skaar, C., Labonnote, N. and K. Gradeci. (2018). From Zero Emission Building (ZEB) to Zero Emission Neighbourhoods (ZEN): A Mapping Review of Algorithm-Based LCA. *Sustainability*, 10(7), 2405

SSB – Statistics Norway. (2014). *Energy consumption in households*. 14 July 2014

- SSB – Statistics Norway. (2018). *Generation and consumption of electricity*. 29 November 2018
- SSB – Statistics Norway. (2018). *Over 140 000 electric cars in Norway*. 22 March 2018
- Stewart, I.D. and T.R. Oke. (2012). Local Climate Zones for Urban temperature studies. *Bulletin of the American Meteorological Society*, 93(12), 1879-1900
- Tang, W., Davidson, C.I., Finger, S. and K. Vance. (2004). Erosion of limestone building surfaces caused by wind-driven rain. 1. Field measurements. *Atmospheric Environment*, 38(33), 5589-5599
- Tariku, F., Cornick, S.M. and M.A. Lacasse. (2007). Simulation of wind-driven rain effects on the performance of stucco-clad wall. *Thermal Performance of Exterior Envelopes of Whole Buildings X International Conference, Clearwater Beach, FL, Dec. 2-7, pp. 1-15*
- Taveres-Cachat, E., Grynning, S., Thomsen, J. and S. Selkowitz. (2019). Responsive building envelope concepts in zero emission neighbourhoods and smart cities – A roadmap to implementation. *Building and Environment*, (149), 446-457
- Thiis, T. K., Burud, I., Flø, A., Kraniotis, D., Charisi, S. and P. Stefansson. (2017). Monitoring and simulation of diurnal surface conditions of a wooden façade. *Procedia Environmental Sciences*, 38, 331-339
- Thiis, T., Burud, I., Flø, A., Kraniotis, D., Charisi, S. and P. Stefansson. (2017). Monitoring and Simulation of Diurnal Surface Conditions of a Wooden Surface. *Procedia Environmental Sciences*, 38, 331-339
- Tominaga, Y., Akabayashi, S., Kitahara, T. and Y. Arinami. (2015). Air flow around isolated gable-roof buildings with different roof pitches: Wind tunnel experiments and CFD simulations. *Building and Environment*, 84, 204-213
- Tominaga, Y., Mochida, A., Yoshie, R., Kataoka, H., Nozu, T., Yoshikawa, M. and T. Shirasawa. (2008). AIJ guidelines for practical applications of CFD to pedestrian wind environment around buildings. *Journal of Wind Engineering and Industrial Aerodynamics*, 96(10-11), 1749-1761
- Toparlar, T., B. Blocken, B. Maijeu and G.J.F. van Heijst. (2017). A review on the CFD analysis of urban microclimate. *Renewable and Sustainable Energy Reviews*, 80, 1613-1640
- Tsoka, S. and T.K. Thiis. (2018). Calculation of the driving rain wall factor using ray tracing. *Journal of Wind Engineering and Industrial Aerodynamics*, 179, 190-199
- Tsoka, S., K. Tolika, T. Theodosiou, K. Tsikaloudaki and D. Bikas. (2017). A method to account for the urban microclimate on the creation of ‘typical weather year’ datasets for building energy simulation, using stochastically generated data. *Energy and Buildings*, 165, 270-283

- Vallati, A., De Lieto Vollaro, A., Golasi, I., Barchiesi, E. and C. Caranese. (2015). On the impact of urban micro climate on the energy consumption of buildings. *Energy Procedia*, 82, 506-511
- van Hoof, T. and B. Blocken. (2013). CFD evaluation of natural ventilation of indoor environments by the concentration decay method: CO<sub>2</sub> gas dispersion from a semi-closed stadium. *Building and Environment*, 61, 1-17
- Versteeg, H. K. and W. Malalasekera. (2007). *An Introduction to Computational Fluid Dynamics: The Finite Volume Method*. 2<sup>nd</sup> Edition. Pearson Education
- Vu, T., Loehr, E. and D. Smith. (2018). Probabilistic analysis and resistance factor calibration for deep foundation design using Monte Carlo simulation. *Heliyon*, 4, e00727
- W. Oberle. *Monte Carlo Simulations: Number of Iterations and Accuracy*. Technical Note ARL-TN-0684. US Army Research Laboratory: USA, 2015
- W.C. Feist. (1989). Outdoor Wood Weathering and Protection. *Advances in Chemistry*, 225, 263-298
- W.L. James. (1988). *Electric Moisture Meters for Wood*. General Technical Report FPL-GTR-6. U.S. Department of Agriculture, Madison, WI, USA
- Woloszyn, M. and C. Rode. (2008). Tools for Performing Simulation of Heat, Air and Moisture Conditions of Whole Buildings, *Building Simulation*, 1, 5-24
- Woodard, A. C. and H.R. Milner. (2016). 7 - *Sustainability of timber and wood in construction*. In: *Sustainability of Construction Materials*. 2<sup>nd</sup> Edition. Woodhead Publishing Series in Civil and Structural Engineering
- Xu, H., Li, J., Wu, J. and J. Kang. (2019). Evaluation of wood coverage on building facades towards sustainability. *Sustainability*, 11(5), 1407
- Yang, T., Wright, N.G., Etheridge, D.W. and A.D.Q. Quin. (2006). A comparison of CFD and Full-scale Measurement for Analysis of Natural Ventilation. *International Journal of Ventilation*, 4:4, 337-348
- Yochida, M., Kondo, K. and M. Suzuki. (1992). Fluctuating wind pressure measured with tubing system. *Journal of Wind Engineering and Industrial Aerodynamics*, 42(1-3), 987-998
- Younes, C., Shdid, C.A. and G. Bitsuamlak. (2011). Air infiltration through building envelopes: A review. *Journal of Building Physics*, 35(3), 267-302
- Yuan, X., Liu, X. and L. Zuo. (2015). The development of new energy vehicles for a sustainable future: A review. *Renewable and Sustainable Energy*, 42, 298-305
- Zaharim, A., Razali, A.M., Abidin, R.Z. and K. Sopian. (2009). Fitting of Statistical Distributions to Wind Speed Data in Malaysia, *European Journal of Scientific Research*, 26(1), 6-12

ZenN – Nearly Zero Energy Neighborhoods. (2013). *Common barriers and challenges in current nZEB practice in Europe*. D.1.1 Report, IVL Swedish Environmental Research Institute

ZenN – Nearly Zero Energy Neighborhoods. (2014). *Final report on common definition for nZEB renovation*. D.1.2 Report, IVL Swedish Environmental Research Institute

Paper I



# Prediction model of microclimatic surface conditions on building façades

Stergiani Charisi\*, Thomas K. Thiis, Petter Stefansson, Ingunn Burud

Faculty of Science and Technology, Norwegian University of Life Sciences, 1430, Ås, Norway

## ARTICLE INFO

### Keywords:

Microclimate  
Façade  
Surface temperature  
Moisture content  
Thermography

## ABSTRACT

The microclimatic surface conditions of a building façade are critical for determining the degradation of the façade material. Most models use the ambient temperature and RH to predict mould growth and decay on building materials. On the other hand, Heat, Air and Moisture (HAM) simulation software able to calculate the surface conditions, treats the whole façade uniformly without including architectural characteristics of the façade, such as window sills or overhangs, which can have shadowing effect. A simulation model that takes into consideration both the local microclimate and the spatial architectural characteristics of the façade has been developed to predict the spatial surface temperature and moisture content over a whole façade. The model is validated through measurements for two different building façades – wooden consisting of aspen (*Populus tremula*) and masonry consisting of red fire clay bricks. The measurements include monitoring of the spatial surface temperatures with an infrared camera, and logging of the surface moisture content of selected points on the façade using wood resistance humidity sensors. The validation shows that the simulation model can predict the microclimatic surface conditions with high accuracy and can sufficiently capture the spatial variations of surface temperature and moisture content over a building façade.

## 1. Introduction

Contemporary architectural trends tend to use sustainable materials. Untreated wood is continuously gaining in popularity as façade cladding, while red fire clay bricks remain a traditionally safe aesthetic choice for exterior façades. However, such materials are susceptible to degradation caused by the natural weathering process. One of the main degradation problems caused to porous materials, such as wood and brick, is the potential mould and algae growth [1,2]. Especially for untreated wood, the possibility of discoloration by sunlight is additionally introduced [2]. In addition, the frost decay of porous materials creates a severe concern, especially in cold climates [3].

Extended research studies show that the driving mechanisms for biological growth on building materials are the hygrothermal conditions [1,4–9]. Some of the mathematical models for mould growth consider only the climate conditions for temperature and RH, neglecting the surface conditions of the material [4,5], while others use HAM simulation tools to calculate the surface temperature and moisture [1]. All scientific findings though highlight the importance of fluctuations on moisture and temperature conditions, as they can enhance or delay the biological activity on the material surface [5–7].

Furthermore, plenty of scientific reports study the impact of urban and local microclimate on building performance, and promote the coupling of microclimate models with building performance simulation

[10–12]. Although microclimatic weather conditions have been mostly linked with the building energy, they can also significantly affect the hygrothermal performance of a building. This local microclimate can significantly impact the surface temperatures of building façades and the air temperatures around a building [13]. It also defines the amount of solar radiation and wind-driven rain that impinges on the building façades, which are crucial factors for the degradation of building materials. In addition, the various architectural details of exterior façades, such as window sills or overhangs, will create local areas sheltered from solar radiation and wind-driven rain, thereby promoting individual exterior surface microclimates for each façade. As a result, the exterior microclimate significantly affects the exterior surface conditions. Especially for contemporary well-insulated constructions, where the heat fluxes are low but the exterior climate conditions vary greatly within short periods of time, it is the exterior surface microclimate which will define the deterioration of the building façade.

This paper suggests a simulation model for predicting the microclimatic surface conditions of building façades, which can later be used for predicting the deterioration course of building façades. HAM software tools, although sufficiently able to simulate the surface hygrothermal conditions, neglect the above mentioned microclimate and treat the whole façade as a uniform building envelope without considering the various façade details. The suggested model calculates the spatial variations of surface temperature and moisture content along

\* Corresponding author.

E-mail address: [stergiani.charisi@nmbu.no](mailto:stergiani.charisi@nmbu.no) (S. Charisi).



## Nomenclature

$T_w$	wall surface temperature [K]	$T$	air temperature [K]
$q_{wall}$	heat flux from the interior through the wall [ $W/m^2$ ]	$T_d$	dew point temperature [K]
$q_{stored}$	heat flux caused by heating or cooling the material in the wall [ $W/m^2$ ]	$R_{wdr}$	amount of wind-driven rain [mm]
$q_{rad}$	radiative heat flux from the surroundings [ $W/m^2$ ]	$C_R$	roughness coefficient [-]
$h$	local heat transfer coefficient [ $W/(m^2K)$ ]	$C_T$	topography coefficient [-]
$T_a$	temperature of the fluid close to surface [K]	$O$	obstruction factor [-]
$\Delta T_{wall}$	temperature difference between the wall ends [K]	$W$	wall factor [-]
$R_{wall}$	thermal resistance of the wall [ $(m^2K)/W$ ]	$R_{hor}$	rainfall intensity [mm/h]
$c$	specific heat capacity of the material [ $J/(kgK)$ ]	$U_{10}$	wind speed at 10 m height [m/s]
$m$	mass of the material [kg]	$\theta$	angle between wind direction and surface normal vector [°]
$dT_{t-wall}$	temperature difference of the material over specific time [K]	$G_t$	absorbed amount of water on surface [mm]
$t$	time step [s]	$a$	capillary water absorption coefficient [ $mm^3/(mm^2s^{0.5})$ ]
$A$	area of the material [ $m^2$ ]	$D$	moisture absorption coefficient [ $m^2/s$ ]
$\alpha$	absorption coefficient of the surface material	$S$	surface emission coefficient [m/s]
$q_{irrad}$	incident radiation on the surface [ $W/(m^2K)$ ]	$m_e$	equilibrium moisture content
		$m_{i,j}$	moisture content at thickness increment $i$ and time step $j$
		$\Delta t$	time step [s]
		$\Delta x$	thickness increment of surface material [m]

the façade by taking into account the building microclimate and its effect on crucial factors, such as solar radiation and wind-driven rain, and consequently on the hygrothermal conditions of the façade. This et al. have originally developed a model that can calculate surface temperatures and moisture content on the exterior surface of a wooden façade [14]. The model is based on the principles of one-dimensional heat and moisture transport and takes into consideration weather data, as well as the façade design, in order to predict spatial micro-scale variations of temperature and moisture along a building façade. The current paper, however, differentiates the way the surface moisture content is calculated, by introducing the moisture diffusion coefficient into the calculation process. Furthermore, in this study the model is validated through measurements for two different types of typical building façades. Subsequently, the suggested model is able to predict the spatial surface temperature and moisture content variations on a building façade, and can do this for various building materials.

## 2. Methodology

### 2.1. Suggested simulation model

A simple simulation model for calculating the external surface temperature and moisture content spatially throughout a whole façade was developed. A one-dimensional heat and moisture transport from external side to internal side in an opaque wall is assumed. The simulation model follows the physics explained analytically below and aims to calculate the local outer surface temperature and moisture content in a grid consisting of a thousand points on a façade. The model takes into consideration the microclimate in which the façade of interest is situated, and the properties of the building material used in the construction of the façade.

#### 2.1.1. Surface temperature

Fourier's law of heat conduction describes the heat transfer through a material [15,16]. The one-dimensional form of Fourier's law,  $q_x = -k \frac{dT}{dx}$ , is usually used to describe the heat flux in a material, where  $q_x$  [ $W/m^2$ ] is the heat flux in the  $x$  direction,  $k$  is the thermal conductivity of the corresponding material, and  $T$  its temperature. In numerical simulations of fluid and mass transfer, where it is necessary to define the surface temperature of a body, a special case of Fourier's law, called the Heat Flux Boundary Condition, is applied [15]. In the case of an external wall, the exterior surface temperature of the wall is given by the equation:

$$T_w = \frac{q_{wall} + q_{stored} - q_{rad}}{h} + T_a \quad (1)$$

In situations of little or no radiation from the surroundings, i.e. when the sun is down, the heat flux coming outdoors from the interior space and through the wall can be calculated by the equation:

$$q_{wall} = \frac{\Delta T_{wall}}{R_{wall}} \quad (2)$$

For a homogeneous wall of thickness  $L$ , its thermal resistance  $R_{wall}$  depends on the thermal conductivities  $\lambda$  of the materials used in the wall and their corresponding thicknesses [17]. It is strongly suggested that only design values of heat conductivity should be used, since they contain the contribution of a typical water content and are considered sufficient for hygrothermal simulations, and especially for this model that focuses on the external façade's diurnal surface conditions and not on the heat flows [18].

Contemporary buildings that are situated in cold climates are very well insulated and the one-dimensional heat flux through the envelope  $q_{wall}$  is expected to be in the order of 3–10  $W/m^2$ . During the hours of daylight that the sun is over the horizon, the solar irradiation is often in the magnitude of several hundred  $W/m^2$ . As a result, the  $q_{wall}$  can even be considered negligible during daytime.

Furthermore, the model does not consider thermal bridging effect. Thermal bridges are areas with higher heat flow that can result in significantly lower internal surface temperatures [19]. Linear thermal bridges on concrete or masonry buildings, but also point thermal bridges in lightweight ventilated façades, can significantly reduce the energy performance of a building [20–22]. However, thermal bridges are a dynamic multi-dimensional heat transfer phenomenon [23] that cannot be adequately approximated by the suggested one-dimensional model. In addition, thermal bridges are responsible for mould growth and interstitial condensation only on the internal surface of a building element [24], thus it is considered acceptable to neglect them since the current model focuses on the external surface microclimate conditions of a building.

Thermal energy can be stored as sensible heating in any material by raising its temperature. Sensible heat storage systems depend significantly on the specific heat capacity of their material [25]. The flux caused by thermal energy stored or extracted in a building material can be calculated based on the following equation:

$$q_{stored} = \frac{cm\Delta T_{t-wall}}{At} \quad (3)$$

The proposed model takes into consideration only the thermal

storage of the outermost material layer using the temperature difference between two consecutive time steps. The capacitive effect of the whole building element is neglected because both constructions examined have an air gap behind the cladding. As a result, the existing air gap, as a poor heat conductor, will obstruct and delay any heat released from the rest of the building envelope from reaching the cladding and vice versa [15]. Most contemporary constructions have a ventilated or stagnant air gap behind their main cladding, so the same simplification can be applied for various building elements.

Furthermore, it is known that the diurnal surface temperature and moisture fluctuations depend significantly on the atmospheric excitation [26]. As a result, the capacitive effect of the external layer of the building envelope has substantial impact on the diurnal surface temperature and moisture fluctuations within an hourly time step. On the other hand, the total thermal capacity of a well-insulated envelope can be considered negligible for such a short time interval, since the wall temperature does not change that rapidly.

Last but not least, the temperature of the exterior building surface is determined by the heat flow due to radiation exchange with the surroundings. The solar radiation is usually measured on meteorological stations. Considering no cloud coverage, solar radiation can be estimated based on the solar position, the latitude and longitude of the area of interest, and the atmospheric conditions. Meteorological stations usually measure the direct and diffuse radiation. The direct solar radiation on a building façade can be easily calculated using trigonometry and given the orientation and inclination of the façade. Only a fraction of the incident irradiation will be absorbed by the building surface and depends on the material absorptivity. The solar absorption coefficient of the external surface material should be chosen after careful research, as heat fluxes and surface temperatures strongly depend on it [27,28]. Consequently, the radiative heat flux on a building surface can be calculated with the following equation:

$$q_{rad} = \alpha q_{irrad} \quad (4)$$

The solar absorptivities of the two surface materials examined were determined at 0.63 and 0.82 for the aspen and the red fire clay brick correspondingly [29].

The long-wave radiation is neglected on the current model. Building components absorb long-wave radiation from the surroundings, while they also emit long-wave radiation back into their surroundings. Since all objects on the same area are considered to have quite similar temperatures based on the atmospheric conditions, this continuous long-wave radiation exchange is quite balanced and the exchanged radiation flow rather low [30,31].

Furthermore, the radiative cooling due to long-wave emission from the building surface into the dark sky at night time, or the cold ground, cannot be estimated due to lack of information regarding the cloud coverage and ground temperatures [30,31]. However, radiative cooling affects mostly horizontal surfaces, such as roofs, and surfaces that belong in building envelopes with low thermal inertia [30,31]. As a result, the neglectation of the long-wave radiation is a limitation of the suggested model, yet an acceptable simplification for the cases tested, since the model is suggested for well-insulated building wall elements.

### 2.1.2. Surface moisture and relative humidity (RH)

The relation between temperature, water content and RH is rather important for meteorological forecasting and has been previously studied [32]. The Clausius-Clapeyron equation characterizes the phase transition of water as temperature and pressure change. The August-Roche-Magnus approximation gives a good approximation of this equation [33], while Bolton [34] gives an accurate set of coefficients ( $b = 17.67$  and  $c = 243.5$ ) and the RH can be successfully predicted using the equation:

$$RH = 100 \frac{\exp\left(\frac{bT_d}{c+T_d}\right)}{\exp\left(\frac{bT}{c+T}\right)} \quad (5)$$

Furthermore, based on the same study, the dew point temperature is given by the equation:

$$T_d = \frac{c \left[ \ln\left(\frac{RH}{100}\right) + \frac{bT}{c+T} \right]}{b - \ln\left(\frac{RH}{100}\right) - \frac{bT}{c+T}} \quad (6)$$

It is possible to reliably assume that the air in the boundary layer close to the exterior surface of a wall has the same absolute water content as the ambient air, given that good mixing of air takes place in outdoor conditions. Given that the surface temperature of the exterior surface is varying according to equation (1), the RH in the boundary layer can be calculated by combining equations (5) and (6) by substituting ambient air temperature  $T_a$  for  $T$  in equation (6) and  $T_a$  for  $T$  in equation (5). As a result, the dew point  $T_d$  is calculated using the ambient air temperature  $T_a$ , and the RH close to the outer surface is calculated using the dew point and the modelled surface temperature from equation (1).

The moisture content of a material depends on the relative humidity and temperature of the air surrounding it. If the building material remains long enough in air where the RH and the temperature remain constant, the moisture content will also become constant at a value known as the equilibrium moisture content (EMC) [35]. The relation between RH in the surrounding air and EMC in porous materials is usually determined by a combination of diffusion and capillary transport tests in a controlled laboratory environment. A moisture sorption curve corresponds to every material and depicts the relationship between RH and EMC at a given temperature. It is known that the EMC increases with increasing relative humidity and with decreasing temperature [32].

Modelling of moisture content, especially in wood, can be performed with models with different complexity, and is a popular research topic. The two driving forces of moisture transport are diffusion and capillary flow [36]. The predominant moisture transport mechanism in porous materials is diffusion. However, in the context of building physics, it is sufficiently accurate to regard also the liquid transport in the pore spaces as a diffusion phenomenon.

The mathematics of diffusion offer a generalized system for predicting moisture content changes below the fiber saturation point. To use the mathematics of diffusion, it is necessary to know the diffusion coefficient and the factors that cause it to vary [37,38]. Diffusion describes the movement of water between the interior and the surface of the porous material. Internal resistance to moisture movement is characterized by the diffusion coefficient  $D$ , which depends on several factors including moisture content and temperature, and is a unique characteristic of every material. Simpson et al. [37] highlight that movement of water across the surface of the material is also a factor in determining the rate of water adsorption or desorption, and subsequently the moisture content of the material. This surface resistance to moisture movement can be described by the surface emission coefficient  $S$ , which depends on temperature, air velocity, and relative humidity.

Liu [39] has developed an equation that separates the diffusion coefficient  $D$  from the surface emission coefficient  $S$ , and the surface emission coefficient is given by the equation:

$$S = \frac{0.701D}{\left(\frac{a}{2}\right) \left[ \frac{D}{\left(\frac{a}{2}\right)^2} - 0.196 \right]} \quad (7)$$

Crank [40] gives the equation for calculating the surface moisture content  $m_0$ :

$$m_{0,j+1} = m_{0,j} + 2RD_{0,j} \left[ m_{1,j} - m_{0,j} - \left( \frac{S}{D} \right) \Delta x (m_{0,j} - m_e) \right] \quad (8)$$

where  $R = \Delta t / (\Delta x)^2$ .

The indexing system is  $m_{i,j}$ , where  $i$  is  $x$  (thickness) increment and  $j$  is  $t$  (time) increment. In the calculation model, the assumption that  $m_{1,j}$  is equal to  $m_{0,j}$  has been made, due to the material thickness used for calculating the exterior surface moisture content being extremely small, and the difference is considered negligible.

The simulation model uses equations (1)–(4) in order to calculate the exterior surface temperatures. The specific heat capacity, absorption coefficient and interior temperature are set according to the façade material and construction type correspondingly.

The model also requires the solar radiation on the façade in time and space. The software tool RADIANCE has been developed to simulate the radiation in illuminated spaces [41]. It uses the technique of ray-tracing, which follows light backwards from the image plane to the source. RADIANCE and another daylight simulation engine, DAYSIM [42], have been incorporated to the software DIVA-for-Rhino. The software has been used to calculate climate-specific hourly irradiation load at nodes located on the façade of a 3D digital building model. The software uses EnergyPlusWeather (.epw) files that provide hourly weather data. Using a relatively dense simulation grid with node distance approximately at 8 cm makes it possible to simulate the shading effects of small building features, such as window sills and overhangs, as well as larger effects, such as shading roof eaves and inside corners. The software calculates the hourly solar irradiation in every node for one whole year given the climate, the geographic position, the architecture and the orientation of the building. The irradiation load for every node is corrected with the absorption coefficient of the façade material. The grid generated by the software is further used for calculating the exterior surface temperature and moisture content on every node, thus getting spatial results on the façade.

After the exterior surface temperature is calculated, the dew point  $T_d$  and the RH close to the outer surface are calculated by equations (5) and (6) as has been described above.

Subsequently, the moisture content on the outdoor façade surface is calculated by equation (8). For every material, its diffusion coefficient needs to be defined. As has already been mentioned, diffusion coefficient is strongly dependent on moisture content and temperature [35]. For the simulation model, diffusion coefficients available in literature were used for the tested materials [37,40]. For relative low levels of moisture content from 10% to 50% most of diffusion coefficients seem to increase slightly and linearly, so the average diffusion coefficient was used for calculating the moisture content. Diffusion coefficients change radically for high levels of moisture content during capillary uptake. This feature was implemented at the simulation model, and the diffusion coefficient taken into consideration at moisture content levels higher than 80% represents the capillary diffusion coefficient of each material. In each time step, the surface emission coefficient of the material is computed by equation (7) and depends on the diffusion coefficient selected.

In addition to the hygrothermal atmospheric conditions, the surface moisture content of building cladding is significantly affected by wind-driven rain. The relation between wind-driven rain and its impact on the hygrothermal conditions of a façade has been extensively studied [43–45]. Blocken and Carmeliet have performed a thorough literature review regarding the various methods used to define the wind-driven loads on building façades [46]. In this paper, the effect of the driving rain on the surface moisture content is quantified and counted in the calculation of the total surface moisture content. The wind-driven rain load of the building façade is determined based on the semi-empirical model proposed by the International Standard for hygrothermal performance of buildings [47]. The amount of wind-driven rain, according to standard ISO 15927–3:2009, is calculated by the following equation:

$$R_{wdr} = \frac{2}{9} C_r C_T OWU_{10} R_{hor}^{0.88} \cos \vartheta \quad (9)$$

The wall factor  $W$  is defined as the ratio of the quantity of water hitting a wall to the quantity passing through an equivalent unobstructed space, allowing thus to account for the spatial characteristics of the wall, such as window-sills, overhangs or extrusions. The amount of rain incident on a wall depends on the type of the wall, its height and on the construction characteristics of the façade and the roof. Furthermore, the amount of impinging rain can vary significantly over a building surface according to the air flow around the building [47]. An important limitation of the standard is that the wall factor is given for a limited number of building configurations and disregards potential spatial characteristics of the façade. As a result, microscale effects, such as sheltering due to overhangs and extrusions, are not imported into the calculation of the amount of driving rain hitting a façade.

Tsoka and Thisis suggest a new model for calculating a set of wall factor coefficients that can sufficiently capture the microscale effects along a façade due to its unique characteristics [48]. The method is based on the ray tracing method that is widely used for determining solar radiation effects on building façades. The model treats the rain droplet trajectories as straight paths, similarly to solar beams. It calculates the impact of the driving rain on the façade for two wind speeds ( $U < 4$  m/s and  $U > 4$  m/s) and for eight different wind directions (N, NE, E, SE, S, SW, W, NW). The 32 masks resulting are consequently combined with the wall factor provided by the ISO standard, thus creating a set of new wall factors based on the specific characteristics of the façade. These building-specific wall factors can sufficiently capture the microscale effects of the building. The building-specific wall factor for the wooden façade is presented in Fig. 1. The amount of wind-driven rain hitting the building façade is calculated based on the new building-specific wall factors.

Furthermore, it is known that only a part of the driving rain that impacts on the wall will be absorbed by the surface and the rest will run off [46,49]. Beijer [50] introduced a simple model for determining the absorbed amount of water and is given by the equation:

$$G_r = \min \left\{ \frac{R_{wdr}}{a \cdot \sqrt{t}} \right\} \quad (10)$$

where the capillary absorption coefficient  $a$  is set to 0.007. Once the amount of the absorbed water has been defined, it is then divided by the width of the material cladding and is added to equation (8) to determine the final surface moisture content MC. The model procedure is presented briefly on the following flow chart (Fig. 2), where the rectangular shapes represent input for the model and the oval shapes represent calculated values.

## 2.2. Simulations

The above model was applied for two different façades. The first is a wooden façade consisting of aspen (*populus tremula*) panels. The cladding has a thickness of 30 mm and behind it there is a layer of stagnant air. The second façade consists of red clay fire bricks. The bricks have a typical thickness of 80 mm and they are placed as exterior cladding to a masonry wall. The two façades are shown in Fig. 3.

The simulation model is set to run with an hourly time step for a

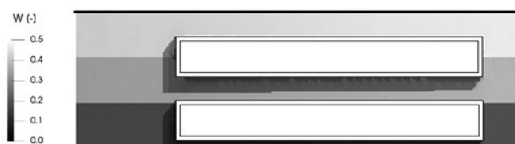
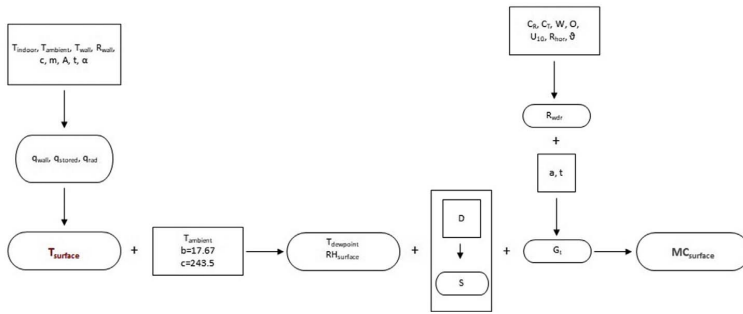


Fig. 1. Building-specific wall factor for a building façade with two extruded windows.

Fig. 2. Flow chart explaining the model developed.



period of a whole year. The climate data used were retrieved from a local meteorological station situated approximately 0.5–1 km from the buildings, so they sufficiently represent the microclimate of the area. Both buildings are rather exposed. The grids that were created for both buildings consist of nodes that abstain 8 cm from each other. The grid for the wooden and the masonry façade include 21450 and 5896 nodes respectively. It is reminded that the weather data that are needed as input parameters to the proposed model are ambient air temperature, ambient RH and solar radiation. Furthermore, the model requires the properties of the surface material, such as adsorption coefficient, surface transfer coefficient, diffusion coefficient and moisture storage curve.

### 2.3. Measurements

The surface temperatures were monitored in both façades for a certain period of time. The moisture content of the wooden cladding was also measured using resistance humidity sensors. Due to limited allowed access on the building site, it was not possible to perform moisture measurements in the brick façade. The measurements obtained were used for validating the simulation model. For further validation, the model's results were compared to software WUFI [51], which is one of the most commonly used hygrothermal analysis software tools and has already been validated by several reports [52,53].

In both façades, the surface temperatures were monitored using thermography techniques. An Optris PL640 camera, that delivers radiometric pictures, was used to obtain the spatial distribution of the



Fig. 3. Pictures of the (a) wooden façade and (b) masonry façade. The red and black points represent the positions of the sensors (T and RH). (For interpretation of the references to colour in this figure legend, the reader is referred to the web version of this article.)

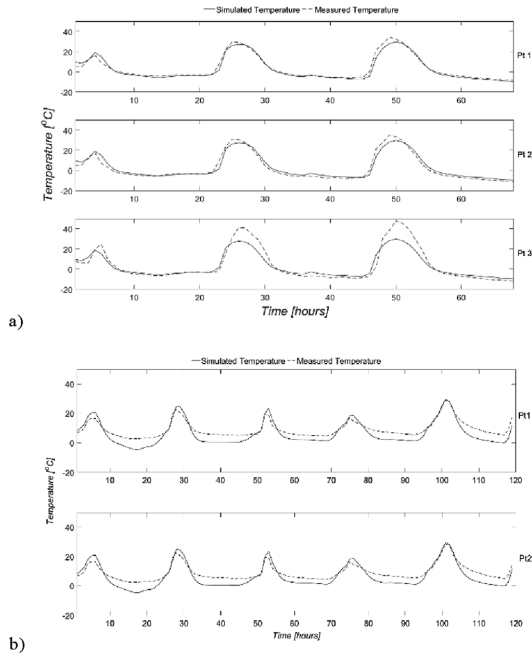


Fig. 4. Simulated and measured temperatures for (a) untreated wooden façade; (b) masonry façade.

surface temperature over the building façades. In both cases, the IR camera was mounted on the rooftop of a neighbouring building. The monitoring time for the wooden façade was approximately a week, whereas for the masonry façade was ten days.

Furthermore, temperature sensors were installed on the façades of the buildings (Fig. 3). The temperature sensors were installed inside holes that were drilled very close to the surface of the façades, approximately 3 mm behind the surface. The temperature sensors are considered accurate with a very small margin of error, and therefore their data were used in order to calibrate the IR camera.

The emissivities of the surface building materials of the monitored buildings were unknown before the measurements. During the thermal camera recording, the emissivity of the surface material was set at 1. As a result, the surface temperatures deriving from the thermal camera had an offset of the actual values of the surface temperatures. The correct emissivity values of the building materials were mathematically calculated based on the camera's measurement formula. The measurement formula of the camera is based on the Stefan-Boltzmann law, that describes the total emissive power of a blackbody as being proportional to the fourth power of its absolute temperature. During the measurements, the infrared camera not only receives radiation from the object, but also collects radiation from the surroundings, as well as the atmosphere itself [54]. The raw data obtained from the camera were used to calculate the total received radiation power. Knowing the total received radiation power from the camera, and the surface temperatures from the attached sensors, the emissivity of the aspen and the red fire clay brick were calculated to be  $\epsilon = 0.87$  and  $\epsilon = 0.93$  respectively. The surface temperatures obtained by the infrared camera were corrected for the right emissivity of the materials.

In addition to the temperature sensors, moisture sensors were also attached to the wooden building façade. The wood resistance humidity sensors were installed on the front side of the wood façade using metal spikes. Field results have already shown that this kind of sensor shows

rather good reliability and performance in exterior environments, and are reliable for building enclosure monitor applications [55]. Unfortunately, due to restricted access, the available humidity sensors were not able to be mounted on the brick façade.

The thermography measurements were used to validate the developed model for surface temperature, while the humidity measurements were used to validate the model for the moisture content. Since humidity measurements are not available for both building façades, the model was additionally validated for the moisture content based on simulation results deriving from the hygrothermal analysis tool WUFI.

### 3. Results

For the validation of the model, the simulation results for the surface temperature are compared to the measurements performed with the infrared camera on building site. As far as the moisture content is concerned, the simulated results are compared to the recording of the humidity sensors installed on the wooden façade. Since for the masonry façade such humidity measurements are not available, the simulation results are compared to simulation results deriving from WUFI. Simulation results from the software for the wooden façade are also compared to the measurements performed on the wooden façade in order to justify the reliability of the software and accept it as credible reference.

The root mean square error (RMSE) is used as a measure of the model performance. The RMSE is calculated for the data set based on the following formula:

$$RMSE = \sqrt{\frac{1}{n} \sum_{i=1}^n \Delta T^2} \quad (11)$$

where  $n$  is the overall time steps during which the value of interest (surface temperature or moisture content) were calculated, and  $\Delta T$  is the value difference between the measurements and the simulation model. The RMSE is considered appropriate measure index to express the accuracy of the predicted model surface conditions and has already been used in similar studies [56].

#### 3.1. Surface temperature

Initially, the simulated temperatures derived from the model are compared to the temperatures measured by the temperature loggers. The positions of the sensors on the building façades are known, and the correct points of the grid in the model, corresponding to these positions, are used. Fig. 4 shows the measured and simulated diurnal variation of temperature. Three sensors were placed on the wooden façade, whereas only two were placed on the masonry wall. The sensors were monitoring for 70 and 120 h respectively. The errors for the simulated temperatures compared to the measurements for both buildings are given in Table 1. In both cases, the error maximizes for the point that is close to window sill for the wooden surface and metal overhang for the brick façade. The model does not include either the metal sheeting or the convective heat transfer from the window's sill. Consequently, the error can potentially be the result of the simplification of the setup.

Fig. 5a shows the spatial distribution of the RMSE of the simulated surface temperatures compared to the IR measurements for the wooden façade. Since the view field of the camera is limited, the camera

Table 1

Root mean square error (RMSE) of the simulation compared to the measurements on the positions of the sensors.

	Untreated wooden façade	Masonry façade
Pt1	2.21	4.12
Pt2	2.79	3.98
Pt3	6.03	

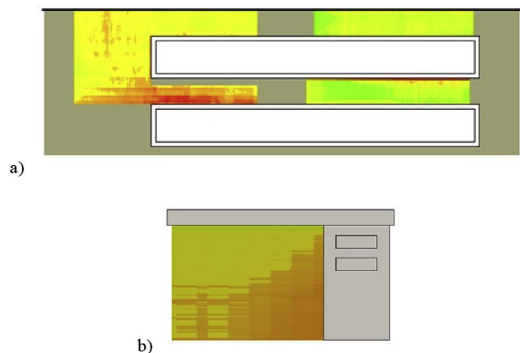


Fig. 5. RMSE of the simulations compared to the IR measurements for (a) untreated wood façade and (b) masonry façade.

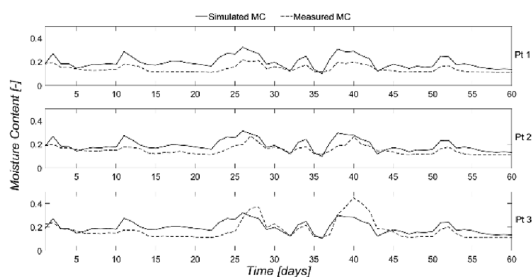


Fig. 6. Simulated and measured moisture content on untreated wooden façade.

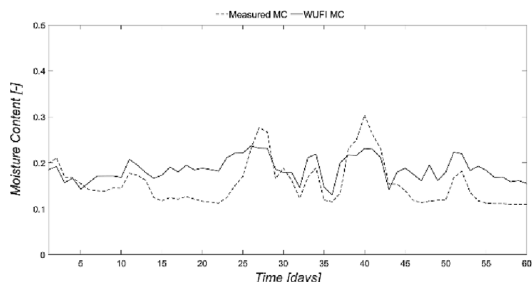


Fig. 7. Measured moisture content using the available sensors and simulated moisture content by software WUFI on untreated wooden façade.

recorded separately two different areas of the façade. The camera was monitoring the right side of the south facing façade for 72 consecutive hours and the left side of the façade for the next 48 h. The two recording episodes were timely close, but during the recording of the right side the ambient temperature was significantly lower. The increment of the ambient temperature is expected to raise the magnitude of surface temperatures observed and as a result increase the error between the simulations and the measurements. The area with the highest error is detected on the lower left side of the building, where a neighbouring tree casts its shadow. The tree is not allowed for during the simulations, and the shadow it casts on the building during daytime is responsible for the rather large error. Furthermore, the neighbouring building itself contributes to the error. Although the neighbouring building is simulated, the timing of its shadow is slightly out of synchronization with

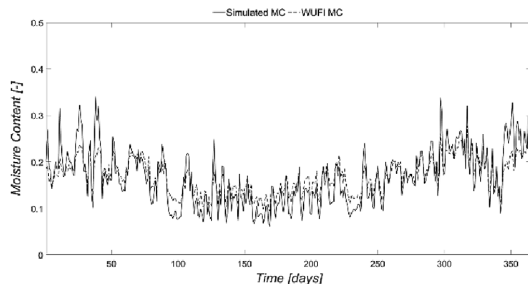


Fig. 8. Simulated moisture content using the developed model and software WUFI on brick façade.



Fig. 9. Spatial simulation of yearly mean surface temperature on untreated wooden façade.



Fig. 10. Spatial simulation of yearly mean moisture content on untreated wooden façade.

the measurements, resulting in a larger error.

Fig. 5b presents the spatial distribution of the RMSE of the simulated surface temperatures compared to the IR measurements for the masonry façade. The monitoring took place in late summer and lasted 300 h. As it is obvious, the spatial error is quite uniform along the façade, approximately at 5 °C, which is considered within acceptable range since the magnitude of the surface temperatures at summer time rises over 50 °C. According to the manufacturer, the IR camera gives a temperature error of  $\pm 2$  °C for the same temperature range. Furthermore, for every point in the façade, the coefficient of variation (CV), which is defined as the ratio of the standard deviation  $\sigma$  to the measured mean  $\mu$ , and shows the extent of the variability in relation to the actual mean of the population, is calculated. Similarly, the spatial distribution of the CV of all the simulated point temperatures fluctuates around 3.3 over time. According to the spatial plot, the error rises significantly on the right edge of the façade, which is located right next to a metal door. The metal door is not taken into consideration in the simulation model, and the heat flux of the metal material is not reflected in the simulation results, causing the error to increase in the area adjacent to the metal door.

### 3.2. Moisture content

As far as the moisture content is concerned, the measured data from the wooden façade are compared to the simulation results and are shown in Fig. 6. For all three points available, the RMSE of moisture error fluctuates around 0.05, which is within acceptable range. The measured data from the humidity sensors are additionally compared to the simulated moisture content derived from one of the most commonly used software WUFI (Fig. 7) and the corresponding RMSE is calculated

equal to 0.053. This is similar to the RMSE deriving from the comparison between the developed model and the measurements. This comparison proves that the simple simulation model developed produces quite reliable results, in line with those of the state-of-the-art software. Furthermore, it should be highlighted that besides the simulation error, an error due to hypersensitivity of the resistance humidity sensors to impinging water also supersedes into the comparison [55].

Due to lack of humidity measurements for the brick façade, the simulated results for moisture content from the developed model is compared to the WUFI results, whose accuracy has already been established above. Fig. 8 shows that developed model produces results similar to advanced software tool WUFI with only 0.0067 of RMSE.

#### 4. Discussion

A model that can predict the spatial diurnal variations for external surface temperature and moisture content has been developed. The model is based on one-dimensional heat and moisture transport from external to internal side and has been developed for opaque (homogenised) building materials. The model does not account for long-wave radiation and thermal bridging effect, because it focuses on the hygrothermal conditions of the external surface. Solar radiation and wind-driven rain are considered the driving mechanisms affecting surface temperatures and moisture content on a façade, and they have been integrated on the model so as to be able to predict their spatial effect on a façade.

Figs. 9 and 10 present the mean surface temperatures and moisture content respectively, for a time period of a year on the wooden façade. The model is able to capture the spatial variations of surface temperature and moisture content in a building façade.

The effect of solar radiation on the surface temperatures and the impact of wind-driven rain on surface moisture content is obvious. As expected, the areas of the building that are mostly exposed to short-wave radiation present high surface temperatures due to the high radiative flux that is introduced to the building façade. Furthermore, moisture transport is treated as a combination of diffusion phenomenon for humidity levels lower than 80% and capillary phenomenon for higher humidity levels. As further expected, especially for cold climates with high precipitation, the model captures the significant impact of impinging water on the surface. Sheltered areas of the building façade will maintain lower moisture content, while the higher and more exposed parts of the building to driving rain will present the highest levels of surface moisture content.

#### 5. Conclusion

This paper presents a one-dimensional model that predicts spatial microclimate surface conditions on a building façade. Despite the limitations of the model, the measurements indicate that it can perform on an external surface with high spatial accuracy. The simulation model is able to capture sufficiently the surface temperature and moisture content variations on a façade and, given the amplitude of the variables, the error of the simulation is considerably low. Measurements in two different kind of façades suggest that the model can perform equally well for different façade materials. For higher accuracy of results, the model should adopt more extreme detail in the geometrical modelling and neighbouring obstacles.

The model's main advantage is that it provides a spatial illustration of the façade's surface hygrothermal conditions with high accuracy. At the same time, the external surface temperature and moisture content of a façade are also calculated with high arithmetic accuracy. As a result, the model can point out high-risk areas with hygrothermal conditions that can encourage potential mould growth, deterioration and discoloration of the façade material. These areas would not be possible to be captured by conventional hygrothermal models that treat the whole building envelope uniformly.

The suggested model consists of a fast and user-friendly tool for simulating the microclimatic spatial conditions of a building façade. If the model is combined with mould-growth or decay models, such as Thelander and Isaksson [5], it can be useful as decision support for façade material by architects and engineers.

#### Acknowledgement

This work has been funded by the Norwegian Research Council as part of the project 'WOOD/BE/BETTER' code 225345.

#### References

- [1] K. Sedlbauer, Prediction of mould growth by hygrothermal calculation, *J. Therm. Envelope Build. Sci.* 25 (2002) 321–336.
- [2] W.C. Feist, Outdoor wood weathering and protection, *Adv. Chem.* 225 (11) (1989) 263–298.
- [3] K.R. Lisø, T. Kvanne, H.O. Hygen, J.V. Thue, K. Harstvein, A frost decay exposure index for porous, mineral building materials, *Build. Environ.* 42 (2007) 3547–3555.
- [4] A. Hukka, H.A. Viitanen, A mathematical model of mould growth on wooden material, *Wood Sci. Technol.* 33 (1999) 475–485.
- [5] S. Thelander, T. Isaksson, Mould resistance design (MRD) model for evaluation of risk for microbial growth under varying climate conditions, *Build. Environ.* 65 (2013) 18–25.
- [6] P. Johansson, G. Bok, A. Ekstrand-Tobin, The effect of cyclic moisture and temperature on mould growth compared to steady state conditions, *Build. Environ.* 65 (2013) 178–184.
- [7] P. Johansson, T. Svensson, A. Ekstrand-Tobin, Validation of critical moisture conditions for mould growth on building materials, *Build. Environ.* 62 (2013) 201–209.
- [8] K.F. Nielsen, G. Holm, L.P. Uttrup, P.A. Nielsen, Mould growth on building materials under low water activities. Influence of humidity and temperature on fungal growth and secondary metabolism, *Int. Biodeterior. Biodegrad.* 54 (2004) 325–336.
- [9] A.L. Pasanen, J.P. Kasanen, S. Rautiala, M. Ikaheimo, J. Rantamaki, H. Kaariainen, P. Kallioikoski, Fungal growth and survival in building materials under fluctuating moisture and temperature conditions, *Int. Biodeterior. Biodegrad.* 46 (2000) 117–127.
- [10] K. Gobakis, D. Kolokotsa, Coupling Building Energy Simulation Software with Microclimatic Simulation for the Evaluation of the Impact of Urban Outdoor Conditions on the Energy Consumption and Indoor Environmental Quality. *Energy and Building*, Article in Press, 2017.
- [11] A. Gros, E. Bozonnet, C. Inard, Cool materials impact at district scale – coupling building energy and microclimate models, *Sustain. Cities Soc.* 13 (2014) 254–266.
- [12] A. Gros, E. Bozonnet, C. Inard, M. Musy, Simulation tools to assess microclimate and building energy – a case study on the design of a new district, *Energy Build.* 114 (2016) 112–122.
- [13] S. Tsoka, K. Tsikaloudaki, T. Theodosiou, Urban space's morphology and micro-climatic analysis: A study for a typical urban district in the Mediterranean city of Thessaloniki, Greece, *Energy Build.* 156 (2017) 96–108.
- [14] T.K. Thisi, I. Burud, A. Flø, D. Kraniotis, S. Charisi, P. Stefansson, Monitoring and simulation of diurnal surface conditions of a wooden façade, *Procedia Environ. Sci.* 38 (2017) 331–339.
- [15] T.L. Bergman, A.S. Lavine, F.P. Incropera, D.P. Dewitt, *Fundamentals of Heat and Mass Transfer*, seventh ed., John Wiley and Sons Ltd, 2012.
- [16] T.N. Narasimhan, Fourier's heat conduction equation: history, influence, and connections, *Rev. Geophys.* 37 (1999) 151–172.
- [17] J. Sykora, J. Vorel, T. Krejci, M. Sejnoha, J. Sejnoha, Analysis of coupled heat and moisture transfer in masonry structures, *Mater. Struct.* 42 (2009) 1153–1167.
- [18] H.M. Kunzel, Simultaneous Heat and Moisture Transport in Building Components – One- and Two-dimensional Calculation Using Simple Parameters, IRB Verlag, 1995.
- [19] International Organization for Standardization, ISO 10211, Thermal Bridges in Building Construction – Heat Flows and Surface Temperatures – Detailed Calculations, (2007).
- [20] A.B. Larbi, Statistical modelling of heat transfer for thermal bridges of buildings, *Energy Build.* 37 (9) (2005) 945–991.
- [21] K. Tsikaloudaki, T. Theodosiou, D. Aravantinos, K.N. Kontoleon, D. Bikas, Quantifying the thermal bridging effect with regard to the facade's configuration, *Proc. Int. Acad. Conf. Places Technologies* (2014) 570–576.
- [22] T.G. Theodosiou, A.G. Tsikaloudaki, K.J. Kontoleon, Thermal bridging analysis on cladding systems for building facades, *Energy Build.* 109 (2015) 377–384.
- [23] A. Tadeu, I. Simoes, N. Simoes, J. Prata, Simulation of dynamic linear thermal bridges using a boundary element method model in the frequency domain, *Energy Build.* 43 (2011) 3685–3695.
- [24] International Organization for Standardization, ISO 13788, Hygrothermal Performance of Building Components and Building Elements – Internal Surface Temperature to Avoid Critical Surface Humidity and Interstitial Condensation – Calculation Methods, (2001).
- [25] O. Ercan Ataer, Storage of Thermal Energy - Energy Storage Systems in Encyclopedia of Life Support Systems (EOLSS). Developed under the Auspices of the UNESCO, Eolss Publishers, 2006.
- [26] H. Janssen, B. Blocken, J. Carmeliet, Conservative modelling of the moisture and heat transfer in building components under atmospheric excitation, *Int. J. Heat Mass Transf.* 50 (2007) 1128–1140.

- [27] K.J. Kontoleon, D.K. Bikas, The effect of south wall's outdoor absorption coefficient on time lag, decrement factor and temperature variations, *Energy Build.* 39 (2007) 1011–1018.
- [28] D. Mazzeo, G. Oliveti, N. Arcuri, Mapping of the seasonal dynamic properties of building walls in actual periodic conditions and effects produced by solar radiation incident on the outer and inner surfaces of the wall, *Appl. Therm. Eng.* 102 (2016) 1157–1174.
- [29] J.L.M. Hensen, R. Lamberts, *Building Performance Simulation for Design and Operation*, first ed., Spon Press, 2011.
- [30] VDI 3789, Wechselwirkungen zwischen Atmosphäre und Oberflächen; Berechnung der kurz- und der langwelligen Strahlung, *Umweltmeteorologie*, Bl. 2 (1992).
- [31] M. Kehler, T. Schmidt, Temperaturverhältnisse an Aussenoberflächen unter Strahlungseinflüssen, *Proceedings BauSIM 2006*, 2006.
- [32] M.G. Lawrence, The relationship between relative humidity and the dewpoint temperature in moist air: a simple conversion and applications, *Bull. Am. Meteorological Soc.* 86 (2) (2005) 225.
- [33] D. Koutsoyiannis, Clausius-Clapeyron equation and saturation vapour pressure: simple theory reconciled with practice, *Eur. J. Phys.* 33 (2) (2012) 295.
- [34] D. Bolton, The computation of equivalent potential temperature, *Mon. Weather Rev.* 108 (1980) 1046–1053.
- [35] W.T. Simpson, Determination and use of moisture diffusion coefficient to characterize drying of northern red oak (*Quercus rubra*), *Wood Sci. Technol.* 27 (1993) 409–420.
- [36] H.M. Kunzel, K. Kiessl, Calculation of heat and moisture transfer in exposed building components, *Int. J. Heat Mass Transf.* 40 (1997) 159–167.
- [37] W.T. Simpson, J.Y. Liu, Dependence of the water vapour diffusion coefficient of aspen (*Populus spec.*) on moisture content, *Wood Sci. Technol.* 26 (1991) 9–21.
- [38] R. Sargent, S. Riley, L. Schottle, Measurement of dynamic sorption behaviour of small specimens of *Pinus Radiata* – influence of wood type and moisture content of diffusion rate, *Cienc. Technologia* 12 (2010) 93–103.
- [39] J.Y. Liu, A new method for separating diffusion coefficient and surface emission coefficient, *Wood Fiber Sci.* 21 (1989) 133–141.
- [40] J. Crank, *The Mathematics of Diffusion*, second ed., Oxford University Press, 1975.
- [41] K. Frost, M. Donn, R. Amor, The application of RADIANCE to daylighting simulation, *Proceedings of Building Simulation '93*, Adelaide, Australia, 16–18 August, 1993.
- [42] C.F. Reinhart, O. Walkenhorst, Validation of dynamic RADIANCE-based daylight simulations for a test office with external blinds, *Energy Build.* 33 (2001) 683–697.
- [43] A. Kubilay, D. Derome, B. Blocken, J. Carmeliet, Numerical simulations of wind-driven rain on an array of low-rise cubic buildings and validation by field measurements, *Build. Environ.* 81 (2014) 283–295.
- [44] A. Karagiozis, G. Hadjisophocleous, S. Cao, Wind-driven rain distributions on two buildings, *J. Wind Eng. Industrial Aerodynamics* 67 (1997) 559–572.
- [45] M. Abuku, H. Janssen, S. Roels, Impact of wind-driven rain on historic brick wall buildings in a moderately cold and humid climate: numerical analyses of mould growth risk, indoor climate and energy consumption, *Energy Build.* 41 (2009) 101–110.
- [46] B. Blocken, J. Carmeliet, A review of wind-driven rain research in building science, *J. Wind Eng. Industrial Aerodynamics* 92 (2004) 1079–1130.
- [47] International Organization for Standardization, ISO 15927-3, Calculation of a Driving Rain Index for Vertical Surfaces from Hourly Wind and Rain Data, (2009).
- [48] S. Tsoka, T.K. This, Calculation of the driving rain wall factor using ray-tracing, 7th European-african Conference on Wind Engineering, Liege, Belgium, 4–7 July, 2017.
- [49] B. Blocken, D. Derome, J. Carmeliet, Rainwater runoff from building façades: a review, *Build. Environ.* 60 (2013) 339–361.
- [50] O. Beijer, Concrete walls and weathering, RILEM/ASTM/CIB Symposium on Evaluation of the Performance of External Vertical Surfaces of Buildings, Otaniemi, Espoo, Finland, 23–31 August & 1–2 September, 1977.
- [51] A. Karagiozis, H.M. Kunzel, A. Holm, WUFI-ORNL/IBP – a North American hygrothermal model, *Performance of Exterior Envelopes of Whole Buildings VIII*, 2001, pp. 2–7.
- [52] M. Krus, H.M. Kunzel, M. Hartwig, Vergleich experimenteller und rechnerischer Ergebnisse anhand des Austrocknungsverhaltens von Ziegelwänden, *Tagungsbericht des Internationalen CIB W67 1996* (1996), pp. 433–498.
- [53] M.P. Solof, A. Jesper, Comparison of field measurements and calculations of relative humidity and temperature in wood framed walls, *Conf. Proc. – Thermophys.* 2010 (2010) 93–101.
- [54] Flir, *Flir Tools: User's Manual*, (2011) Publ. No. T559600.
- [55] U. Köhta, J. Straube, Laboratory calibration and field results of wood resistance humidity sensors, *BEST 1: Building for Energy Efficiency and Durability at the Crossroads*, Minneapolis, MN, 2008.
- [56] T. Chai, R.R. Draxler, Root mean square error (RMSE) or mean absolute error (MAE)? – Arguments against avoiding RMSE in the literature, *Geosci. Model Dev.* 7 (2014) 1247–1250.



Paper II



Available online at [www.sciencedirect.com](http://www.sciencedirect.com)

**ScienceDirect**

Energy Procedia 122 (2017) 637–642

Energy

**Procedia**

[www.elsevier.com/locate/procedia](http://www.elsevier.com/locate/procedia)

CISBAT 2017 International Conference – Future Buildings & Districts – Energy Efficiency from Nano to Urban Scale, CISBAT 2017 6-8 September 2017, Lausanne, Switzerland

**Sustainable Building Envelopes (Ecobuildings, Retrofit, Performance Gap)**

## Investigation of the pressure coefficient impact on the air infiltration in buildings with respect to microclimate

Stergiani Charisi<sup>a,\*</sup>, Milosz Waszczuk<sup>a</sup>, Thomas K. Thiis<sup>a</sup>

<sup>a</sup>*Faculty of Science and Technology, P.O. Box 5003, 1432 Ås, Norway*

---

### Abstract

Wind pressure coefficients ( $C_p$ ) are important for calculating the air infiltration rate of a building.  $C_p$  depend on a wide range of parameters, such as wind direction and speed, position on the building surface and façade exposure. Most Building Energy Simulation (BES) programs generally calculate air infiltration using simplified pressure coefficients. The Norwegian technical software (SIMIEN) do not consider them. The effect of the pressure coefficients on the air infiltration of the building, taking into consideration the microclimate of the building area, is studied. The wind pressure coefficients are defined through computational fluid dynamics (CFD) simulations. The air infiltration in the building is determined based on the calculated pressure coefficients. Tracer gas measurements were used for validation of the results. Two cases of fully exposed and partially sheltered building were examined. The results indicate that wind pressure coefficients derived from CFD simulations calculate more realistic values for the air infiltration of the building.

© 2017 The Authors. Published by Elsevier Ltd.

Peer-review under responsibility of the scientific committee of the CISBAT 2017 International Conference – Future Buildings & Districts – Energy Efficiency from Nano to Urban Scale

*Keywords: wind pressure coefficient, CFD, microclimate, air infiltration, simulation*

---

---

\* Corresponding author. Tel.: +47-942-78-276.

E-mail address: [stergiani.charisi@nmbu.no](mailto:stergiani.charisi@nmbu.no)

## 1. Introduction

Air infiltration is one of the most important factors with respect to energy use of buildings. Infiltration strongly depends on wind and air buoyancy forces. Mathematically, the volumetric flow rate of outside air entering the building is a function of pressure difference on the building envelope. When wind impinges on the surface of a building, a positive pressure is induced on the upwind face. This wind pressure is usually expressed by pressure coefficients ( $C_p$ ), which depend on a wide range of parameters, such as wind direction and speed, position on the building surface and façade exposure.

Wind pressure coefficients ( $C_p$ ) are defined as the ratio between the wind-induced pressure in a point  $x$  in the building façade  $P_x$ , and the dynamic wind pressure in the free stream region  $P_d$  [1].

$$C_p = \frac{P_x}{P_d} \quad (1)$$

The dynamic wind pressure corresponds to the force per are unit due to wind inertia, given by the following equation, where  $U_{ref}$  is the wind speed (m/s) at the building height, and  $\rho$  is the air specific mass ( $\text{kg/m}^3$ ) [1].

$$P_d = \frac{\rho \cdot U_{ref}^2}{2} \quad (2)$$

The Norwegian national standard for calculation of energy performance of buildings (NS 3031) neglects completely the wind pressure coefficients during the calculation of air infiltration, introducing thus a large error in the estimation of energy use of buildings. Most commercial Building Energy Simulation (BES) programs calculate air infiltration using simplified pressure coefficients given by standard datasets or analytical models. The field of computational fluid dynamics (CFD) regarding air flow around buildings and wind pressure on building façade has been constantly evolving the past 30 years. Nowadays, CFD simulations are considered as an accurate and reliable method to model wind flow around building [2]. Costola et al. showed that the  $C_p$  values differentiate significantly depending on the source adopted and highlights the superiority of CFD simulations over the rest of the sources.

Furthermore, several authors have studied the microclimate effect on energy balance of buildings and it has been established that the surrounding microclimate of a building plays a decisive role in its energy balance [3]. Despite this fact, almost all BES programs use typical meteorological year (TMY) climate and tend to ignore that microclimate can vary significantly within the borders of the same geographical area, according to urban infrastructure and architectural details. Microclimate can also influence the wind pressure coefficient, which depends on a set of local climatic parameters, such as wind speed and direction, as well as on the building construction and surroundings. As a result, the local microclimate of a building can be introduced by firstly using actual weather data of the site examined, and secondly by using more detailed  $C_p$  values that reflect the impact of all the above dependent variables.

## 2. Methodology

In this study, the impact of pressure coefficients  $C_p$  on the infiltration rate of buildings with respect to the local microclimate was investigated. Three different approaches, regarding the wind pressure coefficients, were implemented in order to determine the infiltration rate. Tracer gas measurements were performed at a reference building and were used to evaluate the impact of pressure coefficients on the total infiltration of the building. During all the phases of the study, the actual weather data of the building site were used.

### 2.1. Reference building

A building that was available for measurements was selected as the reference building for this study. The building has south orientation and is a fully exposed building in an open terrain [Figure 1]. All the actual weather data used for the later simulations were collected 10 meters outside the building. The reference building does not have mechanical ventilation system.

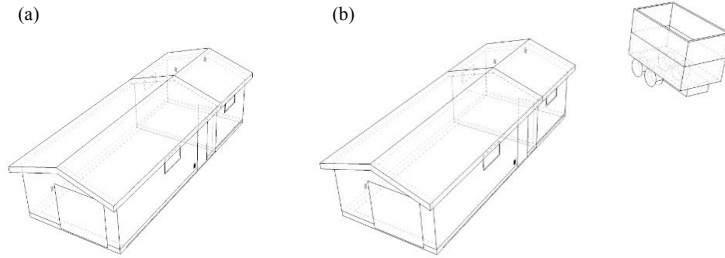


Figure 1. Reference building (a) completely exposed and (b) partially sheltered

### 2.2. Test cases

Three different methods were used to estimate the infiltration in the reference building. Firstly, the Norwegian technical software (SIMIEN), that completely ignores the wind pressure coefficients, was employed to calculate the air infiltration rate. Secondly, the commercial BES software DesignBuilder was used to calculate the infiltration. DesignBuilder uses simplified pressure coefficients that derive by standard datasets. Furthermore, the wind pressure coefficients were defined by CFD simulations and were used as input on the same BES program in order to calculate the infiltration rate of the building. The integrated CFD module of DesignBuilder was used to define the pressure variations on the building façades, and consequently calculate the wind pressure coefficients  $C_p$ .

In order to examine the effect of microclimate on the wind pressure coefficients, all test cases were additionally tested for semi-exposed building. A high truck was placed diagonally, approximately 5 meters from the north-east corner of the building, providing thus a shelter from the weather conditions [Figure 1]. The test cases are presented briefly in Table 1.

Table 1. Test cases

	Exposed	Sheltered
ac/h	without $C_p$ (SIMIEN)	
	$C_p$ values from dataset	
	$C_p$ values from CFD simulations	

### 2.3. Simulations

#### 2.3.1 Norwegian technical software SIMIEN

The Norwegian national standard for calculation of energy performance of buildings (NS 3031:2014) does not take into consideration the wind pressure coefficients  $C_p$  during the calculation of air infiltration. The air changes are given by the following equation:

$$n_{inf} = \frac{n_{50} e}{1 + \frac{f(V_1 - V_2)}{V \cdot n_{50}}} \tag{3}$$

where

- $e, f$  are terrain shielding coefficients
- $n_{50}$  is the air infiltration when the difference pressure between indoors and outdoors is 50 Pa [ac/h]
- $V$  is the total heated volume of the building [m<sup>3</sup>]
- $\dot{V}_1$  is the supply airflow from the mechanical ventilation system [m<sup>3</sup>/h]
- $\dot{V}_2$  is the extract airflow from the mechanical ventilation system [m<sup>3</sup>/h]

The air changes of the reference building at 50 Pa had previously been defined through pressurization test and it was determined to be equal to 8.17 ac/h [4].

### 2.3.2 BES software using standard $C_p$ values

The BES software DesignBuilder employs the power law to calculate infiltration rate. The ventilation rate  $q$  through each opening and crack is calculated based on the pressure difference using wind and stack pressure:

$$q = C \cdot \Delta P^n \quad (4)$$

where

$q$	is the volumetric flow entering the opening/crack	[m <sup>3</sup> /h]
$\Delta P$	is the pressure difference across the opening/crack	[Pa]
$n$	is the flow exponent varying between 0.5 for fully turbulent flow and 1.0 for fully laminal flow	
$C$	is the flow coefficient, related to the size of the opening/crack	

When wind impinges on the building façade, a positive pressure is induced on the upwind face. The flow separates at the corners resulting in negative pressures regions on the side of the building and a negative pressure distribution on the leeward façade. The pressure at any point on the surface of a building façade can be represented by:

$$P_w = \frac{1}{2} \rho C_p U_z^2 \quad (5)$$

where

$P_w$	is the pressure due to wind	[Pa]
$\rho$	is the density of air	[kg/m <sup>3</sup> ]
$C_p$	is the wind pressure coefficient at a given position	
$U_z$	is the mean wind velocity at height $z$	[m/s]

The software uses a database of wind pressure coefficients provided by the Air Infiltration and Ventilation Center (AIVC). The  $C_p$  data regard buildings consisting of 3 storeys or less, with square surfaces and for 3 levels of site exposure. The  $C_p$  data are given in 45° increments [5].

### 2.3.3 BES software using $C_p$ values calculated from CFD simulations

CFD simulations remain a complicated task that requires high level of expertise and computational capacity, invaluable amount of time and eventually comes with great cost. Contemporary BES programs provide the possibility of integrated pre-processing and post-processing between BES and CFD. In such cases, CFD simulations may appear as less advanced due to the predefined numerical scheme and discretization, as well as the single choice of a turbulence model and the limitation of coarse grids. However, they are able to provide numerical analysis of fluid flow in a user-friendly environment and in short time.

The CFD tool of DesignBuilder employs the Reynolds-averaged Navier-Stokes equations (RANS) equations in combination with the standard  $k$ - $\epsilon$  turbulence model. Furthermore, it uses second-order numerical discretization schemes. The main disadvantage of the specific CFD tool lays on the grid resolution, which cannot exceed the limit of 0.1 m for each grid cell, providing thus a rather coarse grid.

An average value for wind pressure coefficient  $C_p$  was defined for each façade of the building. The  $C_p$  were calculated for eight different wind directions (N, S, E, W, NE, SE, NW, SW). The set of the eight calculated  $C_p$  for each façade was imported at the building energy simulation, which determined the infiltration rate of the building based on equations (4) and (5).

In order to verify the accuracy of the CFD tool, CFD simulations were also performed in OpenFOAM, using also the RANS equations and the standard k- $\epsilon$  turbulence model, but finer grid. The wind pressure coefficients were calculated for each façade and for all eight wind directions. These  $C_p$  values were also used at the BES program to determine the air infiltration rate of the reference building.

### 3. Measurements

The concentration test decay method (ASTM – E741, 2006) was employed for measuring the average infiltration rate of the reference building. A volume of CO<sub>2</sub> was distributed uniformly in the interior of the building and two CO<sub>2</sub> loggers were monitoring the concentration of the tracer gas inside the building within a time interval of 10 minutes. The highest concentration recorded was approximately 5000 ppm and it was finally stabilized at approximately 400 ppm. For each time, the normalized concentration  $C_N$  was calculated based on equation:

$$C_N = \frac{C(t) - C_o}{C(0) - C_o} \quad (6)$$

Where

$C(t)$  is the tracer gas concentration in given time [ppm]

$C_o$  is the tracer gas concentration outdoors [ppm]

The ‘optional regression model’ (ASTM-E741, 2006) was used to obtain the average air changes, using the following equation:

$$\ln C_N = -At + \ln C_N(0) \quad (7)$$

Performing a regression of  $\ln C_N$  against  $t$  will give a fit line, whose slope represents the average infiltration rate.

In total, six measurements took place in the reference building: three measurements for the totally exposed building and three measurements while the building was partially sheltered. During the tracer gas measurements, the wind speed and wind direction were measured on site and were used for the simulations.

### 4. Results

Table 2 presents the wind pressure coefficient values from the standard dataset and the CFD simulations. As it is expected, the CFD tool calculates with higher accuracy the  $C_p$  values on every façade, while the analytical dataset significantly underestimates them. Although the integrated CFD tool does not achieve the same level of accuracy as OpenFOAM, it still manages to describe the wind-induced variations on the building facades.

Table 2. Wind pressure coefficients for the north façade of the reference building

Wind direction (normal to surface)	$C_p$ from dataset	$C_p$ from integrated CFD module	$C_p$ from OpenFOAM
0 °	0.40	0.70	0.62
45 °	0.10	0.38	0.37
90 °	-0.30	-0.78	-0.43
135 °	-0.35	-0.33	-0.36
180 °	-0.20	-0.12	-0.21
225 °	-0.35	-0.33	-0.35
270 °	-0.30	-0.68	-0.51
315 °	0.10	0.48	0.21

The air infiltration results that derived from the three different types of simulations are compared to the measurements performed in the reference building for both cases of exposure and they are shown in Table 3. It is obvious, that the oversimplified method followed by the Norwegian technical software leads to large errors in calculating air infiltration. The commercial BES software that employs a more sophisticated method of calculating the air infiltration rate, using a defined dataset for the  $C_p$  values, predicts rather better results. However, the same BES program, when utilize the  $C_p$  values produced by its CFD module, seems to be able to calculate the infiltration rate with an impressive proximity to the actual air changes measured, deviating only 2-15% from the actual rates. As it is expected, the best results derive from the BES software, when the  $C_p$  values derived from OpenFOAM simulations. However, it is important to highlight that, although the simplified integrated CFD module is not able to depict the same details on the wind-induced pressure variations as OpenFOAM, it still manages to achieve quite accurate results.

Table 3. Air infiltration rates [ $\text{ach}^{-1}$ ] for all tested cases

Test case		SIMIEN	BES with $C_p$ from dataset	BES with $C_p$ from integrated CFD module	BES with $C_p$ from OpenFOAM	Tracer gas measurements
Exposed	1	0.82	0.45	0.57	0.54	0.56
	2	0.82	0.39	0.39	0.42	0.43
	3	0.82	0.40	0.56	0.53	0.50
Sheltered	1	0.57	0.54	0.61	0.63	0.67
	2	0.57	0.95	0.64	0.66	0.73
	3	0.57	0.51	0.60	0.62	0.72

## 5. Conclusion

Research has already shown that the impact of wind pressure coefficients  $C_p$  on the air infiltration of the building is without any doubt of high importance. The disregard of them during the energy performance estimation can lead to large errors. Analytical models and datasets provide a rough estimation of  $C_p$  values that can be used on BES and decrease this error. However, wind pressure coefficients depend significantly on microclimatic factors, such as wind speed and directions and surroundings. Many authors have highlighted that the best policy for the calculation of wind pressure coefficients is through CFD simulations, resulting in minor errors during the determination of energy performance of the building.

Although CFD simulations remain a complicated task that demands high expertise and high computational time and cost, many BES programs are nowadays launched with integrated CFD modules. Despite the fact that such modules are known to lack the high level of accuracy of proper numerical CFD simulations, the integrated pre-processing and post-processing between BES and CFD has advanced significantly, providing thus an acceptable estimation of the wind-induced pressure variations on buildings. As a result, a good calculation of the wind pressure coefficients, and consequently a more realistic estimation of the air infiltration rate, is feasible in short time and with low computational cost.

## References

- [1] Costola D, Alluci M. Pressure coefficient simulated by CFD for wind-driven ventilation analysis. Proceedings: Buildings Simulations. 2007
- [2] Costola D, Blocken B, Hensen JLM. Overview of pressure coefficient data in building energy simulation and airflow network programs. Building and environment. 2009;2027-2036
- [3] Pisello AL, Pignatta G, CastaldoVL, Cotana F. The impact of local microclimate boundary conditions on building energy performance. Sustainability. 2015;9207-9230
- [4] Kraniotis D, Aurlien T, Thiis T. Investigating instantaneous wind-driven infiltration rates using the  $\text{CO}_2$  concentration decay method. International Journal of Ventilation. 2016;2044-4044
- [5] Air Infiltration and Ventilation Centre. A guide to energy efficient ventilation. Annex V. 1996
- [6] ASTM International E741-06. Standard test method for determining air change in a single zone by means of a tracer gas dilution. ASTM. 2006





## Paper III

# Effect of microclimate on wind-induced pressurization of the building envelope: a test case of twin high-rise buildings

Stergiani Charisi<sup>1,\*</sup>, Thomas K. Thiis<sup>1</sup> and Tormod Aurlien<sup>1</sup>

<sup>1</sup>Faculty of Science and Technology, Norwegian University of Life Sciences, Ås, Norway

\*Corresponding email: [stergiani.charisi@nmbu.no](mailto:stergiani.charisi@nmbu.no)

## ABSTRACT

The pressurization of the building envelope is the driving mechanism for air infiltration and exfiltration of the building. Wind pressure coefficients ( $C_p$ ) are used to express the wind-induced pressure on the exterior of the building and they can be included in building energy simulations (BES) for calculating the air infiltration of the building. Consequently, knowing the wind-induced pressure distribution on a building can help in accurately predicting its air infiltration. As the air flow around a building depends on its geometry and surroundings, similarly the pressure variations along a building façade depend on the local microclimate. In this study, two twin high-rise buildings are investigated. The two buildings have the same geometry of rectangular prism and they are almost parallel to each other with a distance of approximately ten meters between them. The buildings' long axes are running East-West and they are situated in a Norwegian town (Ås, Akershus) where the annual dominant wind direction is South. As a result, one building is providing substantial wind shelter to the other throughout the year. The pressure differences in different heights between the windward and leeward façades of both buildings are measured simultaneously. The in-situ measurements show that the sheltering effect caused by one building reduces significantly the pressurization of the other building, especially for South wind direction. Computational Fluid Dynamics (CFD) simulations were performed in order to evaluate their ability to capture this sheltering effect. As a result, although the two buildings have exactly the same design, the sheltered building is expected to have lower air infiltration due to the local microclimate.

## KEYWORDS

microclimate, wind pressure coefficient, pressure measurements, CFD

## INTRODUCTION

The air infiltration of a building can significantly affect its energy balance. Wind-induced pressure, stack-effect and mechanical ventilation are the driving forces for the air flow in and out of a building (Haghighat et al. 2000). Studies have showed that urban microclimate has a great impact on the wind flow around buildings (Toparlar et al. 2017). Consequently, the wind-induced pressurization of the building envelope, and thus the total air infiltration and energy balance of a building, can be affected by the microclimate.

One method to account for the microclimate effect on the pressurization of a building in Building Energy Simulation (BES) is through wind pressure coefficients ( $C_p$ ) (Charisi et al. 2017).  $C_p$  is used to express the wind-induced pressure on the exterior of the building and depends on wind direction, site exposure and position on the building façade. Standard databases are the most widely used source of  $C_p$  values for BES (Costola et al. 2009) and they usually include simple building geometries and generic site exposure conditions. As a result, similar buildings situated in the same neighbourhood will be treated equally. However, in cases of big-scale building complexes, one building can provide substantial wind shelter to its

neighbouring buildings. That sheltering effect combined with weather patterns can have great impact on pressurization of the building envelope. Knowing the wind-induced pressure distribution on building façades can help calculate accurate  $C_p$  values and subsequently predict more realistically the air infiltration of the buildings.

On-site pressure measurements is the most realistic method to calculate the pressure variations on a building, but they are difficult, time consuming and rarely performed (Richards et al. 2001). The alternative method of Computational Fluid Dynamics (CFD) simulations is commonly used to predict the wind-induced pressure distribution on building façades (Toparlar et al. 2017), although the CFD method may include limitations, such as steady state analysis, approximating turbulence modelling and simplified meshing.

This study investigates the shielding effect on the pressurization of the building envelope in the case of a twin high-rise building complex. The pressure difference between leeward and windward side was measured simultaneously on the facade of two identical eight storey buildings. Furthermore, the measurements were used to validate the accuracy of CFD simulations.

## METHODS

### Pressure measurements

The pressure difference between the windward and leeward side of the twin buildings was measured simultaneously in multiple points. Six pressure taps were placed in three different heights – top, middle and low part of the building – and in three different lateral positions – one close to each edge of the building and one on the middle of the building [Figure 1b]. The pressure taps were placed symmetrically on the South (windward) and North (leeward) façades of the buildings [Figure 1b], and at the same exact positions on both buildings. The pressure taps had a diameter of 3mm and they were placed in the middle of square plate with area  $0.01\text{ m}^2$ , in order to avoid turbulent flow around the tap nozzle [Figure 2]. The pressure taps were connected with silicone tubes with a diameter of 3mm to the differential pressure sensors that were placed on the rooftop of each building. The data acquisition system was recording the instantaneous pressure difference values with a frequency of 1 Hz.

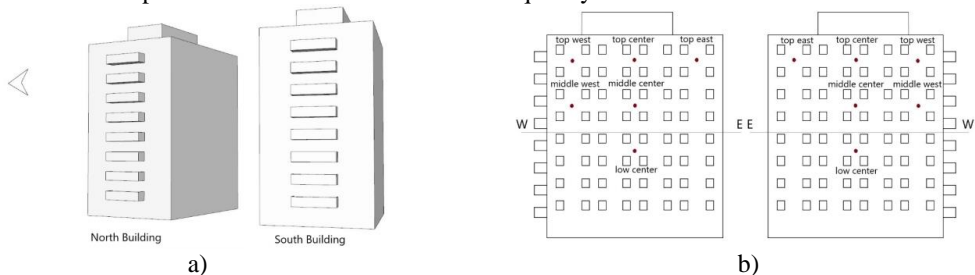


Figure 1. a) Perspective view of the twin high-rise buildings, b) positions of pressure taps (red dots) on the South and North façade of the buildings.

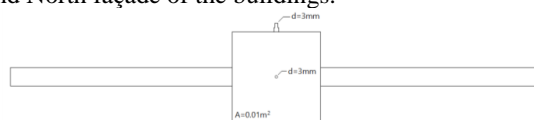


Figure 2. Drawing of the pressure taps used for the measurements. The silicon tubes were connected to the top nozzle of 3mm, which was connected with the 3mm hole on the centre of the square plate. The ‘flaps’ on both sides were used to stabilize the pressure taps on the façade.

## CFD simulations

Steady state CFD simulations were performed for the predominant wind speed and direction around the reference buildings during the measurements' period, in order to define the pressure variations on the building façades and evaluate if the CFD simulations are able to capture the sheltering effect as was measured. The CFD simulations employed the Reynolds-averaged Navier Stokes (RANS) equations in combination with the standard  $k-\epsilon$  turbulence model. The Semi-Implicit Method for Pressure Linked Equations (SIMPLE algorithm) was used for the velocity-pressure coupling and second-order discretization schemes were used for both the convection and viscous terms of the governing equations. Also, vertical profiles for the mean velocity  $U$ , turbulent kinetic energy  $k$  and dissipation rate  $\epsilon$  were defined as initial boundary conditions (Tominaga et al. 2008). The 3d model used for the CFD simulations included all the neighbouring buildings of the twin high-rise building complex in a radius of approximately 100 meters, along with the terrain altitude variations [Figure 3]. The simulation domain was defined to be 5 times the width and length of the 3d model, and 3 times its height. The mesh created is an unstructured hexahedral mesh with extra finer layers close to the building surfaces.



Figure 3. a) Satellite picture of the building complex and its surroundings, b) 3d model used for the CFD simulations. The twin buildings are marked inside the red frame.

## RESULTS

The fluctuating data obtained through the pressure measurements was smoothened, and the 'noise' due to the length of the tubing was filtered out by the means of moving average (Smith 1997). During the wind incidents, it is considered that the leeward façade (North) will maintain a stable, relatively low pressure, and subsequently the measured pressure difference will reveal the wind-induced pressure variations on the windward façade (South).

Figure 4 shows that during all three days of measurements, the top part of the windward façade of the Southern building develops high pressures that fluctuate from 2 to 20 Pa higher than the leeward façade, depending on the incident wind. At the same time, its twin Northern building has almost zero pressure difference between windward and leeward side regardless the wind speed, meaning that the South building provides substantial shielding that prevents the wind-induced pressurization of the Northern building's windward façade, even at its most exposed parts. Especially during measurement 'Day 3' that the dominant wind direction is South and the average wind speed approximately 7 m/s, the wind-induced pressure difference on the top center of the windward façade of the South building is 20 Pa, while the corresponding wind-induced pressure difference on the Northern building is close to 0Pa.

Figure 5a shows that for South, South-East and South-West wind directions, the wind-induced pressurization of the top part of the building is significantly larger than the rest of the building envelope. This pressure difference between leeward and windward façade appears only on the Southern building, which is exposed to the wind. The Northern building's envelope does not present any wind-induced pressurization, even at the highest part of its construction, due to the sheltering provided by its twin building. The negative pressure difference on the lower part of

the Northern building is probably the result of turbulence caused by the existence of big rocky wall in close proximity ( $\sim 3\text{m}$ ) to the bottom of the building.

Figure 5b presents the pressure difference on the west part of the twin buildings. For the top parts of the buildings, higher pressures are developed on the Southern building, which is exposed to wind. The pressure difference of the middle parts close to the edges of the building envelope is significantly lower. However, it seems to be very dependent on the wind direction. This effect is more obvious during ‘Day 1’ at which the dominant wind direction was South-West. Probably the turbulence developed inside the narrow passage between the twin buildings has as a result the development of higher pressures on the windward façade of the sheltered Northern building [Figure 5b].

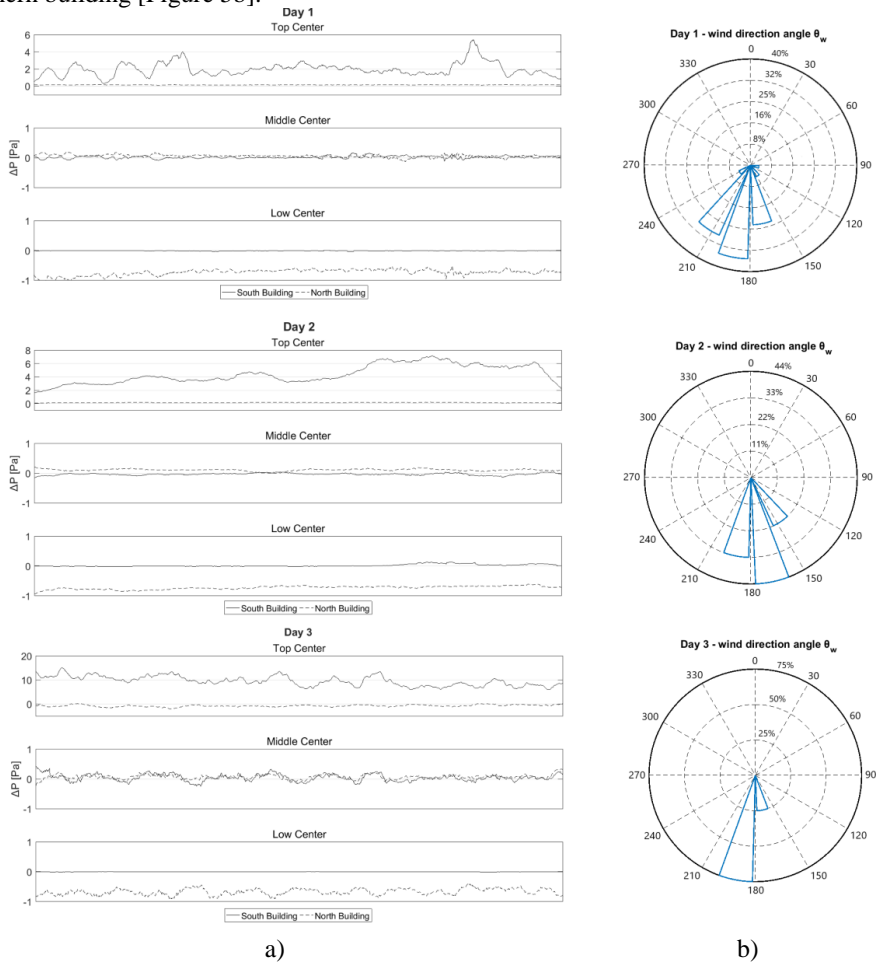


Figure 4. a) Measured pressure differences on the top part of the two twin buildings and b) corresponding wind roses depicting the variation of the direction angle  $\theta_w$  during each measurement ‘day’ ( $\theta_w = 0^\circ$  corresponds to North wind,  $\theta_w = 90^\circ$  to East,  $\theta_w = 180^\circ$  to South and  $\theta_w = 270^\circ$  to West)

The pressure differences measured during an instantaneous wind incident of speed 7.1 m/s and direction  $184.4^\circ$  are compared with the corresponding pressure difference calculated with a

CFD simulation for the same wind profile [Table 1]. Overall, the CFD simulation manages to predict correctly the pressure variation lengthwise and along height the building façades. However, on the exposed Southern building, it overestimates the pressure difference in almost all the measuring points, which is probably the result of comparing a steady-state simulation with a very dynamic phenomenon. The CFD simulation successfully captures the sheltering effect of the South building to the North. The calculated pressure differences for the Northern building remain at the same low levels as the measured ones. However, the CFD simulation shows that the windward façade of the Northern (sheltered) building is under-pressurized, in contradiction to the on-site measurements that show that the windward façade of the sheltered building is slightly over-pressurized. It is possible that the CFD simulation underestimates the turbulence caused in the passage between the twin buildings while it overestimates the turbulence caused in the exposed leeward façade of the Northern Building.

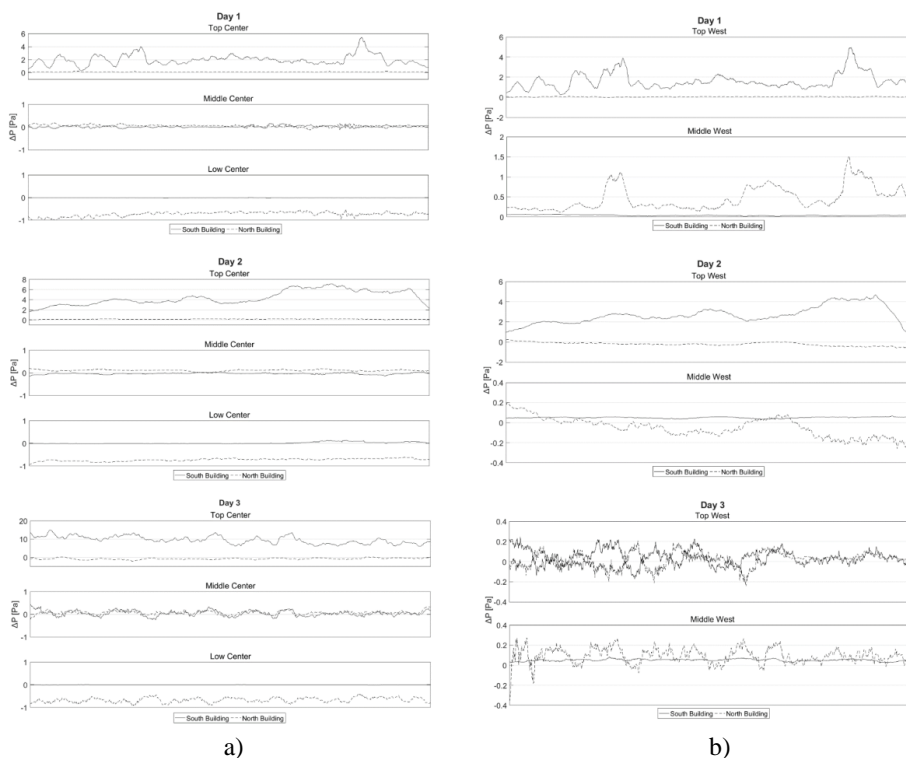


Figure 5. Pressure difference measurements a) on the top part of the twin buildings and b) on the West part of the twin buildings.

Table 1. Pressure difference on the six difference positions on the building envelope

Position	Southern Building		Northern Building	
	Measurement	CFD simulation	Measurement	CFD simulation
Top Center	53.2	60.3	6.9	-9.9
Top West	31.8	56.2	2.1	-5.8
Top East	13.3	32.6	2.8	-3.5
Middle Center	21.0	48.7	1.4	-5.1
Middle West	0.3	45.0	2.6	-4.9
Low Center	0.0	39.3	0.3	-4.8

## DISCUSSIONS

On-site pressure measurements on a twin high-rise building complex showed that one building provides substantial wind shelter to its neighbouring, reducing thus drastically its envelope pressurization. As a result, although the two buildings are identical and BES would treat them equally, the sheltered one is possible to have quite lower air infiltration. Furthermore, the measurements showed that the pressure difference on the two top floors is significantly larger than the rest of the lower parts of the building, rendering them more vulnerable than the rest of the building to energy losses due to wind-induced air infiltration. More on-site measurements on high-rise building complexes will contribute in mapping accurate  $C_p$  values for use in BES. CFD simulations proved to be able to capture the sheltering effect of one building to its twin, but it seems that they fail to accurately predict the turbulence between the two twin buildings. In such cases of high-rise building complexes, where the narrow passages between buildings play an important role, more sophisticated turbulence models should be selected after careful consideration for the CFD simulations in order to ensure accurate results.

## CONCLUSIONS

This case study shows that the wind-induced pressure distribution of twin high-rise buildings is strongly dependent on the local microclimate they form, resulting into one building providing substantial wind-shelter to its twin. On site-pressure measurements, as well as CFD simulations, can help defining the pressurization degree of the building envelopes for such cases of twin buildings. The pressure variations can later be introduced in BES in the form of building-specific  $C_p$ . Although twin buildings have identical construction and they would be expected to have the same energy needs, the wind-induced pressurization in combination with local weather patterns can potentially conclude in one building having lower energy demands than its twin.

## ACKNOWLEDGEMENT

The authors thank Arne Svendsen for helping the authors with the measuring equipment, Tom Ringstad for setting up the data acquisition system, and Ole Semb for providing access to the building facilities in daily basis.

## REFERENCES

- Charisi, S., Waszczuk, M. and T.K. Thiis. 2017. Investigation of the pressure coefficient impact on the air infiltration in buildings with respect to microclimate. *Energy Procedia*, 122, 637-642
- Costola, D., Blocken, B. and J.L.M. Hensen. 2009. Overview of the pressure coefficient data in building energy simulation and airflow network programs. *Building and Environment*, 44(10), 2027-2036
- Haghighat, F., Brohus, H. and J. Rao. 2000. Modelling air infiltration due to wind fluctuations – a review. *Building and Environment*, 35, 377-385
- Richards, P.J., Hoxey, R.P. and L.J. Short. 2001. Wind pressures on a 6m cube. *Journal of Wind Engineering and Industrial Aerodynamics*, 89, 1553-1564
- Smith, S. W. 2003. *The Scientist and Engineer's Guide to Digital Signal Processing*. 2<sup>nd</sup> Edition. *California Technical Publishing*
- Tominaga, Y., Mochida, A., Yoshie, R., Kataoka, H., Nozu, T., Yoshikawa, M. and T. Shirasawa. 2008. AIJ guidelines for practical applications of CFD to pedestrian wind environment around buildings. *Journal of Wind Engineering and Industrial Aerodynamics*, 96, 1749-1761
- Toparlar, Y., Blocken, B., Maiheu, B. and G.J.F. van Heijst. 2017. A review on the CFD analysis of urban microclimate. *Renewable and Sustainable Energy Reviews*, 80, 1613-1640





Paper IV

**DETERMINING BUILDING-SPECIFIC WIND PRESSURE  
COEFFICIENTS TO ACCOUNT FOR THE MICROCLIMATE IN  
THE CALCULATION OF AIR INFILTRATION IN BUILDINGS**

Stergiani Charisi<sup>a\*</sup>, Milosz Waszczuk<sup>a</sup> and Thomas K. Thiis<sup>a</sup>

*<sup>a</sup>Faculty of Science and Technology, Norwegian University of Life Sciences, P.O. Box  
5003, Ås, Norway*

\*Corresponding author. Email: stergiani.charisi@nmbu.no

# **Determining building-specific wind pressure coefficients to account for the microclimate in the calculation of air infiltration in buildings**

Wind pressure coefficients ( $C_p$ ) are important for the correct calculation of the air infiltration of a building.  $C_p$  depends on wind direction, position on the building façade and site exposure, and is therefore influenced by the microclimate. The external coupling between building energy simulation (BES) software and computational fluid dynamics (CFD) pre-processing allows calculating building-specific wind pressure coefficients that can account for the microclimate. Building energy simulations have been performed in order to calculate the infiltration rate of a reference building using surface-averaged  $C_p$  values from two different sources; a standard database and CFD simulations from OpenFOAM. Tracer gas measurements were performed in the reference building in order to validate the simulation results. The results show the coupled CFD/BES method gives building-specific  $C_p$  values that represent adequately the microclimatic conditions, leading up to 45% more accurate air infiltration rates compared to conventional methods.

Keywords: wind pressure coefficients; air infiltration; CFD; tracer gas; building energy simulation

## **1. Introduction**

In 2020, most of the European countries have to abide by the 2010 Energy Performance of Buildings Directive and the 2012 Energy Efficiency Directive, and the building energy saving will consequently increase if they follow the directives (European Commission 2010; 2012; 2018) . The new challenge for modern societies is the transition to clean energy, and the development of sustainable zero energy and zero emission neighbourhoods in smart cities. Electricity can be generated from sustainable sources like wind, solar and geothermal power with little or no pollution or global warming emissions, and it can be widely used for covering the energy demands of the building sector (SSB 2012). At the same time, more and more modern societies invest in sustainable ways of transportation, such as hybrid or electric vehicles, creating thus an extra electricity demand. As a result, the correct prediction of energy demands in a neighbourhood level

seems to become a necessity in the near future, as it will facilitate the energy distribution on the grid. Defining accurately the energy demands of buildings based on the microclimate formed by their actual surroundings will significantly contribute towards achieving this goal (Mochida et al., 2006; Shirzadi et al., 2018; Shirzadi et al., 2018).

Recent studies have already documented the effect of urban microclimate on energy performance of buildings (Toparlar et al., 2017; Allegrini et al., 2012; Moonen et al., 2012; Priyadarsini 2011; Oxizidis et al. 2011). In large cities, where the urban typologies vary widely from neighbourhood to neighbourhood, the implementation of local microclimate in building energy performance simulations will give the advantage of predicting more accurately each building's energy balance.

Many recent studies focus on microclimate's effect on the energy use of buildings and suggest different approaches of quantifying this effect. Niikho et al. (2017) employ computational fluid dynamics (CFD) in order to define the wind pattern around buildings and alternate accordingly the conventional typical climate data used in the building energy simulations. Similarly, Pisello et al. (2015) conduct CFD simulations in order to define more accurate air temperatures and relative humidity (RH) that can be used as climatic boundary conditions for the determination of the energy demands of buildings. Tsoka et al. (2017) introduce the urban microclimate into building energy simulation by generating 'urban specific weather datasets' based on monthly averages that are provided by simulated urban microclimatic results. Shirzadi et al. (2018) employ an improved CFD model based on experimental data in order to calibrate BES model's input, such as velocity profile, discharge coefficient and convective heat transfer coefficients, and thus account for urban microclimate interactions. Other scientific studies perform CFD simulations in order to define the air flow around buildings and calculate wind speeds, air temperatures and convective heat transfer coefficients, that can later be used as input on

the building energy simulation for quantifying the impact of local microclimate on building energy consumption (Allegrini et al., 2013; Malys et al., 2015).

External coupling between CFD and BES, a.k.a. the exchanging data process between two programs, has already been reported in many studies that aim to improve the building energy performance with respect to microclimate (Zhang et al., 2018, Yi and Feng, 2013; Fan and Ito, 2012; Barbason and Reiter, 2014; Boujer et al., 2011; Djunaedy et al, 2008; Costola et al, 2009). Most studies focus on the correct calculation of convective heat coefficients from CFD simulations that can be used as input on the BES in order to account for the microclimatic effect. Costola et al. (2009) described how the integration of CFD pre-processing into BES software could enhance the use of CFD as source of  $C_p$  data. This paper investigates the wind-pressure coefficient impact on the air infiltration of the buildings with respect to microclimate.

Air infiltration is one of the most important factors that determine the energy demands of a building (Younes et al., 2012). The driving mechanism for air infiltration in a building is the pressurization of the building envelope, caused by wind and air buoyance forces (Lyberg, 1997).

In most applications, the air infiltration of a building is calculated based on its air leakage number  $n_{50}$  and two rather generic shielding and height correction coefficients, provided by the relevant national energy performance standards (SN/TS 3031:2016). As a result, the air infiltration calculated is merely an approximation of the actual infiltration rates of the building, due to the oversimplification of the microclimatic boundary conditions.

Wind pressure coefficients ( $C_p$ ) are used to express the wind-induced pressure on the building envelope. As the local microclimate can affect the air flow around buildings, similarly it can affect the pressure variations along the building envelope. Consequently,

$C_p$  depends on a set of parameters that includes wind direction, position on the building surface and façade exposure. Therefore, the use of wind pressure coefficients can introduce the microclimatic conditions on the calculation of air infiltration of the building, leading to estimation of more realistic air infiltration rates.

$C_p$  values can derive from different sources, such as full-scale measurements, reduced-scale measurements in wind tunnels, CFD simulations, databases and analytical models (Costola et al., 2009). Studies have shown that the most accurate way to define the  $C_p$  values of a building are full-scale measurements, while wind-tunnel measurements and CFD simulations are following in accuracy (Costola et al., 2009; Costola and Alucci, 2007; Miyoshi et al., 1971; Surry, 1991; Richards et al., 2001; Uematsu and Isyumov, 1999). Full-scale measurements are complicated, time-consuming, expensive and therefore rarely performed (Costola et al., 2009). Similarly, wind-tunnel measurements come at high cost and expertise and are used for limited applications (Costola et al., 2009). However, full-scale and reduced-scale measurements have been used for validating modelling methods, such as CFD simulations, and their results have been used to create typical  $C_p$  databases (Costola et al., 2009). On the other hand, CFD simulations can be performed in the comfort of an office space and still produce accurate  $C_p$  values. However, the amount of time, computational capacity and expertise required for CFD simulations renders them scarcely used in the building industry.

$C_p$  databases consist the most commonly used source for BES and they usually include simple cases of rectangular or square buildings and generic exposure conditions (Costola et al., 2009).  $C_p$  databases comprise data that have been collected from various sources, such as full-scale measurements and wind-tunnel measurements. The data are classified in different typical categories based on common factors, such as building geometry and degree of shelter/exposure. For each category, the wind pressure

coefficients are given as an average value for each façade of the building and in increments of 30° or 45° for the wind direction. The most widely used  $C_p$  database in the ventilation field is the one established by the Air Infiltration and Ventilation Centre (AIVC). The AIVC published its first compilation of wind pressure coefficients shortly after a workshop held about the wind pressure coefficients (Liddament, 1986) and ever since became an important reference for air infiltration and ventilation issues. Nowadays, the AIVC Guide to Ventilation (Liddament, 1996) is published with tables including  $C_p$  design data for low-rise buildings. The term ‘low-rise buildings’ refers to buildings up to three storeys. For taller buildings, the AIVC guide refers the reader to Bowen (1976), which provides vertical profiles for high-rise buildings. The generic nature of the conditions given by the AIVC database makes it difficult to properly represent the microclimatic characteristics of a building or/and sheltering cases that do not fall under the given categories. However, when it comes to using tabulated  $C_p$  values from databases for building energy simulations, the user shall choose data from the category most similar to the case tested.

Computational Fluid Dynamics (CFD) methods have been constantly developing the past 5 decades and are widely used for solving air flow problems in the built environment. CFD simulations are able to calculate wind pressure distributions around buildings with high accuracy (Stathopoulos, 1997; Hirt and Cook, 1972; Murakami and Mochida, 1988; Tominaga et al., 2008; Yand et al., 2006; Nozu et al., 2008). Since pressurization of the building envelope is the driving force for air infiltration and exfiltration, the wind-induced pressure distribution around a building is critical to its air infiltration rate (Lyberg, 1996; Haghighat et al., 2000). Consequently, knowing the pressure variations due to wind around a building can help define the wind-pressure

coefficients, which can be introduced in the building energy simulations and define the wind-driven infiltration rate (Costola et al., 2009).

The use of wind pressure coefficients for the prediction of air infiltration in the building energy simulation has already reported (Walker and Wilson, 2011; Asfour and Gadi, 2007; Costola and Alucci, 2007; Charisi et al., 2017). This study primarily investigates the use of building-specific wind pressure coefficients as an appropriate input to BES that can account for the microclimate. In addition, an external coupling between CFD simulations and BES is attempted. The CFD simulations are used to calculate building-specific wind pressure coefficients that can capture the building's microclimatic conditions and that are used as input on the BES program. Furthermore, the use of tabulated wind pressure coefficients as input to BES is evaluated. Each method's accuracy – use of tabulated  $C_p$  values and use of building-specific  $C_p$  values - in predicting the air infiltration of a reference building for two different microclimates is explored. The calculated air infiltration rates are compared with on-site measurements for two different microclimatic cases in order to establish whether the use of building-specific  $C_p$  values suffice as microclimatic boundary conditions.

## **2. Methodology**

Wind pressures coefficients deriving from two available sources are implemented on the same building energy simulation software and their impact on the calculation of air infiltration is examined. Tracer gas measurements performed at a reference building are used to evaluate, at first, the efficiency of wind-pressure coefficients in introducing the microclimate on the air infiltration calculation, and, secondly, to evaluate each method's accuracy on the calculation of air infiltration.



## 2.1 Reference building

The building used as a reference for this study is a low-rise building, fully exposed in open terrain and is situated in the suburban town Ås, Norway [Figure 1]. The building's long axis has North-South orientation with an angle of  $6.5^\circ$  [Figure 2]. The building is a one-storey light timber construction and consists of an insulated room that is sporadically used as an office, a non-insulated garage space, and a cold attic [Figure 2]. The office room is separated from the garage space with an insulated timber wall with a door. The floor is insulated with 10 cm of extruded polystyrene, while the walls (including the internal partition wall) and the ceiling are insulated using mineral wool of 10 cm width. The office space includes two window openings, while the garage space includes one window, one door and one garage-door. Four small square vents of area  $0.023 \text{ m}^2$  – two on each room - that are used for natural ventilation, are placed around the building envelope. Electrical convectors heat the office room, but the building has not mechanical ventilation system. The garage space is neither insulated nor heated. Figure 2 shows a perspective drawing of the reference building and its rooms.



Figure 1. The reference building and its surroundings

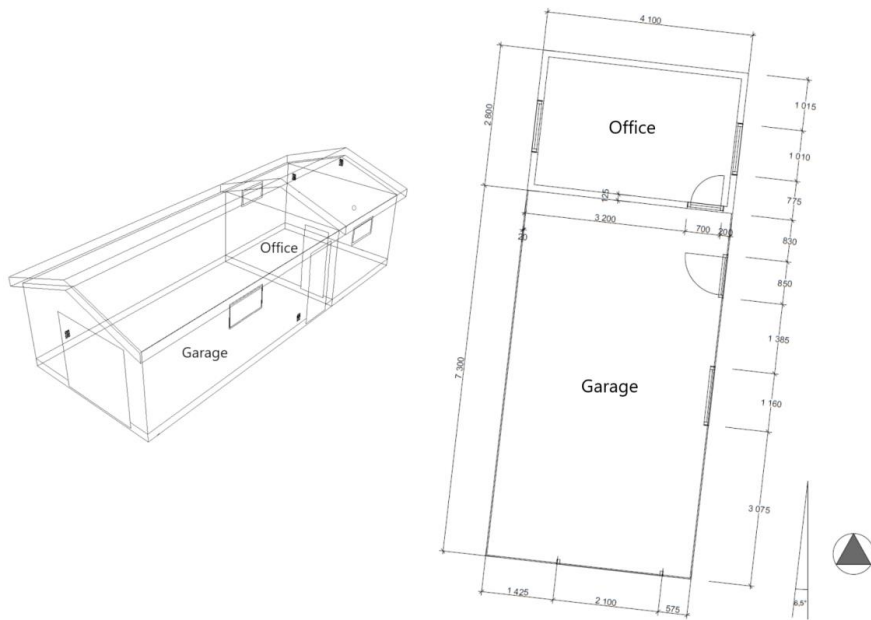


Figure 2. Wireframe drawing of the reference building and layout of the building with detailed dimensions in mm.

Two different cases of building microclimate (exposed/sheltered) were investigated. A compact obstacle (truck) of dimensions 4.2m $\times$ 2.2m $\times$ 4.0m was placed 5 meters away from the North-East corner of the reference building [Figure 3]. The obstacle was providing partial shielding to the building from wind.

The building is located inside the meteorological field where the university's weather station facilities are located. Therefore, all the weather data used for the building energy simulations were measured 10 meters outside the reference building by the weather station equipment.

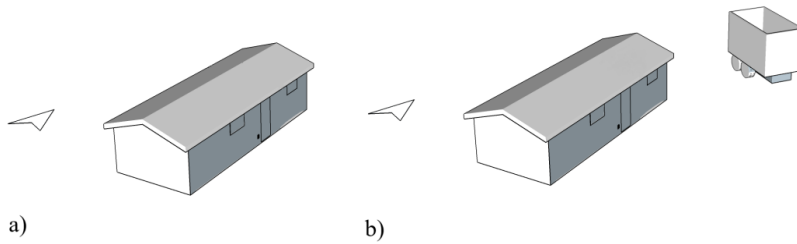


Figure 3. Reference building a) completely exposed and b) partially sheltered on the North-East façades

## 2.2 Test cases

In order to evaluate each method’s efficiency for different microclimates, all wind pressure coefficients were determined for the additional case of sheltered building.

Since the most common practice of defining air infiltration rate in buildings is the use of  $n_{50}$  as input in building energy simulation, one additional case was examined. The air leakage number of the reference building was measured through a blower door test (ASTM, 2006) and the air infiltration of the reference building was calculated based on the specific  $n_{50}$  through building energy simulation.

All the test cases are presented briefly on table 1.

Table 1. Test cases

	Exposed	Sheltered
ac/h	$n_{50}$	
	$C_p$ values from database	
	$C_p$ values from OpenFOAM	

## 2.3 Simulations

### 2.3.1 Building Energy Simulation (BES)

In this study, a commercial third-party graphical user interface for EnergyPlus

(DesignBuilder) was used for the building energy simulations, and the different approaches described below were followed for the calculation of the air infiltration rate.

### 2.3.1.1 BES using air leakage number ( $n_{50}$ ).

The most commonly used infiltration model is the ‘Design Flow Rate’ model, in which the user defines a design flow rate that can be modified by temperature differences and wind speed. EnergyPlus calculates infiltration load based on design infiltration rate ( $I_{design}$ ), schedule fraction ( $F_{schedule}$ ), temperature difference between the zone and outdoor air, and wind speed, using the following basic equation:

$$Infiltration = I_{design} * F_{schedule} * (A + B * |T_{zone} - T_{odb}| + C * Windspeed + D * Windspeed^2) \quad (1)$$

The four coefficients A, B, C and D can be defined by users to take into account the effect of microclimate conditions of temperature and wind speed at each simulation time step (Engineering Reference, 2017). The default values are set to 1, 0, 0, and 0, which gives a constant flow of infiltration under all conditions. The design volume flow rate (noted as  $I_{design}$  in the above equation) is the maximum amount of infiltration expected at design conditions. The resulting volume flow rate is converted to mass flow using the current outdoor air density at each time step.

The BES software converts a known leakage number at a fixed building pressure to the corresponding design infiltration rate needed for the infiltration model based on the European Standard for Heating systems in buildings EN12831 (2003). According to the standard, the infiltration air flow rate induced by wind and stack effect on the building envelope can be calculated by the following equation:

$$V_{inf} = 2 \cdot V \cdot n_{50} \cdot e_i \cdot i \quad (2)$$

where

$n_{50}$  = air exchange rate per hour ( $\text{h}^{-1}$ ), resulting from a pressure difference of 50Pa between the inside and the outside of the building, including the effects of air inlets

$e_i$  = shielding coefficient, which takes into consideration the façade exposure to wind

$i$  = height correction factor, which takes into account the increase in wind velocity with the height of the space from ground level

$V$  = the volume of the heated space ( $\text{m}^3$ )

Values for  $n_{50}$  are given by national regulations that are based on a plethora of representative building measurements. In case of existing buildings, the  $n_{50}$  is possible to be calculated through a fan pressurization test (ASTM 2010). The air infiltration rate of the reference building at pressure difference of 50Pa was measured at  $n_{50}=8.2$  ac/h (Kraniotis et al., 2014).

### 2.3.1.2 BES using $C_p$ values

The ventilation rate through the building envelope is based on the pressure difference caused by wind and stack effect and can be described by the following power law equation:

$$Q = C \cdot \Delta P^n \quad (3)$$

Where

$Q$  = the volumetric air flow through the building [ $\text{m}^3/\text{s}$ ]

$C$  = flow coefficient related to the size of opening/cracks in the building envelope

$\Delta P$  = total pressure difference across the construction including wind pressure and stack effect [Pa]

$n$  = flow exponent varying between 0.5 for fully turbulent flow and 1.0 for fully laminar flow

The BES software uses information on crack data given by the ‘Numerical Data for Air Infiltration and Natural Ventilation Calculations’ by AIVC (Orme et al., 1998). The airtightness is defined through a five point scale which correspond to five pre-defined crack templates ranging from very poor for very leaky buildings to excellent for very airtight buildings. The cracks database has been set up in five categories based on range of building types. Each category gives characteristic flow coefficients and flow exponents for each component of the building, such as openings, walls, floors, ceilings and roofs. Since the air leakage number of the reference building has been measured through blower door test and was found to be  $n_{50}=8.2$  ac/h, the reference building can be considered as a leaky building. The crack template selected for the non-insulated zones, such as the garage space and the cold attic, was ‘very poor’, while the ‘poor’ crack template was chosen for the insulated office space. The corresponding flow coefficients and exponents for all building components are given in Table 2. The same crack template was used for all the building energy simulations.

Table 2. Flow coefficients  $C$  and flow exponents  $n$  used for the reference building during the building energy simulations

Building component		Flow coefficient $C$ at 1Pa		Flow exponent $n$	
		‘Very poor’	‘Poor’	‘Very poor’	‘poor’
Windows	External	0.0030 kg/sm	0.0010 kg/sm	0.60	0.60
	Internal	0.0030 kg/sm	0.0018 kg/sm	0.60	0.60
Doors	External	0.0030 kg/sm	0.0018 kg/sm	0.66	0.66
	Internal	0.0200 kg/sm	0.0200 kg/sm	0.60	0.60

<b>Vents</b>	<b>External</b>	0.0400 kg/sm	0.0100 kg/sm	0.66	0.66
	<b>Internal</b>	0.0200 kg/sm	0.0090 kg/sm	0.60	0.60
<b>Walls</b>	<b>External</b>	0.0004 kg/sm <sup>2</sup>	0.0002 kg/sm <sup>2</sup>	0.70	0.70
	<b>Internal</b>	0.0190 kg/sm <sup>2</sup>	0.0050 kg/sm <sup>2</sup>	0.75	0.75
<b>Floors</b>	<b>External</b>	0.0020 kg/sm <sup>2</sup>	0.0010 kg/sm <sup>2</sup>	1.00	1.00
	<b>Internal</b>	0.0030 kg/sm <sup>2</sup>	0.0020 kg/sm <sup>2</sup>	0.70	0.70
<b>Roofs</b>		0.0002 kg/sm <sup>2</sup>	0.00015 kg/sm <sup>2</sup>	0.70	0.70

The wind pressure is determined by Bernoulli's equation and is given by the following equation:

$$p_w = C_p \rho \frac{U_{ref}^2}{2} \quad (4)$$

Where

$p_w$  = wind surface pressure relative to static pressure in undisturbed flow [Pa]

$\rho$  = air density [kg/m<sup>3</sup>]

$U_{ref}$  = reference wind speed at local height [m/s]

$C_p$  = wind pressure coefficient

The wind pressure coefficient  $C_p$  is a function of location on the building envelope, wind direction and site exposure. Although EnergyPlus can introduce  $C_p$  values at any wind angle increment, the third party interface used in this study employs mean  $C_p$  values for each façade for eight different wind directions (N, E, S, W, NE, SE, SW, NW).  $C_p$  values can be explicitly defined in the input by the user, otherwise the software will use default values from the database provided by AIVC (1996). The user may also find  $C_p$  values on the European Standard for Ventilation in Buildings (EN 15242). For more detailed analysis, the user has the possibility to define the  $C_p$  values through CFD simulations for the case examined. The BES uses the mean  $C_p$  value for each façade and for eight wind directions in 45° increments [Figure 4].

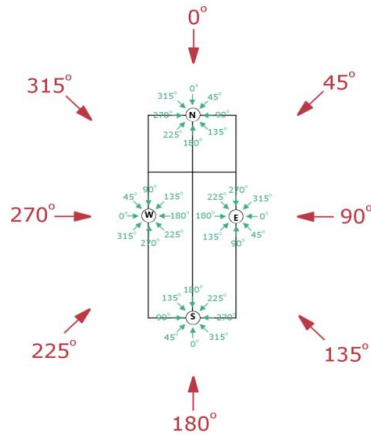


Figure 4. The eight wind directions in  $45^\circ$  increments that are used in the building energy simulation.  $0^\circ$  corresponds to North,  $90^\circ$  to East,  $180^\circ$  to South and  $270^\circ$  to West. For each façade, the surface-averaged  $C_p$  values are given for wind directions normal to the wall that is represented by the green arrows.

### 2.3.2 $C_p$ from database

The tables with the  $C_p$  data provided by AIVC (Orme, 1998) for low-rise buildings have been formed based on wind-tunnel measurements (AIVC, 1984) and several other literature studies (Bowen, 1976; Wiren, 1983). The  $C_p$  data are expressed as an average value for each façade of the building and for each  $45^\circ$  sector in wind direction. They include only two simple building geometries for square and rectangular surface plans, and for three rather generic sheltering conditions; exposed, partially sheltered (surrounded by obstructions equivalent to half the height of the building) and sheltered (building surrounded by obstructions equal to the height of the building). For the purpose of this study, the categories approximating better the two microclimatic cases were chosen.



### 2.3.3 $C_p$ from CFD simulations

In this study, the wind pressure coefficients for the building energy simulation of the reference building are calculated through the widely used open-source software OpenFOAM, which has been validated with both on-site measurements and wind-tunnel experimental data (Gartmann et al., 2011; Kubilay et al., 2014).

The wind pressure coefficients were calculated for both cases of microclimate for the reference building (exposed/sheltered) through both CFD tools. The  $C_p$  values were calculated for eight different wind directions (N, S, E, W, NE, SE, NW, SW), and an average value for wind pressure coefficient was defined for each façade of the building.

All the CFD simulations were performed at a simple mobile working station. The computational time for each direction of the exposed microclimatic case was approximately 2 hours, while the corresponding time for the sheltered microclimatic case was around 3 hours.

#### 2.3.3.1 CFD simulations on OpenFOAM

In the case examined, the steady Reynolds-averaged Navier-Stokes (RANS) equations were employed for determining the wind pressure variations on the reference building (Versteeg and Malalasekera, 2007). Montazeri and Blocken (2013) have evaluated the use of steady RANS equations for predicting mean wind pressure distributions on buildings and validated it with wind-tunnel experiments, and found that it is a suitable method, which provides good accuracy for different building geometries. The three-dimensional steady RANS equations are solved in combination with the standard  $k-\epsilon$  turbulence model. The  $k-\epsilon$  turbulence model is one of the most commonly used two-equation turbulence models in CFD for engineering problems. However, for dense urban typologies enhanced CFD models can capture the air flow characteristics among buildings with higher accuracy (Shirzadi et al., 2018; Shirzadi et al., 2019).

The Semi-Implicit Method for Pressure Linked Equations (SIMPLE algorithm) was used for the velocity-pressure coupling (Patankar and Spalding, 1972; Versteeg and Malalasekera, 2007). Second-order discretization schemes were used for both the convection and viscous terms of the governing equations. The GaussVanLeer (Van Leer, 1974) and the Gauss linear numerical schemes were selected for the convection and viscous terms correspondingly.

Furthermore, standard wall functions were employed for the ground and building surfaces based on their roughness. Turbulence models, such as the k- $\epsilon$ , are only valid for the area where turbulence is fully developed and they do not perform well in the near-wall region. Wall functions can model the near wall region and they are used to bridge the inner region between the wall and the fully turbulent area (Liu, 2016).

Also, vertical profiles for the mean velocity  $U$ , turbulent kinetic energy  $k$  and dissipation rate  $\epsilon$  were defined as boundary conditions. The velocity profile was a logarithmic wind profile where the roughness class and length of the area around the reference building was taken into consideration based on the following equation:

$$U_2 = U_1 \frac{\ln\left(\frac{h_2}{z_0}\right)}{\ln\left(\frac{h_1}{z_0}\right)} \quad (5)$$

Where  $U_1$  is the reference speed measured at height  $h_1$  and  $U_2$  is the wind speed at height  $h_2$ .  $z_0$  is the corresponding roughness length.

The vertical profiles for turbulent kinetic energy and dissipation rate were calculated based on the equations suggested by Richards and Hoxey (1993) and are given on Figure 5. For all vertical profiles, the roughness length  $z_0=0.4\text{m}$  that corresponds to suburban town was considered.

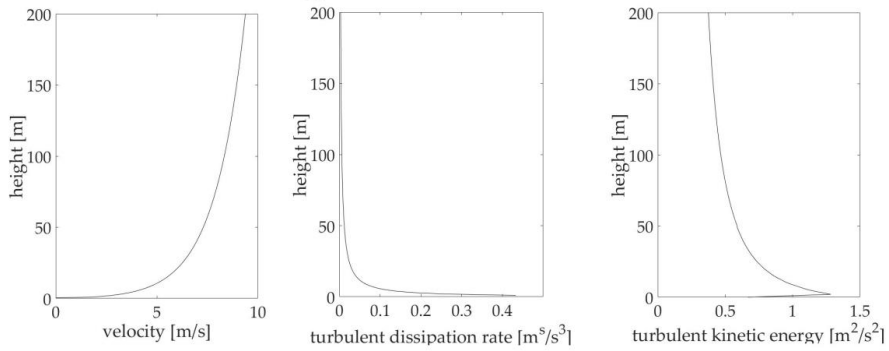


Figure 5. Inlet profiles used for the OpenFOAM simulations.

The mesh was created using the snappyHexMesh tool of OpenFOAM in combination with the blockMesh tool. The domain was defined through the blockMesh as a uniform mesh in all dimensions. The size of the domain was designed based on the Architectural Institute of Japan (AIJ) guidelines (Tominaga et al., 2008). The distance from the inlet and the lateral boundaries to the building was set at  $5H$ , the distance from the outlet to the building at  $10H$  and from the top boundary to the building at  $6H$ , where  $H$  is the height of the reference building. Three domain sizes for North ( $0^\circ$ ) wind, North-East ( $45^\circ$ ) and East ( $90^\circ$ ) are presented on Figure 6. The same domain sizes were used for the sheltered cases also. Subsequently, snappyHexMesh generates a 3-dimensional mesh containing hexahedra and split-hexahedra using the background hex mesh created by blockMesh, which defines the extent of the domain and a base level mesh. The mesh created is a hexahedral mesh with six refinement levels that get finer as approaching the building surfaces. The cell expansion ratio was set at 1 in order to avoid big aspect ratios that can compromise the convergence.

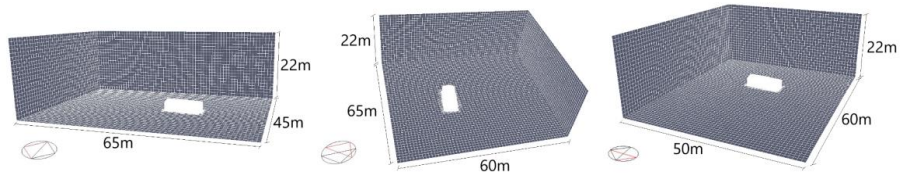


Figure 6. Domains created by OpenFOAM for a) North wind direction, b) North-East wind direction, and c) East wind direction. The black arrow points to the North, while the red arrow shows the wind direction.

A grid sensitivity analysis was carried out. A coarse, a basic and a fine mesh were created for North ( $0^\circ$ ) wind direction. The calculated surface pressures derived by the basic and coarse mesh differentiated by approximately 24%, while only 1.4% difference was noticed on the pressure variations between the basic and fine mesh. Therefore, the basic mesh's generating characteristics were used for the rest of the simulations. The  $y^+$  values were examined for every simulation in each wind direction in order to ensure that they remain inside the logarithmic area ( $30 < y^+ < 300$ ). The amount of grid cells varies among the different domains, but it is in the order of 2200000 to 3500000 cells for the exposed and sheltered microclimatic case correspondingly.

The convergence criteria taken into consideration were residuals values, solution imbalances and quantities of interest at monitor positions. The solutions converged approximately at maximum residual level of  $10^{-4}$  and with solution imbalances less than 1%, while the quantity of interest checked at monitor positions was the absolute pressure.

#### **2.4 Tracer gas measurements**

The air infiltration rate of the reference building was measured under windy conditions for both microclimatic cases (exposed/sheltered). The measurements took place inside

the insulated office space of the reference building, which is situated on the North side of the reference building.

Four measurements were performed when the building was completely exposed in open terrain, the dominant wind direction was North and the wind speeds were approximately at the level of 5 m/s. During the measurements, the wind speeds were recorded by the neighbouring meteorological station and correspond at height  $z = 10$  m above the ground. Additionally, four measurements were performed for the sheltered case, where the dominant wind direction was North-East and the wind speed was fluctuating between 4 to 5 m/s. Each measurement corresponds to approximately 3 to 5 hours of rather stable wind conditions and will be referred to the text as measurement 'Day'. The corresponding wind roses to each measurement ('Day') are presented in Figure 7.

The equipment used for the tracer gas measurements consisted of two CO<sub>2</sub> sensors ROTRONIC CP11, one manual extinguisher filled with CO<sub>2</sub> and one fan. ROTRONIC CP11 is a handheld instrument that simultaneously measures and records CO<sub>2</sub>, humidity and temperature, and it offers accuracy of  $\pm 30\text{ppm} \pm 5\%$  of measured value in the range of 0-5000 ppm. The CO<sub>2</sub> sensors have an automatic calibration function. An 'Outside Air Calibration' at 400 ppm was performed according to the manufacturer's guidelines (CP11 – short instruction manual 2014).

The concentration test decay method was employed for measuring the average air infiltration rate of the reference building (ASTM-E741, 2006). A volume of CO<sub>2</sub> was distributed uniformly in the interior of the building office space with the use of the fire extinguisher and the fan, and the two CO<sub>2</sub> loggers were monitoring the concentration of the tracer gas inside the building with a time interval of 15 seconds. The highest concentration recorded was approximately 5000 ppm and it was later stabilized at

approximately 400 ppm. At each time step, the normalized concentration  $C_N$  was calculated based on the following equation:

$$C_N = \frac{C(t) - C_o}{C(0) - C_o} \quad (7)$$

Where

$C(t)$  = tracer gas concentration in given time [ppm]

$C_o$  = tracer gas concentration outdoors [ppm]

$C(0)$  = tracer gas at first time step [ppm]

The regression model (ASTM-E741, 2006) was used to obtain the average air changes, using the equation below:

$$\ln C_N = -At + \ln C_N(0) \quad (8)$$

Performing a regression of  $\ln C_N$  against time  $t$  will give a fit line, whose slope represents the average infiltration rate [Figure 8]. The average air change rate corresponding to each measurement, as well as the confidence intervals representing the dispersion of the CO<sub>2</sub> concentration around the fit lines (using 99% confidence level), are given on Table 3.



Figure 7. Wind roses depicting the variation of the wind direction angle during each measurement – ‘day’

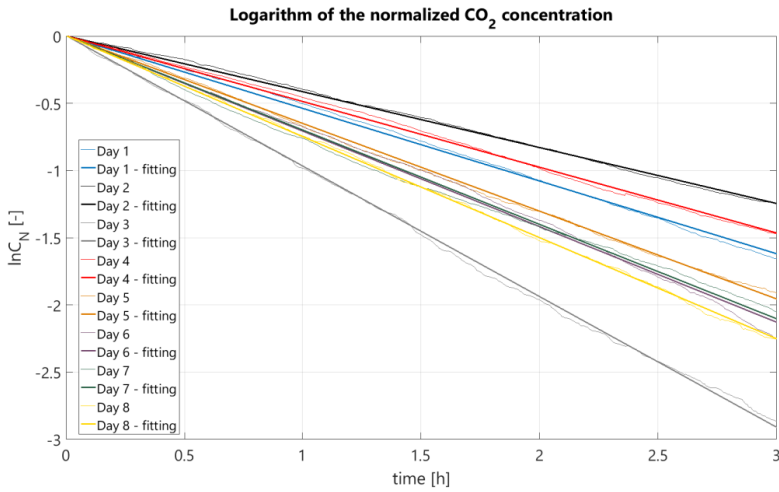


Figure 8. Logarithm of the normalized CO<sub>2</sub> concentrations C<sub>N</sub> at the reference building versus the elapsed time since the start of decay

Table 3. Average infiltration rates measured by the CO<sub>2</sub> decay method at the reference building and their corresponding R-square value

	ACH	R <sup>2</sup>
Day 1	0.555 ± 0.0025	0.999
Day 2	0.427 ± 0.0016	0.990
Day 3	0.998 ± 0.0026	0.999
Day 4	0.502 ± 0.0021	0.998
Day 5	0.671 ± 0.0019	0.999
Day 6	0.730 ± 0.0046	0.995
Day 7	0.721 ± 0.0052	0.992
Day 8	0.772 ± 0.0014	0.999

### 3. Results

The air infiltration rate of the reference building was calculated by all three different methods that are described above and for the two different microclimates (exposed/sheltered). The actual weather data from the neighbouring weather station was used during the building energy simulations. The building energy simulation was



performed with a time step of 30 minutes and the calculated air infiltration rate corresponds to the averaged infiltration rate for the exact 3-5 hours of each corresponding measurement ‘Day’. The calculated infiltration rates were compared with the corresponding measured air changes in order to evaluate the accuracy of each method.

The air infiltration rates calculated for the reference building are presented on Figure 9 and Figure 10 for the two different microclimates correspondingly. In both figures, the calculated air infiltration rates are compared with the measured values by the CO<sub>2</sub> decay method. The corresponding wind roses for each measurement are given on Figure 7. It is obvious that for both microclimatic cases, the air infiltration rates calculated using building-specific wind pressure coefficients from CFD simulations are closer to the actual air changes of the reference building.

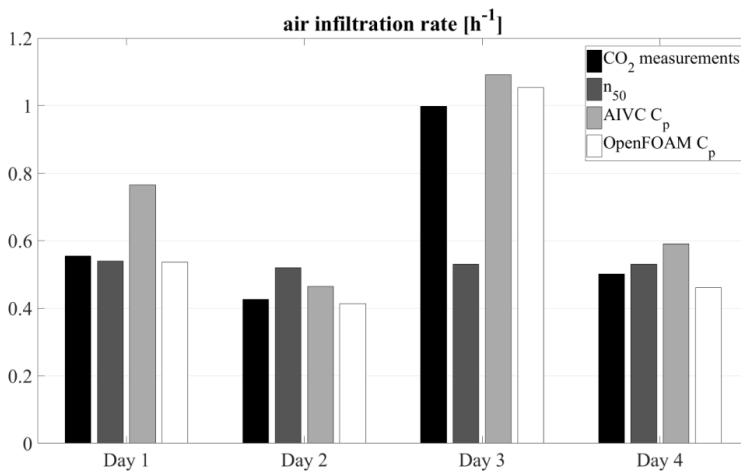


Figure 9. Measured and calculated air infiltration rates for the exposed microclimate.

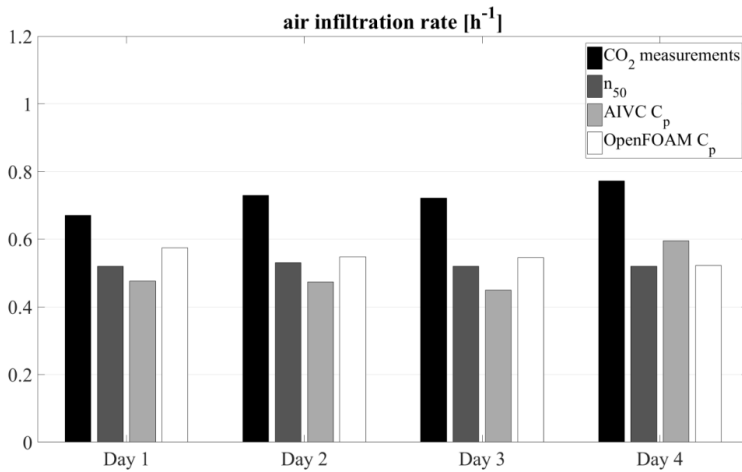


Figure 10. Measured and calculated air infiltration rates for the sheltered microclimate.

The use of the air leakage number  $n_{50}$  gives similar results for all eight days of measurements and fails to capture any microclimate effect. Although the shielding truck is included on the BES simulation for the sheltered case, the calculated air infiltration fluctuates around  $0.52 \text{ ach}^{-1}$  for all eight days of measurements. As a result, the use of the measured air leakage number  $n_{50}$  is able to predict reasonable infiltration rates only for the totally exposed microclimatic case and predicts even lower air changes for the sheltered case. It is necessary to highlight that the  $n_{50}$  number used was measured by a blower door test. Indicatively, it is mentioned that the representative air leakage number  $n_{50}$  from the national standard based on the building characteristics would be equal to  $4.0 \text{ h}^{-1}$ , while the measured is equal to  $8.17 \text{ h}^{-1}$ . The air infiltration results would drop approximately by 50% in the case that the estimated standard  $n_{50}$  was used, leading thus to a complete underestimation of the actual air changes.

The tabulated wind pressure coefficients provided by the AIVC (Orme 1998) give a crude approximation of the infiltration rate that in most cases is rather far from the

measured air changes. The results show that for the exposed case, the tabulated  $C_p$  values tend to overestimate the air infiltration on the reference building by an average 20%. On the other hand, the air infiltration rates for the sheltered case are significantly lower than the actual air changes. The tabulated  $C_p$  values predict from 20% to 35% lower air infiltration rates than the actual ones. These rough estimations can be explained by the fact that the  $C_p$  values from databases are not building-specific and represent very generic microclimatic conditions.

OpenFOAM was used to calculate the spatial wind-induced pressure variations on the reference building façades for each one of the eight wind directions that the BES software uses. Consequently, the  $C_p$  variations were determined based on Equation (4) for every façade and for all eight wind directions (N, E, S, W, NE, SE, SW, NW). The corresponding mean  $C_p$  values for each façade were used on the building energy simulations.

The spatial distribution of  $C_p$  values on the four façades of the reference building for wind normal to façade are presented below. Figure 11 presents the  $C_p$  variations on the building façades for the exposed microclimatic case. Contrary to  $n_{50}$ , that cannot account for the microclimate effect and requires the inclusion of the neighbouring buildings or obstacles on the BES, wind pressure coefficients are calculated based on the building's surroundings, thus they bear incorporated the information of the microclimatic conditions. Figure 12 shows the distribution of  $C_p$  values on the North and East façades of the reference building for both the exposed and the sheltered case for NE wind, calculated through OpenFOAM. It is reminded that the trailer used to provide shielding to the reference building during the measurements was situated 5 meters from the North – East corner of the reference building, providing thus shelter from NE wind [Figure 3].

It is obvious that the shielding effect of the trailer is captured both on the distribution of the wind pressure coefficients, as well as on the mean  $C_p$  value calculated for each façade.

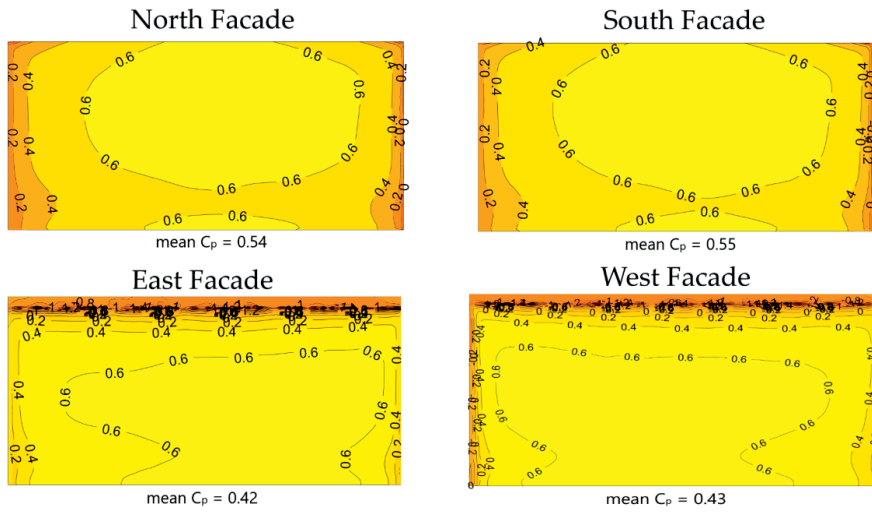


Figure 11.  $C_p$  variation on the four exposed building façades for wind direction normal to façade, calculated through OpenFOAM

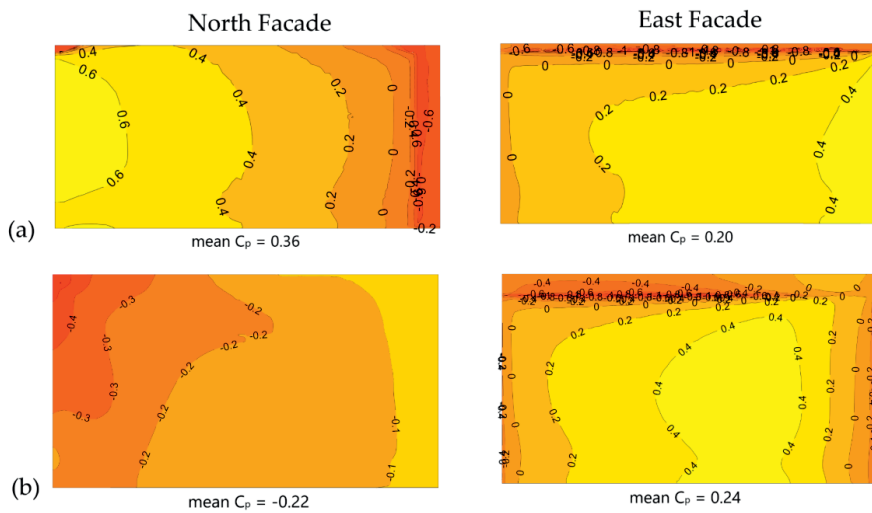


Figure 12.  $C_p$  variation on a) the exposed and b) the sheltered North and East building façades for wind direction of 45 degrees, calculated through OpenFOAM

Figures 11 and 12 show that CFD simulations can produce building-specific  $C_p$  values that carry rather accurately the microclimatic information based on the actual surroundings of the building. For example, the mean  $C_p$  value for the East façade of the exposed building is calculated at 0.42 from the CFD simulations, while the suggested AIVC database value is 0.50. The difference between building-specific  $C_p$  values and database  $C_p$  values is expected to be larger in complex building geometries, especially since databases provide  $C_p$  data only for simple geometries such as square or rectangular buildings. Furthermore, the building-specific mean  $C_p$  value for the sheltered North Façade of the reference building is calculated at the level of -0.22, while the suggested AIVC database value is 0.15 (Orme 1998). The generic nature of the shielding conditions in databases is not able to achieve the same accuracy as CFD calculated building-specific  $C_p$  values. Databases use broad shielding conditions, such as ‘building surrounded by obstructions equal to half the height or to the height of the building’, while CFD simulations can account for the actual surroundings of the building. As a result, building-specific wind pressure coefficients can hold more accurate microclimatic information related to the building examined.

OpenFOAM’s fine grid, with more than 20000 calculation nodes on each facade, makes it possible to calculate spatial pressure variations in detail. For example, although the building has practically South Orientation, it is slightly rotated by  $6^\circ$  towards the South – West direction and OpenFOAM is able to capture the slight shift of the maxima  $C_p$  from the center of the façade due to this  $6^\circ$  angle. Furthermore, OpenFOAM is able to capture the existence of negative pressure very closely to the eave.

The calculated  $C_p$  values from the CFD simulations are compared with the  $C_p$  values given by the AIVC, which seem to deviate from the results of CFD simulations for both microclimates examined.

Table 4. Surface-averaged  $C_p$  values for the exposed microclimatic case given by AIVC database and calculated through CFD simulations

Wind direction (normal to wall)	North Façade		East Façade		South Façade		West Façade	
	AIVC	OF	AIVC	OF	AIVC	OF	AIVC	OF
0°	0.6	0.54	0.5	0.42	0.6	0.55	0.5	0.43
45°	0.2	0.36	0.25	0.29	0.2	0.36	0.25	0.27
90°	-0.9	-0.54	-0.5	-0.2	-0.9	-0.51	-0.5	-0.21
135°	-0.6	-0.26	-0.8	-0.34	-0.6	-0.26	-0.8	-0.33
180°	-0.35	-0.09	-0.7	-0.24	-0.35	-0.09	-0.7	-0.25
225°	-0.6	-0.24	-0.8	-0.32	-0.6	-0.23	-0.8	-0.32
270°	-0.9	-0.34	-0.5	-0.28	-0.9	-0.36	-0.5	-0.28
315°	0.2	0.19	0.25	0.2	0.2	0.19	0.25	0.22

Table 5. Surface - averaged  $C_p$  values for the sheltered microclimatic case given by AIVC database and calculated through CFD simulations

Wind direction (normal to wall)	North Façade		East Façade		South Façade		West Façade	
	AIVC	OF	AIVC	OF	AIVC	OF	AIVC	OF
0°	0.4	0.53	0.25	0.59	0.4	0.57	0.25	0.48
45°	0.2	-0.22	0.06	0.31	0.2	0.38	0.06	0.27
90°	-0.6	-0.14	-0.35	-0.13	-0.6	-0.48	-0.35	-0.19
135°	-0.5	-0.27	-0.6	-0.32	-0.5	-0.26	-0.6	-0.18
180°	-0.3	-0.07	-0.5	-0.27	-0.3	-0.06	-0.5	-0.24
225°	-0.5	-0.2	-0.6	-0.34	-0.5	-0.23	-0.6	-0.33
270°	-0.6	-0.47	-0.35	-0.24	-0.6	-0.35	-0.35	-0.26
315°	0.2	0.21	0.06	0.24	0.2	0.19	0.06	0.24

The Root Mean Square Error (RMSE) (Chai and Draxler, 2014), between the predicted air infiltration rates and the corresponding measured rates, was calculated for

each one of the four methods examined. Table 6 shows that the use of  $C_p$  values from CFD simulations produces the lowest calculation error, as they manage to introduce more accurately the microclimatic boundary conditions. The database  $C_p$  values correspond to the high computational error due to their generic nature. The air leakage number seems to predict air infiltration rates with the highest error even though it has been measured on-site and is not national standard dataset based. The use of measured leakage number does not introduce any microclimatic conditions, can potentially be sufficient only post-construction and cannot contribute in predicting accurately the energy demands during the design phase of a building. Consequently, the results indicate that the use of building-specific wind-pressure coefficients, calculated through CFD simulations, have the potential to account for the microclimate on the building energy simulation and subsequently contribute into predicting more accurate air infiltration rates compared to conventional methods.

Table 6. RMSE of the BES simulations using the three different methods compared to the tracer gas measurements

	$n_{50}$	AIVC $C_p$	OpenFOAM $C_p$
<b>Exposed</b>	0.239	0.125	0.037
<b>Sheltered</b>	0.204	0.229	0.184
<b>Total</b>	0.222	0.184	0.133

#### 4. Discussion

Measurements have shown that the use of building-specific  $C_p$  values as input on BES predicts more accurately the air infiltration rates of a building with respect to its microclimate. The air leakage number  $n_{50}$  gives only a mere approximation of the air infiltration rate and fails to capture any microclimatic effect. Especially, during design phase where the actual air leakage number of a building cannot be measured but only estimated, the predicted air infiltration rates can radically deviate from reality.

Even though the reference building consists a simple geometry with low building height, the use of wind pressure coefficients during the building energy simulation have a clear impact on the prediction of the air infiltration rate of the building. A predefined  $C_p$  database can give a good first level approximation for basic design purposes, but fails to introduce precisely the microclimatic boundary conditions. Overall, the results indicate that the tabulated  $C_p$  values tend to overestimate the air infiltration of exposed buildings and underestimate the air infiltration of sheltered buildings. Furthermore, in cases where the building and/or sheltering conditions are not described by the offered database categories, such as in the sheltered case of the reference building, the user must select values from the most similar category, introducing thus non-representative wind pressure coefficients into the BES, which can potentially lead to non-realistic air infiltration rates.

However, the use of building-specific  $C_p$  values seems that can adequately introduce the local microclimatic conditions into the building energy simulation, leading thus to more realistic air infiltration rates. The results indicate that building-specific wind pressure coefficients, and not databased  $C_p$  values, are more appropriate input variable towards the correct estimation of building air infiltration, even for low-rise buildings. It is likely that the use of building-specific  $C_p$  values will have greater significance for the correct estimation of air infiltration of high-rise buildings and buildings with complicated architecture. In cases of big-scale and complex buildings, surface-averaged  $C_p$  values can lead to uncertainties on the calculation of air infiltration and local  $C_p$  values with high spatial resolution is preferable (Costola et al., 2010). The determination of building-specific  $C_p$  values comes with such spatial resolution. Consequently, local  $C_p$  values can be determined and attributed in detail to every different building component, thus accounting for the microclimatic conditions and increasing the accuracy of the calculated air infiltration rates.



Although CFD simulations remain a complicated and time-consuming task, 50 years of development and advancements have established them as a norm for both research and practice. Nowadays, plenty of research work and guidelines can help the user to define their set of equation, turbulence models, numerical schemes, boundary conditions, domain size and resolution. Therefore, the determination of building-specific  $C_p$  values is facilitated and the coupling of CFD with BES gives the possibility of more accurate prediction of energy demands. Furthermore, the integration of CFD pre-processing on BES software under a more user-friendly interface has been under development the past decade. It is expected that the integration of CFD pre-processing into BES will facilitate even more the determination of building-specific wind pressure coefficients for BES applications with regards to microclimate, and make the coupled CFD/BES method more attractive to engineers and energy consultants.

## **5. Conclusion**

The use of building-specific  $C_p$  values as input to the building energy simulations was shown to be the most accurate of three methods ( $n_{50}$ , tabulated  $C_p$ ,  $C_p$  from CFD simulations) in predicting the air infiltration of a building with respect to microclimate. Building-specific wind pressure coefficients are able to capture the microclimatic conditions of a building based on its geometry and surroundings. The use of CFD is a prerequisite for the correct determination of building-specific wind pressure coefficients. The coupling between CFD pre-processing and BES post-processing gives the opportunity of sufficiently introducing the microclimatic boundary conditions of a building through its building-specific wind pressure coefficients, and can lead to more accurate prediction of air infiltration rates and, subsequently to more accurate estimation of energy demands.

## References

- Air Infiltration and Ventilation Center. (1984). *Wind pressure workshop proceedings AIC-TN-13* p. 1-84
- Allegrini, J., Dorer, V. and J. Carmeliet. (2012). Influence of the urban microclimate in street canyons on the energy demand for space cooling and heating of buildings. *Energy and Buildings*, 55, 823-832
- Allegrini, J., J. Kampf, V. Dorer and J. Carmeliet. 2013. Modelling the urban microclimate and its influence on building energy demands of an urban neighbourhood. *Proceedings of CISBAT 2013 Cleantech for Smart Cities and Buildings II* (pp. 867-872)
- American Society for Testing and Material. (2006). *International E741-06. Standard test method for determining air change in a single zone by means of a tracer gas dilution*
- American Society of Heating, Refrigerating and Air-Conditioning Engineers. (2005). *ASHRAE Handbook – Fundamentals*. Atlanta, GA, USA
- Asfour, O.S. and M.B. Gadi. (2007). A comparison between CFD and Network models for predicting wind-driven ventilation in buildings. *Building and Environment*, 42, 4079-4085
- ASTM (American Society for Testing and Material). 2010. *International E779-10. Standard Test Method for Determining Air Leakage Rate by Fan Pressurization*
- Barbason, M. and S. Reiter. (2014). Coupling building energy simulation and computational fluid dynamics: Application to a two-storey house in temperate climate. *Building and Environment*, 75, 30-39
- Blocken, B., T. Stathopoulos and J. Carmeliet. (2007). CFD simulation of the atmospheric boundary layer: wall function problems. *Atmospheric Environment*, 41(2), 238-252
- Boujér, J., C. Inard and M. Musy. (2011). Microclimatic coupling as a solution to improve building energy simulation in an urban context. *Energy and Buildings*, 43, 1549-1559
- Bowen, J.J. (1976). A wind tunnel investigation using simple building models to obtain mean surface wind pressure coefficients for air infiltration estimates (NRC Report LTR-LA-209). *National Research Council*. Canada

- Chai, T. and R. R. Draxler. (2014). Root mean square error (RMSE) or mean absolute error (MAE)? – Arguments against avoiding RMSE in the literature. *Geoscientific Model Development*, 7, 1247-1250
- Charisi, S., Waszczuk, M. and Thiis, T.K. (2017). Investigation of the pressure coefficient impact on the air infiltration in buildings with respect to microclimate. *Energy Procedia*, 122, 637-642
- Costola, D. and M. Alucci. (2007). Pressure coefficient simulated by CFD for wind-driven ventilation analysis. *Proceedings Building Simulation* (pp. 999:1006)
- Costola, D., B. Blocken and J. L. M. Hensen. (2009). Overview of pressure coefficient data in building energy simulation and airflow network programs. *Building and Environment*, 44, 10:2027-2036
- Costola, D., B. Blocken and J. L. M. Hensen. (2009). Overview of the pressure coefficient data in building energy simulation and airflow network programs. *Building and Environment*, 44(10), 2027-2036
- Costola, D., Blocken, B., Ohba, M. and J.L.M. Hensen. 2010. Uncertainty in airflow rate calculations due to the use of surface-averaged pressure coefficients. *Energy and Buildings*, 42(6), 881-888
- Djunaedy, E., Hensen, J.L.M. and M.G.L.C. Loomans. (2005). External Coupling between CFD and Energy Simulation: Implementation and Validation. *ASHRAE Transactions*, 111, 612-624
- EN 12831 (European Standard). (2003). *Heating systems in buildings – Method for calculation of the design heat load*
- EN 15242 (European Standard). (2007). *Ventilation for Buildings – Calculation methods for the determination of air flow rates in buildings including infiltration*
- EnergyPlus™ Documentation. (2017). Engineering Reference: The Reference to EnergyPlus Infiltration/Ventilation Calculations. *U.S. Department of Energy*
- European Commission. (2010). Directive 2010/31/EU of the European Parliament and of the Council of 19 May 2010 on the energy performance of building (recast). *Official Journal of the European Union*, L 153/3
- European Commission. (2012). Directive 2012/27/EU of the European Parliament and of the Council of 25 October 2012 on energy efficiency, amending Directives 2009/125/EC and 2010/30/EU and repealing Directives 2004/8/EC and 2006/32/EC. *Official Journal of the European Union*, L 315/1

- European Commission. (2018). Directive (EU) 2018/844 of the European Parliament and of the Council of 30 May 2018 amending Directive 2010/31/EU on the energy performance of buildings and Directive 2012/27/EU on energy efficiency. *Official Journal of the European Union*, L 156/75
- Fan, Y. and K. Ito. (2012). Energy consumption analysis intended for real office space with energy recovery ventilator by integrating BES and CFD approaches. *Building and Environment*, 52, 57-67
- Gartmann, A., W. Fister, W. Schwanghart and M. D. Muller. (2011). CFD modelling and validation of measured wind field data in a portable wind tunnel. *Aeolian Research*, 3(3), 315-323
- Haghighat, F., H. Brohus and J. Rao. (2000). Modelling air infiltration due to wind fluctuations – a review. *Building and Environment*, 35, 377-385
- Hirt, C. W. and J. L. Cook. (1972). Calculating three-dimensional flows around structures and over rough terrain. *Journal of Computational Physics*, 10, 324-340
- Kraniotis, D., T. Aurlien and T. K. Thiis. (2014). Investigating Instantaneous Wind-Driven Infiltration Rates using the CO<sub>2</sub> Concentration Decay Method. *International Journal of Ventilation*, 13(2), 111-124.
- Kubilay, A., D. Derome, B. Blocken and J. Carmeliet. (2014). Numerical simulations of wind-driven rain on an array of low-rise cubic buildings and validation by field measurements. *Building and Environment*, 81, 283-295
- Liddament, M.W. (1986). Air infiltration Calculation Techniques – An applications Guide. *Annex V. AIVC*
- Liddament, M.W. (1996). A guide to energy efficient ventilation. *Annex V. AIVC*.
- Liu, F. 2016. A Thorough Description of How Wall Functions are Implemented in OpenFOAM. *Proceedings of CFD with OpenSource Software*
- Lyberg, M.D. (1997). Basic Air Infiltration. *Building and Environment*, 39(2), 95-100
- Malys, L., M. Musy and C. Inard. (2015). Microclimate and building energy consumption: study of different coupling methods. *Advances in Building Energy Research*, 9(2), 151-174
- Miyoshi, S., M. Ida and T. Miura. (1971). Wind pressure coefficients on exterior wall elements of tall building. *Wind Effects on Buildings and Structures*, 10, 273-284

- Mochida, A., Yoshino, H., Miyauchi, S. and T. Mitamura. (2006). Total analysis of cooling effects of cross-ventilation affected by microclimate around a building. *Solar Energy*, 80, 371-382
- Montazeri, H. and B. Blocken. (2013). CFD simulation of wind-induced pressure coefficients on buildings with and without balconies: validation and sensitivity analysis. *Building and Environment*, 60, 137-149
- Montazeri, H. and B. Blocken. (2013). CFD simulation of wind-induced pressure coefficients on buildings with and without balconies: Validation and sensitivity analysis. *Building and Environment*, 60, 137-149
- Moonen, P., Defraeye, T., Dorer, V., Blocken, B. and J. Carmeliet. (2012). Urban physics: Effect of the micro-climate on comfort, health and energy demand. *Frontiers of Architectural Research*, 1, 197-228
- Murakami, S. and A. Mochida. (1988). 3-D numerical simulation of airflow around a cubic model by means of the k- $\epsilon$  model. *Journal of Wind Engineering and Industrial Aerodynamics*, 31, 283-303
- Nearly Zero Energy Neighbourhoods (ZenN) project. 7<sup>th</sup> Framework Programme of the European Union. <http://www.zenn-fp7.eu/>
- Nikkho, S. K., M. Heidarinejad, J. Liu and J. Srebric. (2017). Quantifying the impact of urban wind sheltering on the building energy consumption. *Applied Thermal Engineering*, 116, 850-865
- Northumbria University. 2011. *An Inter-Program Analysis of Computational Fluid Dynamics Based on PHOENICS and DesignBuilder Software* (Report). Retrieved from <https://www.designbuilder.co.uk/download/documents>
- Nozu, T., T. Tamura, Y. Okuda and S. Sanada. (2008). LES of the flow and building wall pressures in the center of Tokyo. *Journal of Wind Engineering and Industrial Aerodynamics*, 96(10-11), 1762-1773
- Orme, M., Liddament, M.W. and A. Wilson. (1998). Numerical Data for Air Infiltration and Natural Ventilation Calculations. *Annex V. AIVC*
- Oxizidis, S., Dudek A.V. and N. Aquilina. (2011). Typical Weather Years and the Effect of Urban Microclimate on the Energy Behaviour of Buildings and HVAC Systems. *Advances in Building Energy Research*, 1, 89-103

- Patankar, S. V. and D. B. Spalding. (1972). A Calculation Procedure for Heat, Mass and Momentum Transfer in Three-Dimensional Parabolic Flows. *International Journal of Heat and Mass Transfer*, 15, 1787-1806
- Pisello, A. L., G. Pignatta, V. L. Castaldo and F. Cotana. (2015). The Impact of Local Microclimate Boundary Conditions on Building Energy Performance. *Sustainability*, 7, 9207-9230
- R. Priyadarsini. (2009). Urban Heat Island and its Impact on Building Energy Consumption. *Advances in Building Energy Research*, 3, 261-270
- Richards, P.J. and R.P. Hoxey. (1993). Appropriate boundary conditions for computational wind engineering models using the k- $\epsilon$  turbulence model. *Proceedings of the 1<sup>st</sup> International Symposium on Computational Wind Engineering* (pp.145-153)
- Richards, P.J., R.P. Hoxey and L.J. Short. (2001). Wind pressures on a 6m cube. *Journal of Wind Engineering and Industrial Aerodynamics*, 89, 1553-1564
- Rotronic AG. (2014). *CP11 – Handheld instrument for CO2, Humidity and Temperature – Short instruction manual*
- Shirzadi, M., Mirzaei, P.A. and M. Naghashzadegan. 2018. Modelling enhancement of cross-ventilation in sheltered buildings using stochastic optimization. *International Journal of Heat and Mass Transfer*, 118, 758-772
- Shirzadi, M., Mirzaei, P.A., Naghashzadegan, M. and Y. Tominaga, (2018). Modelling enhancement of cross-ventilation in sheltered building using stochastic optimization. *International Journal of Heat and Mass Transfer*, 118, 758-772
- Shirzadi, M., Naghashzadegan, M. and P.A. Mirzaei. (2018). Improving the CFD modelling of cross-ventilation in highly-packed urban areas. *Sustainable Cities and Societies*, 37, 451-465
- Shirzadi, M., Naghashzadegan, M. and P.A. Mirzaei. 2019. Developing a framework for improvement of building thermal performance modelling under urban microclimate interactions. *Sustainable Cities and Society*, 44, 27-39
- Shirzadi, M., Naghashzadegan, M. and P.A. Mirzaei.(2018). Developing a framework for improvement of building thermal performance modelling under urban microclimate interactions. *Sustainable Cities and Societies*, 44, 27-39

- SSB (Statistisk sentralbyrå – Statistics Norway). (2012). Energy and manufacturing: Energy consumption in households. <http://www.ssb.no/en/energi-og-industri/statistikker/husenergi/hvert-3-aar/2014-07-14#content>
- Stathopoulos, T. (1997). Computational wind engineering: Past achievements and future challenges. *Journal of Wind Engineering and Industrial Aerodynamics*, 67, 509-532
- Surry, D. (1991). Pressure measurements on the Texas Tech Building: Wind tunnel measurements and comparisons with full scale. *Journal of Wind Engineering and Industrial Aerodynamics*, 38, 235-247
- Tominaga, Y., A. Mochida, R. Yoshie, H. Kataoka, T. Nozu, M. Yoshikawa and T. Shirasawa. (2008). AIJ guidelines for practical applications of CFD to pedestrian wind environment around buildings. *Journal of Wind Engineering and Industrial Aerodynamics*. 96(10-11), 1749-1761
- Tominaga, Y., A. Mochida, S. Murakami and S. Sawaki. (2008). Comparison of various revised k- $\epsilon$  models and LES applied to flow around a high-rise building model with 1:1:2 shape placed within the surface boundary layer. *Journal of Wind Engineering and Industrial Aerodynamics*, 96, 389-411
- Toparlak, T., B. Blocken, B. Maiheu and G.J.F. van Heijst. (2017). A review on the CFD analysis of urban microclimate. *Renewable and Sustainable Energy Reviews*, 80, 1613-1640
- Tsoka, S., K. Tolika, T. Theodosiou, K. Tsikaloudaki and D. Bikas. (2017). A method to account for the urban microclimate on the creation of ‘typical weather year’ datasets for building energy simulation, using stochastically generated data. *Energy and Buildings*, 165, 270-283
- Uematsu, Y. and N. Isyumov. (1999). Wind pressures acting on low-rise buildings. *Journal of Wind Engineering and Industrial Aerodynamics*, 82, 1-25
- Van Leer, B. (1974). Towards the Ultimate Conservative Difference Scheme. II. Monotonicity and Conservation in a Second-order Scheme. *Journal of Computational Physics*, 14(4), 361-370
- Versteeg, H. K. and W. Malalasekera. (2007). *An Introduction to Computational Fluid Dynamics: The Finite Volume Method*. 2<sup>nd</sup> Edition. Pearson Education
- Walker, I.S. and D.J. Wilson. (2011). Field Validation of Algebraic Equations for Stack and Wind Driven Air infiltration Calculations. *HVAC&R Research*, 4, 119-139

- Wiren, B. G. (1983). Effects of surrounding buildings on wind pressure distributions and ventilation losses for single family houses. *Journal of Wind Engineering and Industrial Aerodynamics*, 15, 15-26
- Yang, T., N.G. Wright, D. Etheridge and A. Quinn. (2006). A comparison of CFD and full-scale measurements for analysis of natural ventilation. *The International Journal of Ventilation*, 4, 337-348
- Yi, Y.K and N. Feng. (2018). Dynamic integration between building energy simulation (BES) and computational fluid dynamics (CFD) simulations for building exterior surface. *Building Simulation*, 6, 297-308
- Younes, C., Shdid, C.A and G. Bitsuamlak. (2012). Air infiltration through building envelopes: A review. *Journal of Building Physics*, 35, 267-302
- Zhang, R., P.A. Mirzaei and B. Jones. (2018). Development of a dynamic external CFD and BES coupling framework for application of urban neighbourhoods energy modelling. *Building and Environment*, 146, 37-49



## Paper V

Article

# Full-Scale Measurements of Wind-Pressure Coefficients in Twin Medium-Rise Buildings

Stergiani Charisi \* , Thomas K. Thiis and Tormod Aurlien

Faculty of Science and Technology, Norwegian University of Life Sciences, 1432 Ås, Norway; thomas.thiis@nmbu.no (T.K.T.); tormod.aurlien@nmbu.no (T.A.)

\* Correspondence: stergiani.charisi@nmbu.no

Received: 15 February 2019; Accepted: 7 March 2019; Published: 12 March 2019



**Abstract:** Wind pressure coefficients ( $C_p$ ) are important values for building engineering applications, such as calculation of wind loads or wind-induced air infiltration and especially for tall buildings that are more susceptible to wind forces. Wind pressure coefficients are influenced by a plethora of parameters, such as building geometry, position on the façade, exposure or sheltering degree, and wind direction. On-site measurements have been performed on a twin medium-rise building complex. Differential pressure measurements have been employed in order to determine the wind pressure coefficients at various positions along the windward façades of the twin buildings. The measurements show that one building provides substantial wind shelter to its twin and the microclimatic effect is captured by the measured wind pressure coefficients. They also showed that the wind pressure coefficients vary significantly spatially along the windward façades of the medium-rise buildings. Furthermore, the pressure measurements showed that the wind pressure coefficients fluctuate significantly during the measuring period. The use of the fluctuating  $C_p$  values by means of probability distribution function (pdf) for the calculation of air infiltration has been evaluated. The results indicate that the air flows deriving using fluctuating  $C_p$  values are more accurate than the ones calculated by the conventional method of using mean  $C_p$  values.

**Keywords:** wind pressure coefficient; full-scale measurements; pressure measurements; air infiltration; microclimate

## 1. Introduction

Wind pressure coefficients,  $C_p$ , are non-dimensional coefficients that can express the wind-induced pressure at a specific position over a body, relative to the freestream wind pressure. Wind-pressure coefficients can be calculated through the following formula:

$$C_p = \frac{p - p_\infty}{\frac{1}{2}\rho U_\infty^2}, \quad (1)$$

where  $p$  is the pressure at the point of interest,  $p_\infty$  is the pressure in the freestream,  $\rho$  is the freestream air density, and  $U_\infty$  is the freestream wind velocity at the building height.

In building engineering, wind pressure coefficients are extensively used for the calculation of wind loads, as well as for the calculation of wind-induced air infiltration [1–4]. Especially for large-scale constructions that are more susceptible to wind forces, wind pressure coefficients are crucial to the correct estimation of wind loads and to their structural design [5,6].

Recent studies suggest that the use of building-specific wind-pressure coefficients can introduce the microclimate in building energy simulation (BES) and predict more accurately the wind-induced air infiltration [7,8]. However, the use of surface-averaged wind pressure coefficients seems to be

disadvantageous compared to the use of local  $C_p$  values with high spatial resolution [9–11]. Especially for medium- and high-rise buildings, where the  $C_p$  values can vary significantly along the vertical axis [12], the use of local  $C_p$  values may be more appropriate for BES.

Full-scale and wind-tunnel measurements are considered the most accurate methods in order to produce realistic wind pressure coefficients. During full-scale measurements, it is not necessary to reproduce boundary conditions, adopt physical models, or perform any downscaling. On the other hand, on wind-tunnel measurements, the approach-flow, including wind speed, direction, and turbulence, can be precisely managed by the user. Full-scale measurements are complicated, expensive, and time consuming. Similarly, wind tunnel measurements come with high cost and expertise. Full-scale measurements for the determination of the wind-induced pressures have been previously performed in low-rise buildings with simple geometries [13–15]. Data deriving from full-scale measurements have been also used for the validation of reduced-scale measurements, such as wind-tunnel testing, and showed agreement that renders wind-tunnel tests an invaluable tool for the determination of wind pressure coefficients [13–15]. Numerical analysis by means of computational fluid dynamics (CFD) simulations is usually employed for the determination of wind loads in cases of complicated structures, such as high-rise buildings and non-conventional architectural structures [16]. CFD simulations are considered complementary to the traditional means of full- and reduced-scale measurements and require proper knowledge and expertise in order to achieve high quality and reliability [17]. However, the most common sources of  $C_p$  values for BES applications are databases [1].

The wind pressure coefficients provided by databases, and that are employed by most BES tools for the calculation of air infiltration, are mean values that have been generated from a compilation of data coming from full-scale or wind-tunnel measurements [1]. The database provided by the Air Infiltration and Ventilation Center (AIVC) is based on wind-tunnel measurements and consists, until today, a valid reference used in BES [18]. However, the method that was used to convert these wind-tunnel data to database  $C_p$  values is not described in literature.

Studies suggest that the fluctuating wind pressures on buildings can have a significant impact on the air infiltration of buildings, with high gust incidents increasing significantly the total air changes [19–22]. In addition, the probabilistic and statistical characteristics of the wind pressure coefficients have been described and probability distribution functions (pdf) can be used to describe their fluctuating nature and capture their peak values [23]. Therefore, the use of fluctuating  $C_p$  values instead of the use of a calculated mean  $C_p$  value, might have a substantial impact on the calculation of air infiltration.

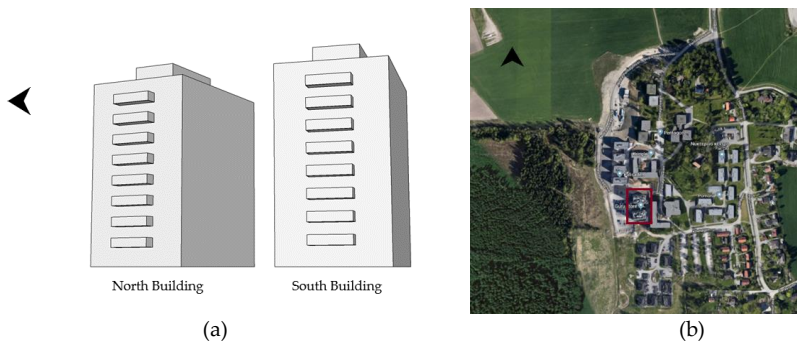
For the purpose of this study, full-scale measurements were performed in two twin medium-rise buildings. The measurements reveal the spatial variation of  $C_p$  values along the windward façades of the buildings. Furthermore, they capture the wind sheltering effect created in the case of a twin-building complex and, more specifically, the sheltering effect provided by one building to its twin. The use of fluctuating wind pressure coefficients for the calculation of air flow through an ideal crack is also investigated.

## 2. Methodology

### 2.1. Reference Buildings

For the purpose of this study, full-scale measurements were performed on the façades of a twin medium-rise building complex. The two identical buildings have the geometry of rectangular prism and they are oriented almost parallel to each other with an average distance of 12 m between them. The buildings' long axes are running East–West. The buildings were erected in 2013 and they are built with cross laminated timber (CLT). They consist of eight floors each and their height is approximately 25 m (Figure 1a).

The twin buildings are situated in the rural town of Ås, Norway. The buildings are surrounded by some low-rise buildings (2–4 storeys) and they are located next to a forest area (Figure 1b).

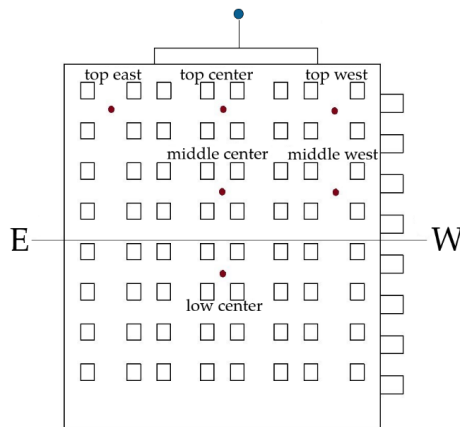


**Figure 1.** (a) Perspective view of the twin high-rise buildings; (b) Satellite picture of the building complex and its surroundings. The twin high-rise buildings are marked inside the red frame.

## 2.2. Measurements

Twelve SDP1000 low-range differential pressure sensors for air—six at each building—were used during the measurements (Figure 2). The sensors have a measurement range of  $-5$  to  $125$  Pa and they give high accuracy even below  $10$  Pa [24]. They also include a digital built-in temperature compensation circuit, thus rendering the measurements temperature independent. The pressure difference between the North façade (windward) and the reference pressure at the top of each of the twin buildings was measured simultaneously at both buildings.

All the reference pressure taps were placed at the same position at a height of approximately  $2.5$  m over the rooftop (Figure 2). The assumption that at this height the velocity vector has only a horizontal component is made. The pressure tap openings were placed parallel to the horizontal wind velocity vector. Therefore, the simplification that the pressure taps on the rooftops will only measure static pressure and not total pressure, since the velocity vector is parallel to the tap and will not increase the fluid's speed, is made. The simplification that the pressure measured over the rooftop is the same as the static pressure at the undisturbed free stream at building height is also made.

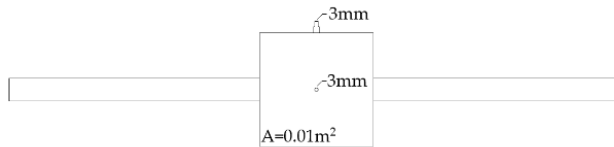


**Figure 2.** The positions of the pressure taps during the measurements. The red dots represent the pressure taps on the windward (North) façades of the twin buildings and the reference pressure taps at a height of  $\sim 2.5$  m over the rooftop are indicated by the blue dot.

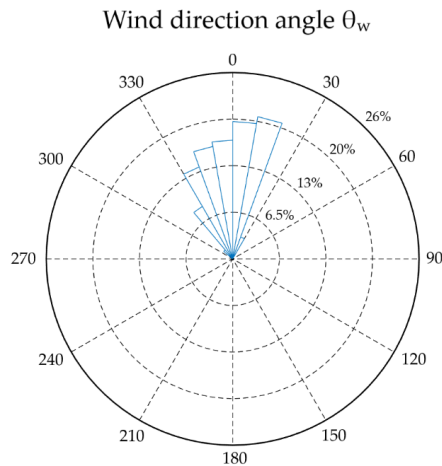
Six pressure taps were placed in three different heights at the windward façades of the buildings. They were placed at the top, middle, and low parts of the building and in three different lateral positions: One close to each edge of the building and one in the middle of the building (Figure 2). The pressure taps had a diameter of 3 mm and they were placed in the middle of a square plate with an area of  $0.01 \text{ m}^2$  in order to keep them perpendicular to the façade and also to reduce the turbulent flow around the tap nozzle (Figure 3). The pressure taps were connected with silicon tubes with a diameter of 3 mm to the differential pressure sensors according to the manufacturer's suggestions. On the pressure side, the tube lengths varied from 15 m to 25 m, while on the reference position the tubes were 7 m.

Summarizing, it is considered that the measured differential pressure gives the difference between the pressure  $P_x$  at the tap's position on the windward building façade and the static pressure  $P_0$  at the undisturbed wind flow at building height.

The pressure sensors were placed at the rooftops of the twin buildings. The data acquisition system was recording the instantaneous pressure difference values with a frequency of 5 Hz. The full-scale measurements lasted approximately one week, during which the dominant wind direction was North ( $0^\circ$ ) (Figure 4). Therefore, wind pressure coefficients for only the North ( $0^\circ$ ) direction were calculated.



**Figure 3.** Drawing of the pressure taps used for the measurements. The silicon tubes were connected to the top nozzle of 3 mm, which was connected with the 3 mm hole on the center of the square plate. The “flaps” on both sides were used to stabilize the pressure taps on the façade.



**Figure 4.** Wind direction measured at the local weather station during the measurement period. Only data that correspond to North wind direction ( $337.5^\circ < \theta_w < 22.5^\circ$ ) were used for the determination of the wind pressure coefficients in this study.

During the measurements, the wind speed and wind direction were monitored both by a weather station installed on the rooftop of one of the twin buildings and by the local meteorological station, which is situated approximately 600 m from the reference buildings. The weather station on the rooftop provided only 30-min averaged values, while the meteorological station gave 10-min averaged values

for wind speed and direction. The most frequent weather data were considered more appropriate for the correct calculation of the wind pressure coefficients. Therefore, a correlation between the two stations were established and the 10-min averaged values were corrected according to the following process in order to account for the local wind speed variations on the rooftop of the reference buildings.

The meteorological station is situated in the middle of an open field and the wind data were measured at a height of 10 m over the ground. Using the logarithmic wind profile [25], the wind speed at the reference building height ( $h_{ref} = 25$  m) was calculated based on the relevant roughness length ( $z_0 = 0.03$  m) that corresponds to open agricultural land, similar to the meteorological field. The logarithmic wind profile is described by the following equation:

$$u_2 = u_1 \frac{\ln\left(\frac{h_2}{z_0}\right)}{\ln\left(\frac{h_1}{z_0}\right)}, \quad (2)$$

where  $u_1$  is the reference wind speed at height  $h_1$ ,  $u_2$  is the wind speed at height  $h_2$ , and  $z_0$  is the roughness length depending on the land cover type.

Subsequently, the 30-min averaged wind speeds at a 25 m height over the meteorological field were calculated and compared with the corresponding 30-min averaged values given by the weather station at the rooftop of the twin buildings. A correction coefficient was determined for each one of 16 wind directions (N, NNE, NE, NEE, E, SEE, SE, SSE, S, SSW, SW, SWW, W, NWW, NW, NNW). The correction coefficients were applied to the 10-min averaged wind speeds from the local meteorological station at 25 m according to the wind direction. The corrected 10-min averaged data at 25 m over the meteorological field correspond to the 10-min averaged wind speeds at the reference building height and were used for the calculation of the  $C_p$  values based on Equation (1) (Figure 5). As a result, both freestream wind velocity and freestream pressure were theoretically measured at the same position over the rooftop of the reference buildings.

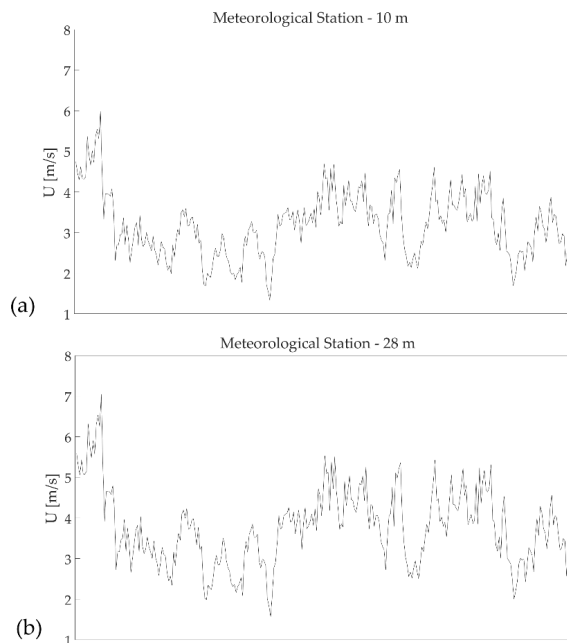
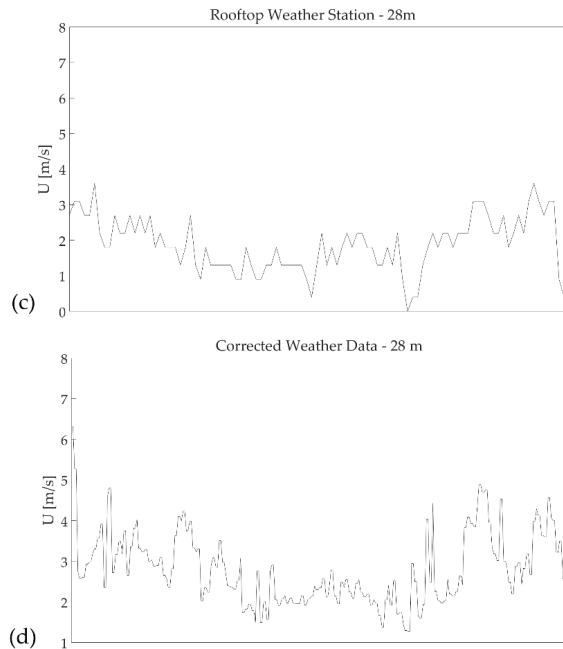


Figure 5. Cont.



**Figure 5.** Wind speeds (a) measured by the local meteorological station at a height of 10 m above the ground; (b) calculated at a height of 28 m above the ground based on the logarithmic wind profile; (c) measured by the weather station on the rooftop of the twin building; (d) corrected 10-min averaged at a height of 28 m above the ground.

### 2.3. Monte Carlo Simulations

The measurements showed that the measured wind pressure coefficients were fluctuating significantly during the measuring period. For the purpose of this study, both the use of fluctuating wind pressure coefficients and the use of the measured mean  $C_p$  values for the calculation of air infiltration were evaluated.

Since the wind pressure coefficients were measured only on the windward sides of the reference buildings, the impact of the  $C_p$  values on air infiltration was evaluated qualitatively, assuming an ideal gap of area of  $0.01 \text{ m}^2$ . In this case, the air flow can be represented by an equivalent flow through a flat orifice plate [18]. The orifice flow is given by the following equation:

$$Q = C_d A \sqrt{\frac{2}{\rho} \Delta P}, \quad (3)$$

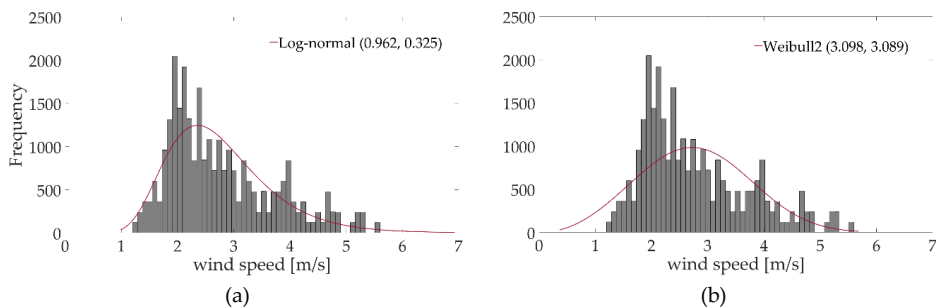
where  $Q$  is the air flow rate ( $\text{m}^3/\text{s}$ ),  $C_d$  is the discharge coefficient (in this study taken as equal to 1),  $\rho$  is the air density ( $\text{kg}/\text{m}^3$ ),  $\Delta P$  is the pressure difference across the opening (Pa), and  $A$  is the area of the opening ( $\text{m}^2$ ).

Combining the orifice equation and the defining equation for wind pressure coefficients, the air flow through the assumed ideal gap can be given by the following equation:

$$Q = A \cdot U_{wind} \cdot \sqrt{C_p}. \quad (4)$$

In order to evaluate the fluctuating  $C_p$  values with respect to air infiltration, the Monte Carlo method was employed [26–29]. Initially, the actual distribution of the measured wind pressure coefficients was determined and, after applying data fitting, it was found that the measured  $C_p$  values follow the logarithmic normal distribution [23]. The logarithmic normal distribution cannot include negative values, thus the measured negative wind pressure coefficients have been excluded. However, for all measuring positions, besides the Middle West, the amount of measured negative values is between 1% and 3%, which can be considered negligible. At the Middle West measuring position, the negative values make up 8% of the total measured wind pressure coefficients.

The wind velocities measured during the measuring period were used. Only wind directions within the angle range  $[-22.5^\circ, 22.5^\circ]$  that correspond to the North wind direction were selected. Similarly, it was found that the wind velocity distribution follows the logarithmic normal distribution (Figure 6). The Weibull distribution was also considered, but the logarithmic normal distribution captured better the frequency of the measured wind speeds (Figure 6). The log-normal distribution is generally considered a suitable distribution to describe the probability distribution of wind speed data [30–33].



**Figure 6.** Fitting of probability distributions to the measured wind speed data. (a) Logarithmic normal distribution; (b) Weibull 2 distribution.

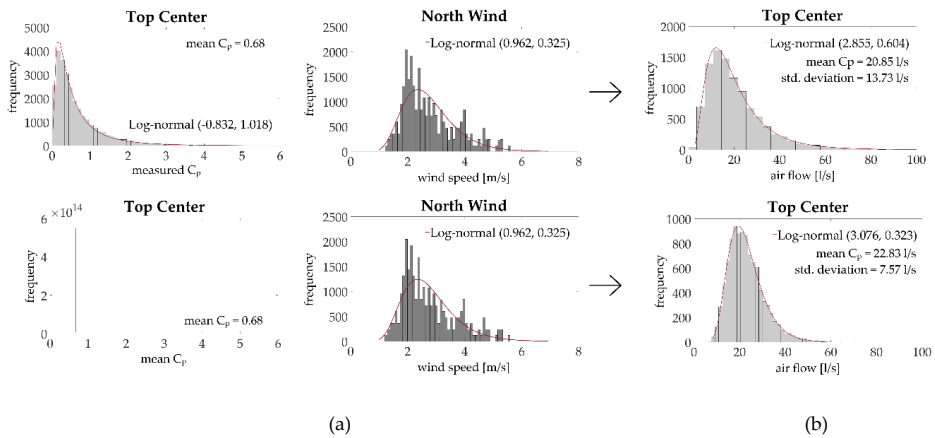
The Monte Carlo simulations repeat random sampling from the two log-normal distributions of wind pressure coefficients and wind velocities, and subsequently calculate the resulting air flow (Figure 7a). In order to define the required number of iterations for the Monte Carlo simulations, 50,000 iterations were performed and the sample average was plotted against the number of iterations. The results indicated that the simulations reach convergence after approximately 7000 iterations. Consequently, 10,000 iterations were performed for the Monte Carlo simulations that calculated the air infiltration in each one of the six measuring positions.

Furthermore, Monte Carlo simulations were also performed in order to define the air infiltration through the ideal gap using constant time-averaged  $C_p$  value (Figure 7b). In that case, the Monte Carlo simulation was used in order to randomly select values from the log-normal distribution of the wind velocities. For this case also, the total number of iterations performed was 10,000.

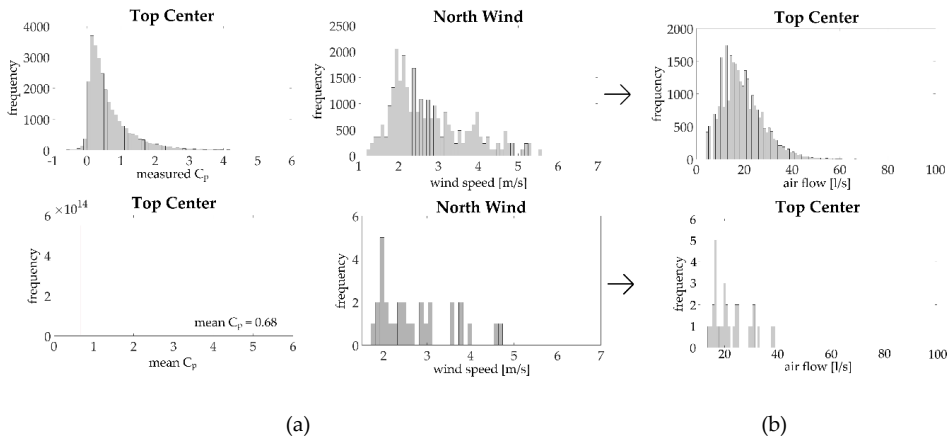
Furthermore, the air flows were calculated using the measured wind pressure coefficient and corresponding measured wind speed at each time step, and the actual air flow distribution at each measuring position was defined (Figure 8a). The Monte Carlo simulation results for both cases—using fluctuating  $C_p$  values and mean  $C_p$  value—were evaluated against the actual air flow distributions that were calculated using the measured wind pressure coefficients and measured wind speeds at each time step.

During building energy simulations, the air changes are calculated using mean  $C_p$  values and hourly wind data from typical meteorological year (TMY) files. Therefore, an additional air flow through the ideal gap was calculated using the mean  $C_p$  values in combination with hourly-averaged wind speeds for the North wind direction (Figure 8b).





**Figure 7.** Example of Monte Carlo simulations: (a) Using the probability distribution of measured  $C_p$  values; (b) using the time-averaged measured  $C_p$  value. The Monte Carlo method selects random value from the two distributions given and correlates them using the relevant formula in order to produce a random sample of results, which are later fitted in a third distribution.



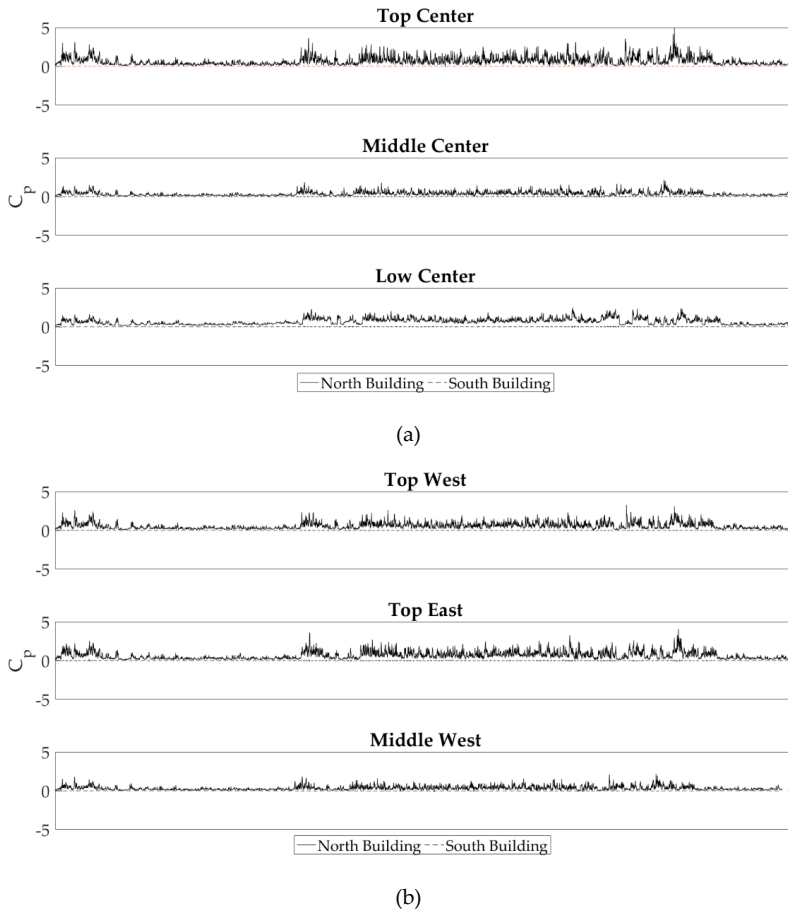
**Figure 8.** (a) Calculation of actual air flow distribution using the measured wind pressure coefficients in combination with the measured wind speeds for North direction ( $0^\circ$ ); (b) Calculation of the air flow distribution using mean  $C_p$  value in combination with hourly wind speeds.

### 3. Results

For the determination of the wind pressure coefficients on the North façades of the two reference buildings, only weather data that corresponded to North wind direction, and more specifically wind angles within the range of  $-22.5^\circ$  to  $22.5^\circ$ , were used (Figure 4). The wind pressure coefficients were calculated from Equation (1), using the differential pressure provided by the sensors and the corrected wind velocity at the building height. The air density was also calculated using the pressure, temperature and humidity values provided by the weather station.

Initially, the fluctuating differential pressure data obtained during the pressure measurements were smoothed and the “noise” due to the length of the silicon tubing used was filtered out by the means of moving average [34].

Figure 9 shows the measured wind pressure coefficients at the various measuring positions for both buildings. We remind that, during the measurements, the dominant wind direction was North (Figure 4). As it is expected, the North building, which is completely exposed to the impinging wind, presents high values of wind pressure coefficients on its windward façade. On the other hand, the South building that is protected by its twin from the incoming North wind develops no essential wind-induced pressure on its windward façade.



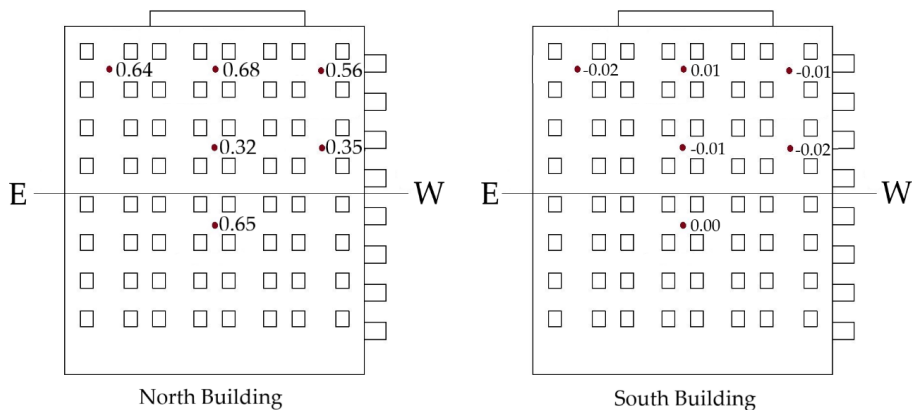
**Figure 9.** Measured pressure coefficients (a) at the center measuring positions and (b) at the edges.

Figure 10 presents the mean measured wind pressure coefficients at the measuring positions on both twin buildings.

The wind pressure coefficients calculated for the highest part of the North building have relatively the highest values, as it would be expected. The top center part is the most susceptible to wind pressure with a measured  $C_p$  value of 0.68. Both positions close to the edges present lower pressurization compared to the center of the building envelope and their measured  $C_p$  values are 0.64 and 0.56 for the East and West positions, correspondingly. It is interesting that, although the edge measuring positions are symmetrical to the center, they do not have similarly lower measured wind pressure coefficients compared to the center. In contrast, the middle part presents no essential variation between the center and the edge and both measured wind pressure coefficients are approximately at 0.34. However, it

is highly interesting that these middle positions are placed on the top half of the building but they deviate almost by half the measured values on the top part. More specifically, the middle measuring position is placed approximately 2/3 up the building, which is similar to the stagnation point position, where the wind-induced pressure is expected to be the highest. On the other hand, the mean measured  $C_p$  value on the low center position was calculated at 0.65. Consequently, and in contrast to what might be expected, i.e., the  $C_p$  values decreasing as the positions are moving lower across the vertical axis of the building, the measurements show that the highest wind pressure coefficients are measured both on the top and in the low measuring positions, while the lowest wind pressure coefficient is measured on the middle measuring position. This is probably the result of the surroundings' morphology, as the neighboring buildings can provide wind shelter to the middle measuring zone and other neighboring buildings or obstacles can create an upwind flow that causes the increased wind-induced pressure on the lower measuring zone. However, since no wind or turbulence measurements were performed on site, it can only be assumed that the particular pressure variation pattern along the building façade is the result of the microclimatic effect.

As it can be seen in Figure 10, all six mean measured coefficients on the South building are practically zero. Slightly over zero, with a  $C_p$  value of 0.01, is the wind pressure coefficient of the top center measuring position. The measured  $C_p$  values on all edge positions are slightly below zero, between  $-0.01$  and  $-0.02$ , probably due to the induced turbulence on the edges of the building. However, the measured  $C_p$  values on the two remaining center points (middle center and low center) of the South Building indicate that the turbulence developed in the passage between the twin buildings is negligible. The results show that for North wind, the South building is completely sheltered from the impinging wind by its twin North Building and no essential wind-induced pressurization is developed on its windward façade.

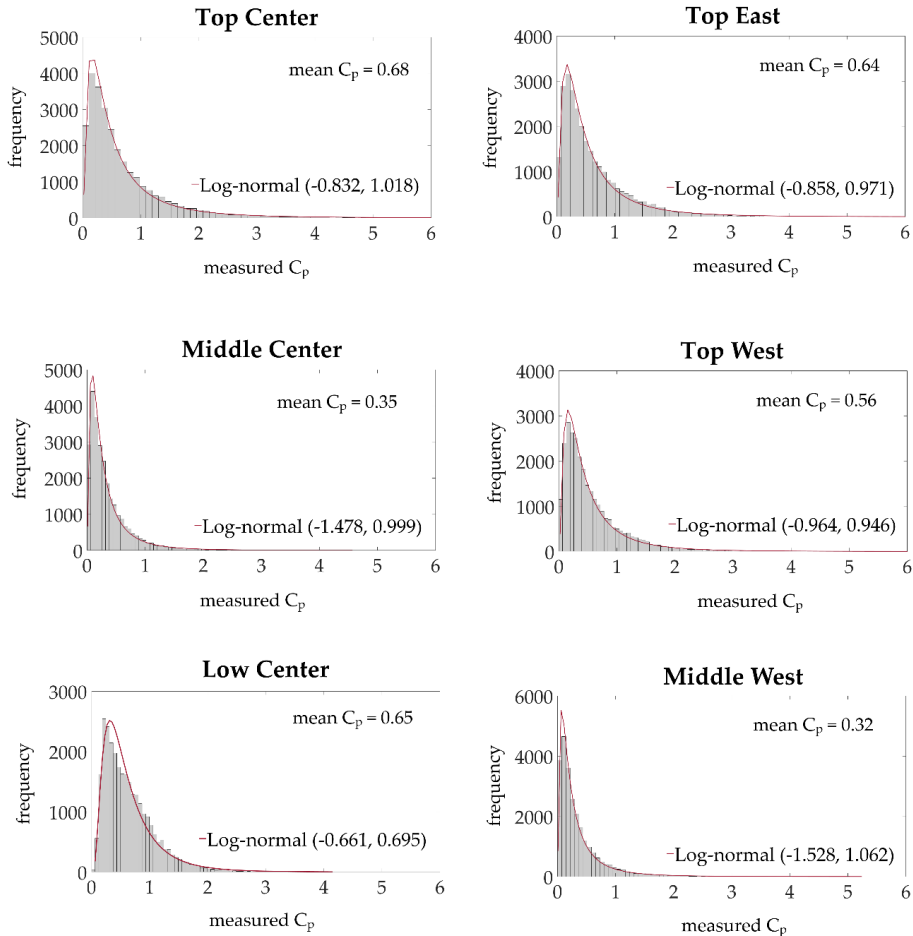


**Figure 10.** Measured wind pressure coefficients on the windward façades of the twin buildings for the North ( $0^\circ$ ) wind direction.

Figure 9 shows that the measured wind pressure coefficients fluctuate significantly during the whole measuring period for the windward façade of the exposed North building. Therefore, Monte Carlo simulations were performed in order to investigate the impact of fluctuating  $C_p$  values on the air infiltration calculation and to assess whether the use of the mean  $C_p$  values is sufficient. Since the measured wind pressure coefficients on the windward façade of the sheltered South building fluctuate slightly around 0.0, the Monte Carlo method was employed only for the windward façade of the exposed North building.

Figure 11 shows all the histogram distributions of the measured wind pressure coefficients on the windward façade of the exposed North building, along with their corresponding probability

distribution functions. It is interesting that in all measuring positions, the wind pressure coefficient distribution follows the logarithmic normal probability function, however, the findings regarding the probabilistic nature of the measured wind pressure coefficients are in accordance with previous study findings [23]. The probability distribution functions of the measured wind pressure coefficients were used in combination with the probability distribution function of wind speeds for the North direction by means of the Monte Carlo simulation, as described in Section 2.3.

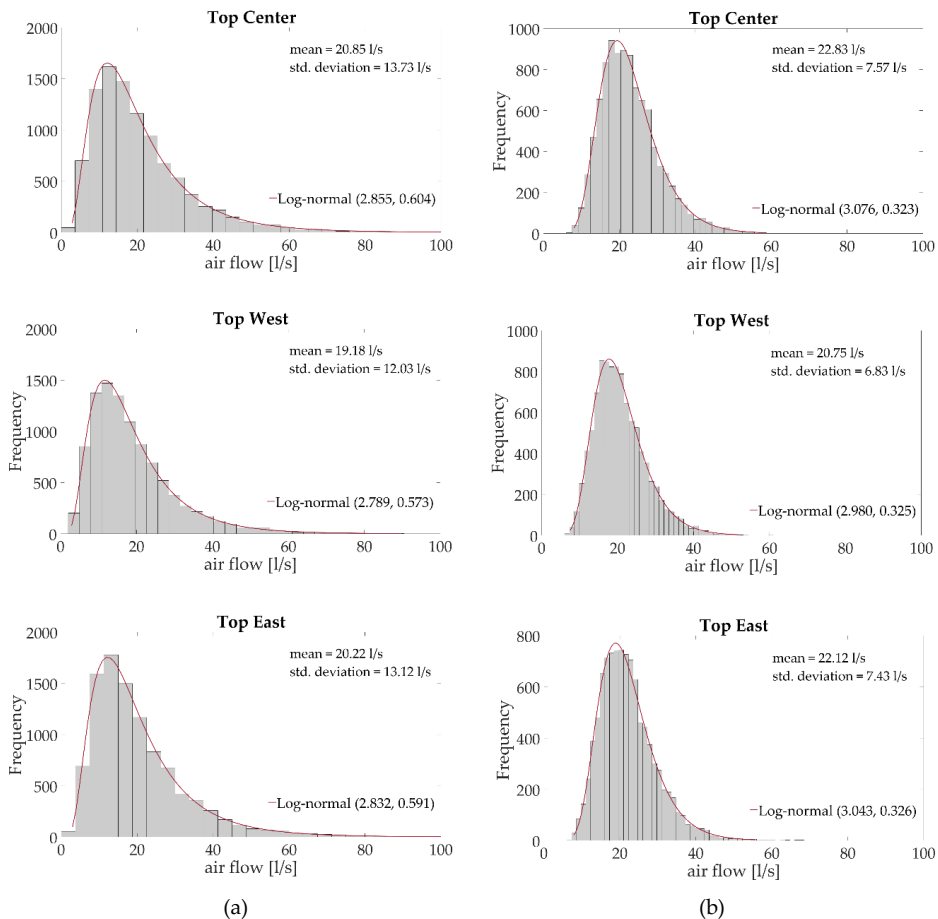


**Figure 11.** Distributions of measured  $C_p$  values on the six measuring positions on the windward façade of the exposed North building and their corresponding probability distribution functions used for the Monte Carlo simulations.

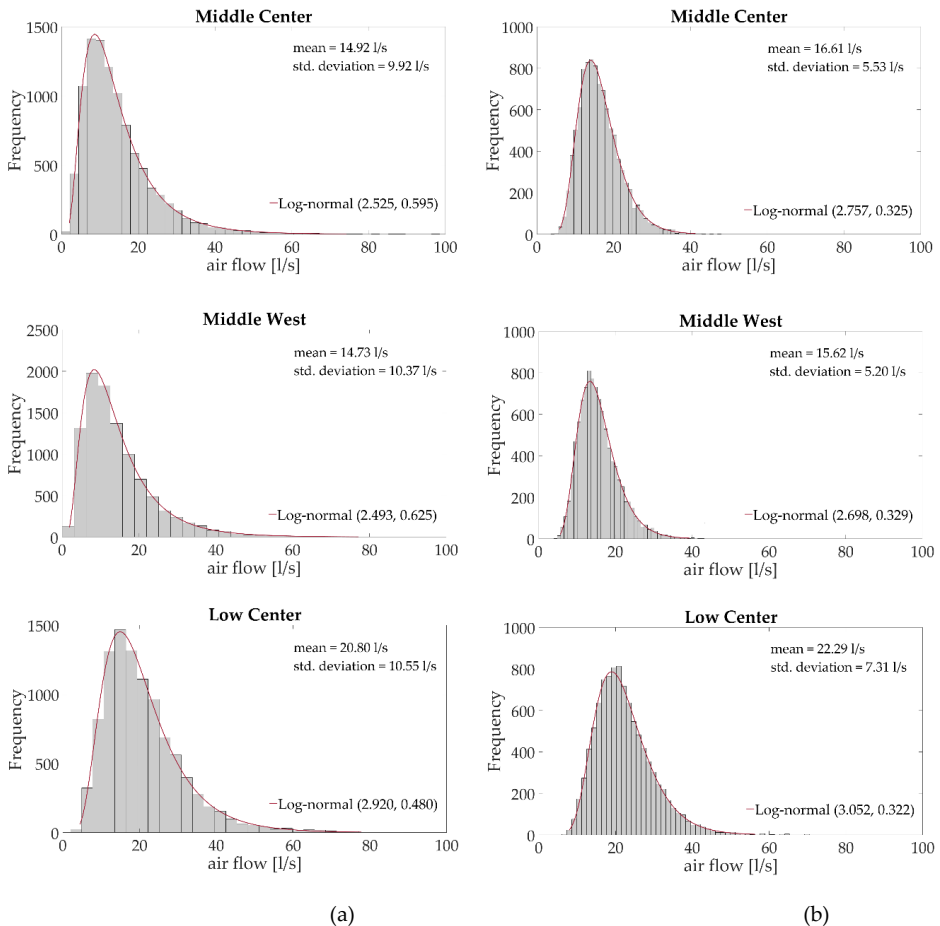
Figures 12 and 13 show the probability distributions of the air flows, calculated both using the probability distribution of measured  $C_p$  values and the constant mean  $C_p$  value. For both cases, all probability distributions are constructed at a confidence level of 95%, and they all follow the logarithmic normal distribution function. In all measuring positions, the log-normal distribution functions derived from fluctuating  $C_p$  values have a slightly higher parameter  $\sigma$  and a lower parameter  $\mu$ , which means that the corresponding density distribution is slightly more shifted toward the left side of the x-axis, compared to the density distribution of air flow derived from the constant mean  $C_p$ .

value. Although the resulting air flow probability distribution function (pdf) using mean  $C_p$  value will be closer to the peak value of the actual air flow rate, the air flow pdf resulting using fluctuating  $C_p$  values will always capture better the overall distribution of the air flows and produce a sample mean closer to the actual air flow mean (Figure 14).

Furthermore, for all measuring positions, the sample mean calculated using mean  $C_p$  values is always higher than the corresponding sample mean using fluctuating  $C_p$  values, while the sample standard deviation using mean  $C_p$  value is always lower than the corresponding one using fluctuating  $C_p$  values. The sample means differ between 4% and 10%, while the standard deviation differences vary from 1% to 30%. Overall, the results suggest that the use of mean  $C_p$  values tends to calculate larger air flows by approximately 7% in comparison to the mean air flow results given by using fluctuating  $C_p$  values. In both cases, the calculated air flow distributions follow similar logarithmic normal distribution.

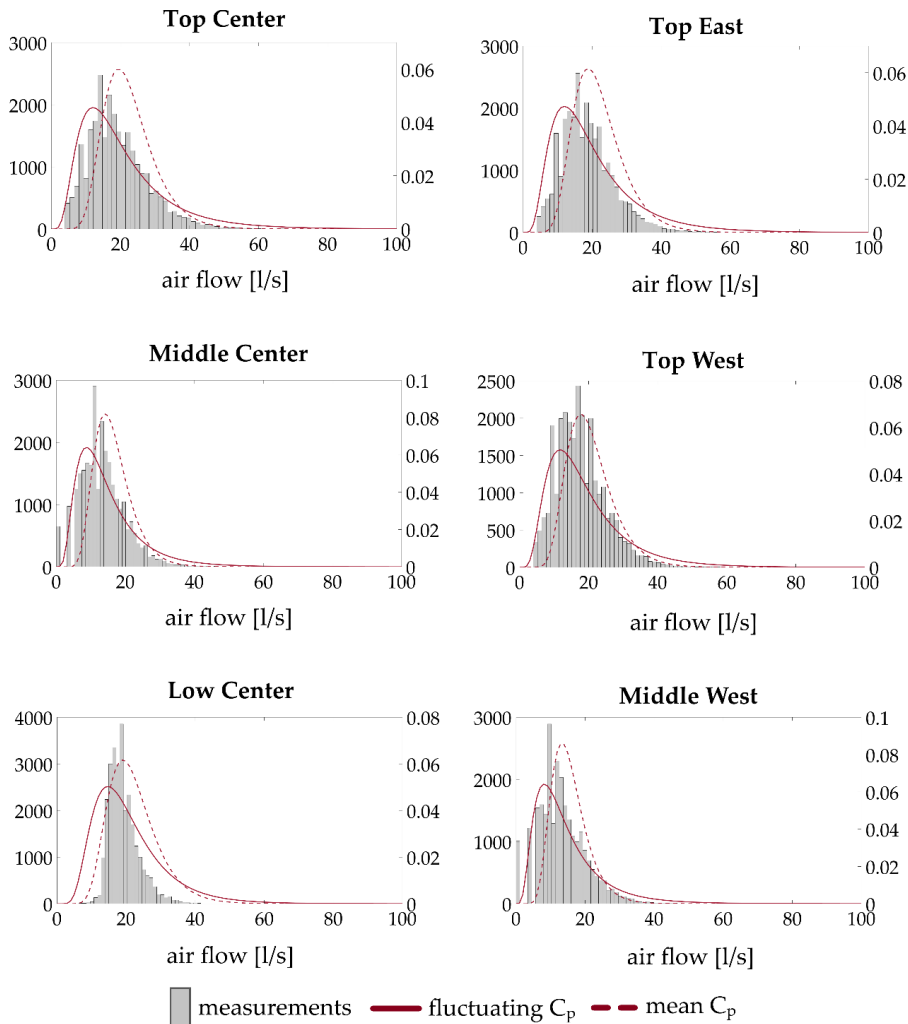


**Figure 12.** Probability distributions of calculated air flow through Monte Carlo simulations (a) using the probability distributions of the measured wind pressure coefficient; (b) using the mean measured wind pressure coefficient.



**Figure 13.** Probability distributions of calculated air flow through Monte Carlo simulations (a) using the probability distributions of measured wind pressure coefficient; (b) using the mean measured wind pressure coefficient.

The Monte Carlo results using both fluctuating and mean  $C_p$  values are also compared with the actual air flow distributions that are calculated using the measured wind pressure coefficients and measured wind speeds at each time step (Figure 14). Figure 14 shows that the statistical methods slightly overestimate the air flow regardless of the input considered for the  $C_p$  values (probability distribution of fluctuating  $C_p$  or mean  $C_p$ ), but overall, both resulting distributions seem to fit rather sufficiently with the measured data. During the Monte Carlo simulations, random values of the two distributions (wind pressure coefficient and wind speed) are combined in order to calculate the air flow. On the other hand, during the calculation of the actual air flow distribution, the measured wind pressure coefficient is combined with the corresponding measured wind speed at each time step in order to calculate the air flow and therefore, it is easier to capture the wind gust effect.



**Figure 14.** Distributions of calculated air flows based on measured  $C_p$  values and measured wind speeds on the six measuring positions on the windward façade of the exposed North building and the probability distribution functions of air flows calculated using fluctuating  $C_p$  values and mean  $C_p$  values through Monte Carlo simulations.

In all measuring positions, the use of the fluctuating  $C_p$  value on Monte Carlo simulations produces results closer to the actual air flow distribution. For fluctuating  $C_p$  values, the sample-average air flows deviate by less than 10% from the mean air flow calculated using the measured data, while the corresponding sample mean using mean  $C_p$  value deviates by 17–23% from the measured mean (Table 1). Overall, the use of fluctuating  $C_p$  values in combination with wind speed probability distribution function gives a root mean square error (RMSE) of 1.51 L/s, while the use of mean  $C_p$  value in combination with wind speed pdf gives an almost double corresponding RMSE of 3.12 L/s.

**Table 1.** Mean air flow using measured data and sample average air flow calculated through the Monte Carlo simulations.

Method	Top East	Top Center	Top West	Middle Center	Middle West	Low Center	RMSE
Measured	18.59 L/s	19.27 L/s	17.68 L/s	13.52 L/s	13.32 L/s	19.29 L/s	-
Fluctuating $C_p$	20.22 L/s	20.85 L/s	19.18 L/s	14.92 L/s	14.73 L/s	20.80 L/s	1.51 L/s
Mean $C_p$	22.12 L/s	22.83 L/s	20.75 L/s	16.61 L/s	15.62 L/s	22.29 L/s	3.12 L/s
Mean $C_p + U_{hourly}$	20.37 L/s	22.44 L/s	20.37 L/s	16.10 L/s	15.40 L/s	21.94 L/s	2.53 L/s

Furthermore, for every measuring position, the air flow through the ideal gap was calculated using the mean  $C_p$  value in combination with hourly-averaged wind speeds. The results show that this conventional way of calculating air flows deviates approximately 10–20% from the actual air flows and produces a RMSE of 2.53 L/s. It is worth noting that, although the conventional method is the most simplified method used to calculate air flows, it produces better results with lower RMSE compared to the use of mean  $C_p$  in combination with wind speed pdf.

Both the calculated air flow probability distributions and the calculated air flow distribution highlight the significance of area-specific wind pressure coefficients instead of surface-averaged wind pressure coefficients for the air infiltration calculations [9,11]. The air flow differs substantially between measuring positions accordingly to the measured wind pressure coefficients. For example, the mean calculated air flow using measured data for the top center measuring position is calculated at 20.85 L/s, while the corresponding mean air flow for the middle center position is calculated at 14.92 L/s, signifying a difference of approximately 28%. The spatial difference on air flow due to the spatial variations of wind pressure coefficients can be seen through the statistical method, regardless of the input—probability distribution function or mean  $C_p$  value. Although the sample-average air flow values using the probability distribution function and the mean  $C_p$  value on Monte Carlo simulations are higher than the measured mean air flows, they still manage to capture the same deviation of 28% between the calculated air flow at the top center and at the middle center position. Similarly, the spatial variation is also captured by the conventional calculation method. As a result, the determination of wind pressure coefficients with spatial resolution along the façades of medium- and large-scale buildings can significantly improve the calculation process of air changes.

#### 4. Discussion

Full-scale measurements for the determination of wind pressure coefficients have been performed in a twin medium-rise building complex. Conventionally, full-scale measurements have been performed in low-rise buildings with simple geometries for the determination of characteristic wind loads and the validation of wind-tunnel tests. In this study, the on-site pressure measurements performed highlight the spatial variation of the wind pressure coefficients along the windward façade of a building complex. The case of the building complex examined indicates that the surroundings can have a significant impact on the wind-induced pressure variations along the building façades and can lead to very building-specific spatial wind-induced pressure variations and consequently to building-specific wind pressure coefficients. Although full-scale measurements are difficult to perform for each individual case, CFD simulations can be employed in order to determine building-specific wind pressure coefficients with respect to the microclimate. In addition, in cases of twin-building complexes, the microclimate formed by the two buildings has a clear effect on the wind-induced pressure coefficients. The full-scale measurements show that for specific wind directions, one building can provide substantial wind shelter to its twin. This fact, in combination with local weather patterns (for example, in a town with a specific annual dominant wind direction), can lead to considerably reduced wind loads acting on one of the buildings throughout the whole year.

Furthermore, studies describe the uncertainties introduced in the air flow rate calculations due to the use of surface-averaged wind pressure coefficients. The on-site measurements performed within the context of this study strengthen the aforementioned argument and show that the wind pressure



coefficients of the windward façade of a medium-scale building can vary in a significantly spatial way along the façade. Furthermore, the air flow calculations performed show that positions with significant differences in the measured wind pressure coefficients present equally significant differences of their corresponding calculated air flow rates. Therefore, the determination of local wind pressure coefficients with high resolution along the building façades seems to be a suitable method that can increase the air flow rate calculation accuracy.

Studies have also described how the wind gustiness effect has a great impact on air infiltration. In addition, studies have also described the probabilistic nature of wind pressure coefficients. The Monte Carlo method seems a promising solution that can combine the probability distribution functions, which describe the fluctuating nature of wind pressure coefficients, and the probability distribution function of wind velocity, which can account for the occurring wind gusts. The use of mean  $C_p$  values in combination with the pdf of wind speed, as well as the conventional method of calculating air flow rates (mean  $C_p$  value in combination with hourly-averaged wind speeds), have also been evaluated. The results show that use of probability distribution functions for both  $C_p$  values and wind speeds by means of the Monte Carlo method produce the most accurate results regarding the calculated air flow rates.

## 5. Conclusions

The full-scale measurements performed for the purpose of this study showed that wind pressure coefficients vary significantly along the façade of medium-rise buildings, with the measured  $C_p$  values varying by even 50% between two height zones. Furthermore, the measurements showed that, in cases of twin-building complexes, under certain wind conditions, one building can provide substantial shelter to its twin. Overall, the results give an indication for the importance of the surroundings on the determination of wind-induced pressurization of buildings.

Furthermore, the results showed that positions with significant differences in their local measured wind pressure coefficients present similar differences in the corresponding calculated air flow rates, thus highlighting the importance of including local  $C_p$  values and not surface-averaged for the calculation of air infiltration. Based on the measured data, the variation of wind pressure coefficients along the building façade can lead to up to 28% difference of air flow rates among the various positions on the building façade.

Last but not least, the use of probability distribution functions of  $C_p$  values, instead of mean (time-averaged)  $C_p$  values, in combination with the probability distribution function of wind speeds, can increase the accuracy of the air flow rate calculation. The results indicate that the use of probabilistic  $C_p$  values can increase the accuracy of air flow rate by 40% compared to the conventional method, which employs mean  $C_p$  values in combination with hourly-averaged wind speeds. As a result, the suggested method has the potential to improve the overall prediction of the building energy demands.

**Author Contributions:** Conceptualization, S.C. and T.K.T.; Methodology, S.C, T.K.T. and T.A.; Software, S.C.; Validation, S.C.; Formal Analysis, S.C. and T.K.T.; Investigation, S.C.; Resources, T.K.T.; Data Curation, S.C.; Writing-Original Draft Preparation, S.C.; Writing-Review & Editing, S.C.; Visualization, S.C.; Supervision, T.K.T.

**Funding:** This research received no external funding.

**Acknowledgments:** The authors thank Tom Ringstad for setting up the data acquisition system, Arne Svendsen for constructing parts of the measuring equipment, Ole Semb for providing access to the building facilities on daily basis, and Dag Pasca for providing help with the Monte Carlo method.

**Conflicts of Interest:** The authors declare no conflict of interest.

## References

1. Costola, D.; Blocken, B.; Hensen, J.L.M. Overview of the pressure coefficient data in building energy simulation and air flow network programs. *Build. Environ.* **2009**, *44*, 2027–2036. [[CrossRef](#)]
2. European Standard EN 1991:1-4:2005. *Actions on Structures—Part 1-4: General Actions—Wind Actions*; European Committee for Standardization: Brussels, Belgium, 2005.

3. Architectural Institute of Japan. *Recommendations for Loads on Buildings—Chapter 6: Wind Loads*; Architectural Institute of Japan: Tokyo, Japan, 2005; pp. 1–81.
4. Liddament, M.W. *A Guide to Energy Efficient Ventilation*; Annex V Air Infiltration and Ventilation Centre: Great Britain, UK, 1996; pp. 215–250.
5. Hubova, O.; Macak, M.; Konecna, L.; Ciglan, G. External Pressure Coefficients on the Atypical High-Rise Building—Computing Simulation and Measurements in Wind Tunnel. *Procedia Eng.* **2017**, *190*, 488–495. [[CrossRef](#)]
6. Verma, S.K.; Kumar, K.; Kaur, H. Estimation of Coefficient of Pressure in High Rise Buildings Using Artificial Neural Network. *Int. J. Eng. Res. Appl.* **2014**, *4*, 105–110.
7. Charisi, S.; Waszczuk, M.; Thiis, T.K. Investigation of the pressure coefficient impact on the air infiltration in buildings with respect to microclimate. *Energy Procedia* **2017**, *122*, 637–642. [[CrossRef](#)]
8. Charisi, S.; Waszczuk, M.; Thiis, T.K. Determining building-specific wind pressure coefficients to account for the microclimate in the calculation of air infiltration in buildings. *Adv. Build. Energy Res.* **2019**, under review.
9. Costola, D.; Blocken, B.; Hensen, J.L.M. Uncertainties due to the use of surface averaged wind pressure coefficients. In Proceedings of the 29th AIVC Conference, Kyoto, Japan, 14–16 October 2008.
10. Montazeri, H.; Blocken, B. CFD simulation of wind-induced pressure coefficients on buildings with and without balconies: Validation and sensitivity analysis. *Build. Environ.* **2013**, *60*, 137–149. [[CrossRef](#)]
11. Costola, D.; Blocken, B.; Ohba, M.; Hensen, J.L. Uncertainty in air flow rate calculations due to the use of surface-averaged pressure coefficients. *Energy Build.* **2010**, *42*, 881–888. [[CrossRef](#)]
12. Bowen, J.J. *A Wind Tunnel Investigation Using Simple Building Models to Obtain Mean Surface Wind Pressure Coefficients for Air Infiltration Estimates*; NRC report LTR-LA-2009; National Research Council: Ottawa, ON, Canada, 1976; pp. 74–106.
13. Surry, D. Pressure measurements on the Texas Tech Building: Wind Tunnel Measurements and comparisons with full scale. *J. Wind Eng. Ind. Aerodyn.* **1991**, *38*, 235–247. [[CrossRef](#)]
14. Xu, Y.L.; Reardon, G.F. *Full-Scale and Model-Scale Wind Pressure and Fatigue Loading on Texas Tech University Building*; Technical report No. 42; James Cook University of North Queensland: Douglas, Australia, 1996.
15. Richards, P.J.; Hoxey, R.P.; Short, L.J. 2001. Wind pressures on a 6m cube. *J. Wind Eng. Ind. Aerodyn.* **2001**, *89*, 1553–1564. [[CrossRef](#)]
16. Mendis, P.; Ngo, T.; Haritos, N.; Hira, A. Wind Loading on Tall Buildings. *EJSE Spec. Issue Load. Struct.* **2007**, 41–54.
17. Blocken, B. 50 years of Computational Wind Engineering: Past, Present and future. *J. Wind Eng. Ind. Aerodyn.* **2014**, *129*, 69–102. [[CrossRef](#)]
18. Orme, M.; Liddament, M.W.; Wilson, A. *Numerical Data for Air Infiltration & Natural Ventilation Calculations. Report*; Technical Note AIVC 44; Annex V. Air Infiltration and Ventilation Center: Great Britain, UK, 1998.
19. Haghghat, F.; Brohus, H.; Rao, J. Modelling air infiltration due to wind fluctuations—A review. *Build. Environ.* **2000**, *35*, 377–385. [[CrossRef](#)]
20. Rao, J. Assessment of the Effect of Mean and Fluctuating Wind-Induced Pressures on Air Infiltration and Ventilation in Buildings: A System Theoretic Approach. Ph.D. Thesis, Concordia University, Montréal, QC, Canada, 1993.
21. Etheridge, D.W. Unsteady flow effects due to fluctuating wind pressures in natural ventilation design—Mean flow rates. *Build. Environ.* **2000**, *35*, 111–183. [[CrossRef](#)]
22. Kraniotis, D.; Thiis, T.K.; Aurlien, T. A numerical study on the impact of wind gust frequency on air exchanges in buildings with variable external and internal leakages. *Buildings* **2014**, *4*, 27–42. [[CrossRef](#)]
23. Quan, Y.; Wang, F.; Gu, M. A method for estimation of extreme values of wind pressure on buildings based on the generalized extreme-value theory. *Math. Probl. Eng.* **2014**, *2014*, 926253. [[CrossRef](#)]
24. Sensirion, The Sensor Company. *Datasheet SDP1000: Low Range Differential Pressure Sensor for Air and Non-Aggressive Gases*; Version 5.1; Sensirion: Lake Zurich, Switzerland, 2017; pp. 1–8.
25. Tennekes, H. The logarithmic wind profile. *J. Atmos. Sci.* **1972**, *30*, 234–238. [[CrossRef](#)]
26. Metropolis, N.; Ulam, S. The Monte Carlo Method. *J. Am. Stat. Assoc.* **1949**, *44*, 335–341. [[CrossRef](#)]
27. Thomopoulos, N.T. *Essentials of Monte Carlo Simulation: Statistical Methods for Building Simulation Models*; Springer: New York, NY, USA, 2013.

28. Jacob, D.; Burhenne, S.; Florita, A.R.; Henze, G.P. Optimizing Building Energy Simulation Models in the Face of Uncertainty. In Proceedings of the 4th National Conference of IBPSA-USA, New York, NY, USA, 11–13 August 2010.
29. Oberle, W. *Monte Carlo Simulations: Number of Iterations and Accuracy*; Technical Note ARL-TN-0684; US Army Research Laboratory: Adelphi, MD, USA, 2015.
30. Calif, R.; Schmitt, F.G. Modeling of atmospheric wind speed sequence using a lognormal continuous stochastic equation. *J. Wind Eng. Ind. Aerodyn.* **2012**, *109*, 1–8. [[CrossRef](#)]
31. Garcia, A.; Torres, J.L.; Prieto, E.; de Francisco, A. Fitting wind speed distributions: A case study. *Sol. Energy* **1998**, *62*, 139–144. [[CrossRef](#)]
32. Zaharim, A.; Razali, A.M.; Abidin, R.Z.; Sopian, K. Fitting of Statistical Distributions to Wind Speed Data in Malaysia. *Eur. J. Sci. Res.* **2009**, *26*, 6–12.
33. Safari, B. Modelling wind speed and wind power distributions in Rwanda. *Renew. Sustain. Energy Rev.* **2011**, *15*, 925–935. [[CrossRef](#)]
34. Smith, S.W. *The Scientist and Engineer's Guide to Digital Signal Processing*, 2nd ed.; California Technical Publishing: San Diego, CA, USA, 1997; pp. 277–284.



© 2019 by the authors. Licensee MDPI, Basel, Switzerland. This article is an open access article distributed under the terms and conditions of the Creative Commons Attribution (CC BY) license (<http://creativecommons.org/licenses/by/4.0/>).

ISBN: 978-82-575-1592-8

ISSN: 1894-6402



Norwegian University  
of Life Sciences

Postboks 5003  
NO-1432 Ås, Norway  
+47 67 23 00 00  
[www.nmbu.no](http://www.nmbu.no)